

**MAPPING OF MODERN PYROCLASTIC DEPOSITS WITH
GROUND PENETRATING RADAR:
EXPERIMENTAL, THEORETICAL AND FIELD RESULTS**

by

ALISON C. RUST

B.Sc., The University of Toronto, 1996

A THESIS SUBMITTED IN PARTIAL FULFILLMENT OF
THE REQUIREMENTS FOR THE DEGREE OF
MASTER OF SCIENCE

in

THE FACULTY OF GRADUATE STUDIES
GEOLOGICAL SCIENCE DIVISION
DEPARTMENT OF EARTH AND OCEAN SCIENCES

We accept this thesis as conforming
to the required standard

THE UNIVERSITY OF BRITISH COLUMBIA

August, 1998

© Alison C. Rust, 1998

In presenting this thesis in partial fulfilment of the requirements for an advanced degree at the University of British Columbia, I agree that the Library shall make it freely available for reference and study. I further agree that permission for extensive copying of this thesis for scholarly purposes may be granted by the head of my department or by his or her representatives. It is understood that copying or publication of this thesis for financial gain shall not be allowed without my written permission.

Department of Earth and Ocean Sciences

The University of British Columbia
Vancouver, Canada

Date August 24, 1998

Abstract

This thesis explores the utility of ground-penetrating radar (GPR) in mapping and characterizing young pyroclastic deposits. In particular, laboratory measurements examine the relationship between porosity and dielectric constant of volcanic rocks. Simulations and field studies demonstrate how GPR data can be used to both image, and quantify, relative porosity variations in pyroclastic deposits. The laboratory results (Chapter 2) indicate a strong and definite relationship between total porosity and dielectric constant of dry, felsic to intermediate volcanic rocks. The trend formed by these data is remarkably tight and coherent, especially considering the samples derive from five deposits and two volcanoes. Chapter 3 models the propagation of a radar wave through a welded pyroclastic flow deposit of variable porosity using the porosity-dielectric constant relationship from Chapter 2. Although porosity changes are gradational, the deposit generates reflections. Distinctive signals correspond to portions with essentially constant porosity or areas where porosity changes with depth at a moderate rate.

GPR data were collected on sections of pyroclastic fall and welded and unwelded pyroclastic flow deposits in Central Oregon (Chapter 4). Airfall and pyroclastic flow deposits can be distinguished on the basis of their distinct geophysical character. For example, the same characteristic signals for regions of changing porosity with depth and regions of constant porosity, which were recognized in the modeling (Chapter 3), are seen in the GPR data. The results indicate that GPR can be used to map the intensity of welding and separate zones of uniform welding from zones of variable welding. Velocity analysis of common midpoint (CMP) surveys is shown to aid in mapping facies variations, as well as,

converting travel times into depths in radargrams. GPR is also found to be useful in delimiting deposit thicknesses and geometries away from exposure.

Table of Contents

Abstract	ii
List of Tables	vi
List of Figures	vii
Preface	x
Acknowledgments	xi
1. Introduction	1
2. Dielectric constant as a predictor of porosity in dry volcanic rocks	4
2.1 Introduction	4
2.2 Previous studies	5
2.3 Selection of sample suites	13
2.4 Measurement of porosity and density	14
2.5 Measurement of K'	21
2.6 Relationship between Φ and K'	27
2.7 Relationship between ρ_T and K'	34
2.8 Applications and limitations of results for GPR	36
3. Detection and mapping of welding in pyroclastic flows with GPR: Forward modeling results	39
3.1 Introduction	39
3.2 Subsurface model profiles	40
3.3 Critical layer thickness (L_c)	44
3.4 Forward Modeling Results	47
3.5 Applicability to field GPR studies	53
3.6 Conclusion	58
4. Methods for mapping and characterizing pyroclastic flow and fall deposits with GPR	60
4.1 Introduction	60
4.2 Field sites	61
4.3 Calibration of characteristic signals in radargrams	63
4.4 Velocity analysis	75
4.5 Columbia Southern Canal: mapping deposit geometries	87
4.6 Summary and conclusions	98

5. Conclusion	100
References	103
Appendix I Measurement of density and porosity in volcanic rocks.	114
Appendix II Scale of heterogeneity of pyroclastic deposits and applicability of gradational porosity profile models	122
Appendix III Inversion for porosity in the presence of water	126

List of tables

Table 2.1	Details of 24 previous studies which reported dielectric constant measurements on igneous samples	6
Table 2.2	Experimentally measured values of density, porosity and dielectric constant for samples of volcanic rock.....	17
Table 2.3	Parameters to model lines describing dielectric constant-porosity data.....	32
Table 4.1	Collection parameters and processing for radargrams.....	64

List of Figures

Figure 2.1	Plot of K' vs. ρ_T for data from Shmulevich et al. (1971) and model curves derived from Ulaby et al. (1990) and Olhoeft and Strangway (1975), respectively.....	8
Figure 2.2	Published values of K' and Φ for volcanic rocks.....	11
Figure 2.3	Comparison of values of measured porosity, determined as connected porosity calculated from Eq. (2.5), and total porosity calculated from Eq. (2.6).....	18
Figure 2.4	Values of Φ_{Comm} (a) and Φ_T (b) are plotted against ρ_T	20
Figure 2.5	Measured values of K' plotted as a function of frequency.....	25
Figure 2.6	Plots of K' versus Φ	26
Figure 2.7	Comparison of new data (porosity values represent total porosity) and results from other sources.....	28
Figure 2.8	Plots of K' versus ρ_T	29
Figure 3.1	Bulk density (ρ_T) versus depth profiles for a basaltic ignimbrite at Playa de Tasarte, Gran Canaria (after Freunt and Schmincke, 1995).....	41
Figure 3.2	Schematic demonstration of steps in conversion from continuous porosity (Φ) profile to discretized profile of dielectric constant (K').....	43
Figure 3.3	Discretized profile of K' using 1 cm thick layers.....	45
Figure 3.4	Simulations for profile a (Fig. 3.1-3.3) at a variety of frequencies (f) and layer thicknesses (L).....	46
Figure 3.5	Synthetic traces resulting from modeling a 25 MHz electromagnetic wave propagating through the two (a and b) Playa de Tasarte sections.....	49
Figure 3.6	Synthetic traces (0-150 ns) resulting from modeling 25, 35, 50, 100 and 200 MHz waves passing through the two Playa de Tasarte sections.....	50
Figure 3.7	Results (150 to 300 ns) of simulations for K' profiles of Figure 3.3 at a variety of frequencies.....	51

Figure 3.8	Raw GPR data with minimal processing.....	54
Figure 3.9	Comparison of model and field GPR traces: a) synthetic trace for Playa de Tasarte, profile b (welded to base); b) average of 31 GPR traces from positions 10 to 40 m of Figure 3.8a.....	56
Figure 4.1	Location of two field sites near Bend, Oregon. A) Cascade Pumice Company pits. B) Site along the Columbia Southern Canal.....	62
Figure 4.2	Locations of surveys at the Cascade Pumice Company pits. Black arrows mark midpoints of common midpoint (CMP) surveys.....	65
Figure 4.3	Radargrams from the Cascade Pumice pits.....	66
Figure 4.4	Photographs of GPR lines at Cascade Pumice Company pits.....	68
Figure 4.5	Migrated version of 50 MHz, line 1 radargram (Fig. 5.4a).....	72
Figure 4.6	50 MHz common midpoint survey CMP1 (Fig. 4.2).....	76
Figure 4.7	Results of five CMP surveys plotted as root mean squared velocity vs. time.....	77
Figure 4.8	Plots showing velocity analysis results for five CMP surveys.....	79
Figure 4.9	Plot of velocity versus height above Tumalo Tuff/Bend Pumice boundary.....	80
Figure 4.10	Plot of velocity in lowermost interval velocity for Tumalo Tuff (V_{TT}) vs. Bend Pumice velocity (V_{BP}).....	83
Figure 4.11	The first 10 m of surveys 1 and 4 are displayed with common two-way travel time (center column). The depths scales for each survey derive from CMP analyses (Fig. 4.8, 4.9).....	85
Figure 4.12	Comparison of depth to Tumalo Tuff/Bend Pumice boundary calculated from CMP velocity analysis (Fig. 4.9) and depth measured with a tape measure.....	86
Figure 4.13	View of Columbia Southern Canal site, looking upstream.....	88
Figure 4.14	Location of GPR surveys at the Columbia Southern Canal site.....	89
Figure 4.15	50 MHz surveys at the Columbia Southern Canal without topographic correction.....	90

- Figure 4.16** 100 MHz radargrams at Columbia Southern Canal trending approximately north-west91
- Figure 4.17** 100 MHz radargrams at Columbia Southern Canal trending approximately north-east.....92
- Figure 4.18** Four views of 100 MHz radargrams fenced together.....93
- Figure 4.19** Photographs from Colombia Southern Canal site. a) Exposure on south-east side of canal across from survey point C (Fig. 4.14). All deposits show little or no welding on this exposure. b) Layer of cobbles in strongly welded Shevlin Park flow marking the boundary of the phases of the flow.....95
- Figure 4.20** a) Migrated radargram for survey F-P (100 MHz) using a constant velocity of 0.1 m/ns. b) Interpreted stratigraphy for a).....97
- Figure A2.1** Three processed versions of the radargram of Figure 3.8. a) Migrated data assuming constant velocity of 0.09 m/ns. Note the removal of hyperbolic events seen in Fig. 3.8. b) Each trace is the mean of ten adjacent traces in Fig.3.8. c) Each trace is the average of ten adjacent traces of the migrated radargram (a).....124
- Figure A3.1** Dielectric constant vs. depth data for two CMP surveys at Cascade Pumice Company pits (Chapter 4). Shaded region indicates range of values predicted for dry, intermediate to felsic volcanic rocks according to laboratory experiments.....128

Preface

This thesis comprises slightly modified versions of three papers (Chapters 2, 3 and 4) which are submitted to refereed journals or are in preparation for publication. Chapter 2 was submitted to the Journal of Volcanology and Geothermal Research. Chapter 3 and 4 are in preparation for submission to the Journal of Volcanology and Geothermal Research, and Bulletin of Volcanology, respectively. My supervisor, Dr. J. K. Russell is a co-author on all three papers, while Dr. R. J. Knight is third author for the Chapter 2 paper. All data collection (lab and field), data processing, analysis and interpretation was performed by me. Dr. Russell supervised and financed the project, and provided text revisions. Dr. Knight contributed analytical supervision and text revisions for Chapter 2.

Acknowledgments

Financial support for this research derives from an NSERC PGS A scholarship (A.C. Rust) for September 1996 to September 1998, and NSERC Research Grant #OGP0820 (J. K. Russell). I especially thank Rosemary Knight and members of the Rock Physics lab group, Paulette, Kevin and Christina for their assistance and helpful suggestions. I am grateful to Steve Cardimona for the use of his program which models EM wave propagation (Chapter 3). This chapter also benefitted from comments by Guy Cross. I thank Britt Hill for suggesting interesting field sites, and Larry Chitwood and family for their consummate generosity and the logistical support they provided in Oregon. Finally, I appreciate Kelly's never-ending enthusiasm and thank him for being an insightful igneous petrologist just crazy enough to try geophysics.

Chapter 1

Overview

Ground-penetrating radar (GPR), used in conjunction with conventional field techniques, offers an effective means of mapping the distribution and architecture of Modern volcanic deposits. There are several challenges associated with conventional mapping which GPR allows us to overcome. Firstly, the youthful, undissected landscapes associated with many Modern volcanic edifices offer little exposure of the 3rd dimension (depth). Secondly, volcanic stratigraphy is notoriously complex in terms of facies variations. Thirdly, the distribution of volcanic deposits can be heavily influenced by paleo-topography, making the stratigraphic correlation of specific units complicated. The fact that many young volcanic deposits are relatively thin and electrically resistive makes it very likely that GPR can probe the entire thickness of these deposits. On this basis GPR promises to be useful in mapping deposit boundaries as well as characterizing the internal structures of volcanic units.

A theme, central to this research, is the use of GPR to obtain information about spatial variations in the porosity of volcanic deposits. Volcanic successions can show large variations in porosity that relate directly to volcanic processes. Porosity variation relates to the type of deposit (e.g., pyroclastic deposits vs. lava flows), to stratigraphic position within an individual unit (e.g., flow top vs. flow interior), and to lateral facies changes (e.g., proximal vs. distal lava flows). GPR has the potential to map porosity in the subsurface; this information can in turn, be used to identify deposit types and facies changes within units.

The thesis comprises three papers (Chapters 2, 3 and 4), as described below, followed

by a summary of principal conclusions (Chapter 5) and three appendices which provide additional discussion on peripheral topics. The chapters progress from laboratory work examining the effect of porosity on radar velocity in volcanic rocks (Chapter 2), to forward modeling of radar propagating through a welded pyroclastic flow (Chapter 3), and finally to GPR field work on pyroclastic deposits (Chapter 4).

Chapter 2 is a laboratory study which examines the relationship between dielectric constant (K') and porosity (Φ) of dry volcanic rocks. Dielectric constant is the primary physical property controlling the velocity of radar through low loss material and K' values can be extracted from GPR data by acquiring estimates of radar velocities from common midpoint surveys. However, an understanding of the dielectric properties of volcanic rocks is required to convert K' values into material properties (i.e., porosity). Previous investigations of the dielectric constants of volcanic rocks have primarily focused on the influence of frequency, temperature and bulk density on K' . Chapter 2 reviews results from the literature, presents new data, and then explores the relationship between K' , porosity and bulk density for a suite of 34 samples of diverse volcanic origin, composition, and vesicularity. An empirical model is presented that relates rock porosity to dielectric constant of non-basaltic volcanic rocks. Chapter 2 shows that there is a strong correlation between the degree of vesicularity of volcanic rocks and their dielectric properties.

Chapter 3 investigates the potential and the limitations of using GPR to delineate and trace welded portions of pyroclastic flows using a program by Steven Cardimona which models electromagnetic wave propagation through layered media. Input K' profiles are calculated from porosity profiles of a pyroclastic flow using the empirical K' -porosity

relationship developed in Chapter 2. Two approaches to detecting and mapping welding are considered: i) identification of characteristic signals or textures in radargrams for distinct welding facies; ii) tracing of strong, continuous reflections produced by rapid porosity changes bordering welded zones. Furthermore, I test ideas derived from this modeling against a case study comprising GPR data collected at a well exposed, welded pyroclastic flow. Appendix II discusses the effect of the scale of heterogeneity of pyroclastic deposits on the interpretation of radargrams using the modeling results of Chapter 3.

Chapter 4 uses GPR field data collected on pyroclastic rocks near Bend, Oregon to demonstrate methods of characterizing and mapping pyroclastic deposits with GPR. The surveys show that valuable volcanological information is attainable from GPR studies. Surveys from a pumice quarry allow the comparison of radar signals to exposed stratigraphy; on this basis characteristic radar signals for individual units and facies are identified. Data from common midpoint (CMP) surveys are analyzed to determine relative porosity patterns in a welded pyroclastic flow. A second field site, 3 km to the south-west, tests the utility of GPR in mapping deposit geometries away from exposed stratigraphy. The use of GPR in volcanology is in its infancy and an important contribution of this chapter is the demonstration of the quality of data that can be obtained and the type of information of interest to volcanologists that can be deduced with GPR surveys.

Chapter 2

Porosity as a predictor of dielectric constant of dry volcanic rocks

2.1 Introduction

Ground penetrating radar (GPR) is a high resolution, near-surface, geophysical technique that provides a means of imaging geological structures and materials in the subsurface. Young volcanic deposits are ideal candidates for GPR surveys because they are electrically resistive, and commonly form thin surficial deposits within 50m of the earth's surface. Of specific interest in my research is the use of GPR to obtain information about the spatial variability in the porosity of young volcanic deposits. Such a technique would be a powerful tool in volcanological studies because volcanic rocks are commonly vesicular and can show large variations in porosity that relate to volcanic processes.

Properties of subsurface materials can be extracted from GPR data by obtaining estimates of radar velocities. This is done using common midpoint surveys, which employ an acquisition geometry that makes it possible to determine the velocity with which an electromagnetic wave travels through a region of the subsurface. The dielectric constant (K') of the material in the region can be calculated from the velocity. However, the conversion of K' into material properties, such as porosity, requires an understanding of the relationship between the property and the dielectric constant. Knowledge of the factors contributing to K' of volcanic deposits also impacts our ability to predict what aspects of volcanic deposits can best be imaged with GPR.

The relationship between the measured dielectric properties and the porosity of

volcanic rocks is affected by numerous factors such as mineralogy, water content, and phase geometries, thus making the accurate interpretation of porosity from GPR data a challenging research problem. In this study I begin to address this issue by investigating the dependence of K' on porosity for dry volcanic rocks. Measurements of K' are presented for several compositions of volcanic rocks over a range of porosities, and a model is presented that relates porosity to dielectric constant. While further research is required to incorporate the effect of other factors on dielectric properties, this model is a first step towards assessing the way in which GPR data can be used to both image, and quantify, porosity variation in young volcanic deposits.

2.2 Previous Studies

Table 2.1 summarizes the results of 24 papers reporting dielectric constant measurements of igneous rocks and includes information on samples, methodology and additional physical properties. The dielectric properties of igneous rocks, and volcanic rocks in particular, have been shown to be sensitive to frequency and temperature (e.g., Saint-Amant and Strangway, 1970; Chung et al., 1970), water saturation (Roberts and Lin, 1997), mineralogy (e.g., Hansen et al., 1973), fabric (Tuck and Stacey, 1977; Hawton and Borradaile, 1988), and bulk density (e.g., Olhoeft and Strangway, 1975). Bulk density is strongly affected by porosity changes but, to date, there has been no comprehensive study directly examining the porosity-dielectric constant relationship in volcanic rocks.

Table 2.1 Details of 24 previous studies which reported dielectric constant measurements on igneous samples

Source	Igneous samples	K ¹ measurement	additional physical properties listed**					
Description	Consolidation	Frequency	Geometry & size*					
			Coating (top and bottom)					
			Moisture Condition					
Adams et al., 1996	volcanic ash (basalt to rhyolite) basalt & granite	unconsolidated solid & powdered	4-19 GHz	n.a.	-	dry; ambient [†]	Φ	X, tan δ
Bondarenko, 1971	plutonic rocks	solid	5 KHz	disks: d=10-12 mm, h=2-3 mm	platinum foil	dry; ambient [†]	ρ	P, T
Campbell and Ulrichs, 1969	volcanic & plutonic rocks	solid & powdered	0.45 & 35 GHz	rectangular parallel-epipeds: 0.71 x 0.36 x 0.25 cm	-	ambient [†]	ρ	X, T, I, tan δ , Φ
Chung et al., 1970	lunar rocks, simulated lunar rock, terrestrial basalts & gabbro	solid	100 Hz - 10 MHz	rectangular parallel-epipeds	0.025 mm thick tin foil	dry; ambient [†]	ρ & Φ (1)	X, T, tan δ , σ
Drury, 1978	basalt	solid	1 Hz - 1 MHz	disks: d=2.54 cm, h=0.5-1.0 cm	-	seawater-saturated	Φ	tan δ , σ
Frisalito et al., 1975	lunar soils & terrestrial basalt	unconsolidated & solid (1)	0.2-100 KHz	n.a.	-	dry; measured in vacuum	ρ	(X), P, tan δ
Gold et al., 1970	lunar rocks & soils	solid & unconsolidated	450 MHz	n.a.	-	ambient [†]	ρ, Φ	(X), tan δ , R, P
Gold et al., 1971 & Gold et al., 1973	lunar rocks & soils	solid & unconsolidated	450 MHz	n.a.	-	dried in vacuum oven	ρ	(X), I, R, P, tan δ ('73)
Hansen et al., 1973	basalt, simulated basalt (Lucite and Ilmenite powders)	solid & powdered	100 Hz - 50 MHz	n.a.	-	dry nitrogen atmosphere; ambient for powders		X, tan δ
Hawton and Berradale, 1989	metavolcanic tuff	solid	5 Hz - 13 MHz	disks: d=12.2 mm, h=2 mm	-	20% relative humidity		tan δ , strain anisotropy
Howell and Licastro, 1961	obsidian & plutonic rocks	solid	50 Hz - 30 MHz	disks: d=2.5-1, h=0.1-0.4 cm	Ag paint or tin-lead foil & petroleum	dry & moist samples; measured in vacuum or air		X, tan δ
Olhoef et al., 1974	lunar rocks & soils (amorphous to basalt)	solid & unconsolidated	variable	variable	-	ambient [†]	ρ	T, (X), σ
Olhoef et al., 1974	lunar soil	unconsolidated	100 Hz - 1 MHz	-	-	dry; measured in vacuum		T, (X), σ
Roberts and Lin, 1997	rhyolitic volcanic tuff	solid	0.1-100 KHz	disks: d=5.1 cm, h=2.3, 4.5 mm	Au sputter (~100 nm) and Au foil (~50 μ m)	variable water saturation; distilled and groundwater	ρ, Φ ++	T, tan δ , σ
Russell and Stasiuk, 1997	volcanic rocks (basalt to dacite)	solid	10 Hz - 10 MHz	disks: d=5, h=0.5 cm	Au sputter (50 nm)	ambient	Φ	(X)
Saint-Amant and Strangway, 1970	dunite & basalt	solid & powdered	50 Hz - 2 MHz	disks: h=2 mm	-	dry; measured in vacuum		T, tan δ
Shmulovich et al., 1971	volcanic and plutonic rocks	solid	500 MHz	n.a.	-	ambient [†]	ρ	X, tan δ , σ
Shmulovich, 1970	volcanic and plutonic rocks	powdered	0.545-37.5 GHz	-	-	ambient [†]		T, tan δ
Singh and Singh, 1991	volcanic and plutonic rocks	solid	0.1-20 MHz	slabs: l=0.4-1.1 cm	-	dry & wet (up to 6.4% moisture)		T, (X), σ , I, tan δ
Strangway et al., 1972	lunar soils & granite	solid & unconsolidated	0.1-100 KHz	n.a.	-	dry; measured in air and vacuum		T, (X), σ , I, tan δ
Troitsky and Shmulovich, 1973	volcanic rocks, granite & peridotite	powdered	9.4 GHz	-	-	ambient [†]	ρ	tan δ
Tuck and Stacey, 1978	basalt	solid	2.3 KHz	disks: d=16 mm, h=1.4 mm	-	dry; cell flushed with dried air before measurement		magnetic anisotropy
Ulabiy et al., 1990	volcanic and plutonic rocks	solid	0.5-18 GHz	t > 4mm	-	dry; ambient [†]	ρ	X, tan δ

* d= diameter, h= height, l= thickness
 ** dielectric constant, frequency and moisture content not included in this column, p= bulk density, Φ = porosity, X= composition (major oxides or mineral modes), (X)= compositional data is published elsewhere, P= compressive pressure, T= temperature, tan δ = loss tangent or dielectric loss, σ = resistivity or conductivity, l = absorption length, R= reflectivity, P= polarization assumed but not stated
 ++ solid density, average pore diameter, surface area also determined

Density & K'

Measurements of density and K' have been made on rocks and their corresponding powders (Campbell and Ulrichs, 1969; Troitsky and Shmulevich, 1973; Frisnillo et al., 1975), on suites of solid and/or naturally unconsolidated volcanic rocks (Chung et al., 1970; Gold et al., 1971 and 1973), on solid rocks (Bondarenko, 1971; Shmulevich et al., 1971) and on unconsolidated material (Gold et al., 1970; Adams et al., 1996).

The most comprehensive study in terms of the range of density and the range of chemical compositions of volcanic rock samples is by Shmulevich et al. (1971). They measured the dielectric properties of 89 acid to ultrabasic igneous rocks (68 volcanic, 21 intrusive) at a frequency of 500 MHz. The bulk density (ρ_T) of volcanic samples ranged from 0.54 to 2.90 g/cm³. Rather than compare ρ_T and K' directly, Shmulevich et al. (1971) plotted K' and the Krotikov parameter (**a**), against SiO₂ content. The Krotikov parameter is defined as:

$$a = \sqrt{K'} - 1/\rho_T \quad (2.1)$$

Troitsky and Shmulevich (1973) found the Krotikov parameter to be practically invariant for lower density igneous rocks ($\rho_T \leq 2$ g/cm³), and for all acidic rocks, regardless of density. This study and others (e.g., Campbell and Ulrichs, 1969; Adams et al., 1996) indicate a trend of increasing K' with decreasing SiO₂ content of volcanic rocks.

Using the values of **a** and ρ_T reported by Shmulevich et al. (1971), I have recalculated values of K' . Figure 2.1 is a plot comparing the values of K' and ρ_T (Shmulevich et al., 1971) against model curves of Ulaby et al. (1990) and Olhoeft and Strangway (1975). Ulaby et al. (1990) fit experimental data from 80 rocks of diverse origin (volcanic, plutonic,

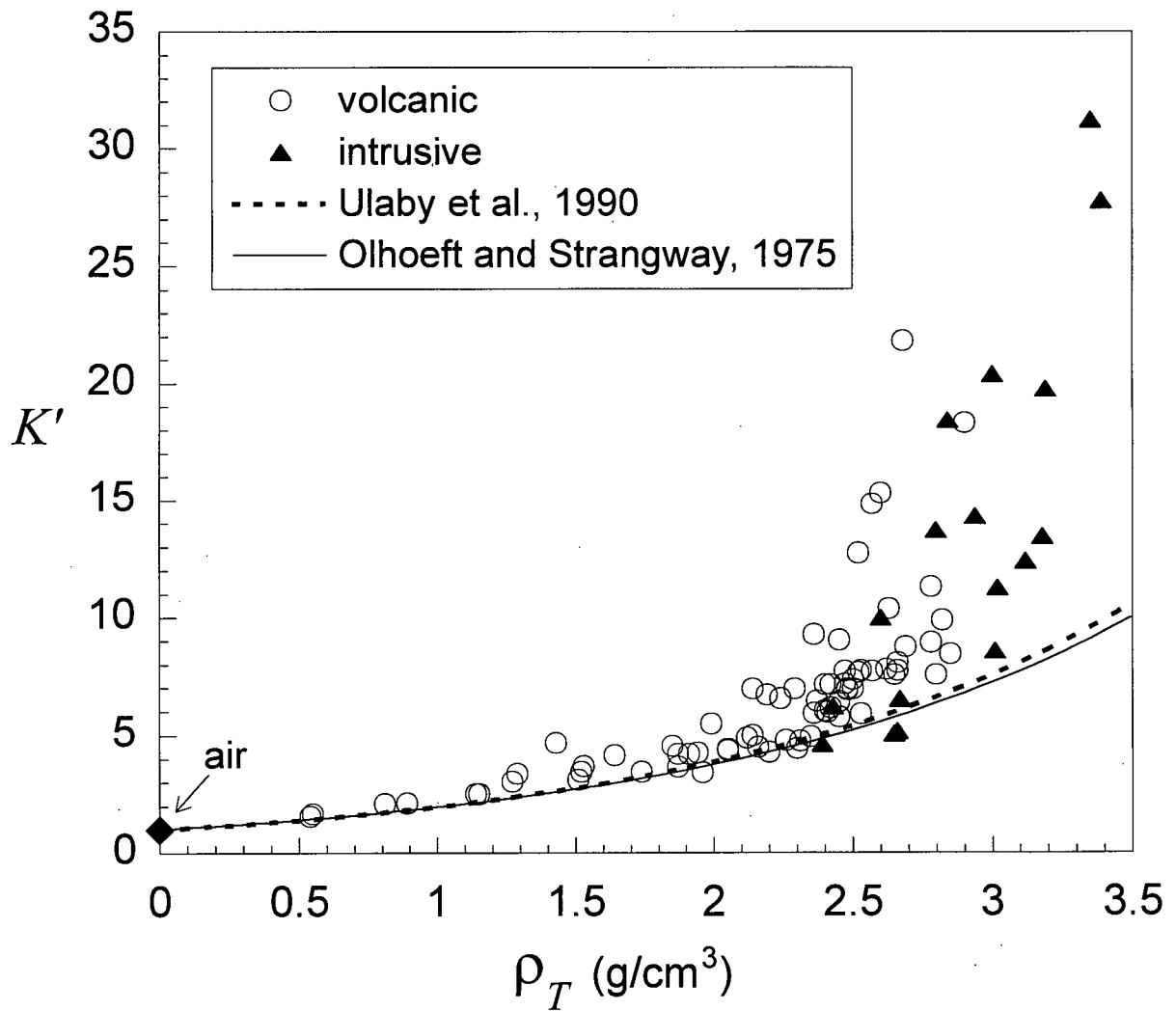


Figure 2.1 Plot of K' vs. ρ_T for data from Shmulevich et al. (1971). The model curves $K' = 1.96^{\rho_T}$ and $K' = 1.93^{\rho_T}$ derived from Ulaby et al. (1990) and Olhoeft and Strangway (1975), respectively.

clastic, carbonate and "other") to:

$$K' = (1.96 \pm 0.14)^{\rho_r} \quad (2.2)$$

Their dielectric data were collected at frequencies from 0.5 to 18 GHz. K' was found to be independent of frequency and they attributed 50% of the variance in the data to variations in sample density. Olhoeft and Strangway (1975) compiled and fit density measurements (92 solid and unconsolidated lunar rocks) to values of K' measured at frequencies greater than 0.1 MHz. Their model curve (Eq. 2.3) is very similar to that of Ulaby et al. (1990):

$$K' = (1.93 \pm 0.17)^{\rho_r} \quad (2.3)$$

The K' predicted by the models of Ulaby et al. (1990) and Olhoeft and Strangway (1975) are consistently lower than the majority of Shmulevich et al. (1971) data. Although intended to predict dielectric constants as a function of ρ_r over the complete range of densities, the model curves fit the lower density data best up to values of 2.0 g/cm³. The variance in measured values of K' increases markedly at higher values of bulk density (e.g., > 2 g/cm) which suggests that some factor other than density also affects dielectric constant of igneous rocks (Fig. 2.1). Nevertheless, density appears to be a good predictor of dielectric constant for volcanic rocks of low to moderate density.

Porosity & K'

There are few published data relating dielectric constant directly to porosity (Φ) for volcanic rocks. Five studies by Campbell and Ulrichs (1969), Chung et al. (1970), Gold et al. (1970), Adams et al. (1996) and Russell and Stasiuk (1997) provide a total of 28 (Φ , K')

points (Fig. 2.2). Data from Roberts and Lin (1997) and Drury (1978) are omitted because the samples were saturated with fresh or sea water (Table 2.1). Measurements of K' were made at a variety of frequencies, and compositions of samples, states of consolidation and methods of measuring porosity all varied.

Campbell and Ulrichs (1969) and Gold et al. (1970) used powdered samples and porosity was calculated assuming that the rock from which the powder originated was not porous (i.e., $\rho_{T(\text{rock})} = \rho_{S(\text{rock})} = \rho_{S(\text{powder})}$):

$$\Phi_{T(\text{powder})} = 1 - \frac{\rho_{T(\text{powder})}}{\rho_{T(\text{rock})}} \quad (2.4)$$

Thus, the reported values of porosity represent minima; the extent to which they are low depends on the actual porosity of the original rocks. The four data points from Gold et al. (1970) derive from a single powdered lunar rock compacted to various porosities. The eleven data points from Campbell and Ulrichs (1969) represent crushed rocks of different composition: obsidians (2), trachyte, phonolite, and basalt (7). All powders were compacted to a porosity of 40%. One objective of this study (Campbell and Ulrichs, 1969) was to compare the electrical properties of powdered material to those of the corresponding rock. They found that the difference in K' between rock types was much smaller where measured on powdered rocks (all at 40% porosity) relative to measurements on the solid rock equivalents.

The relevant samples of Adams et al., (1996) consist of six natural volcanic ashes of variable composition (basalt (2), andesite, dacite (2), and rhyolite) and two powdered basalt samples. K' measurements were made from 4 to 19 GHz. Porosity and density values

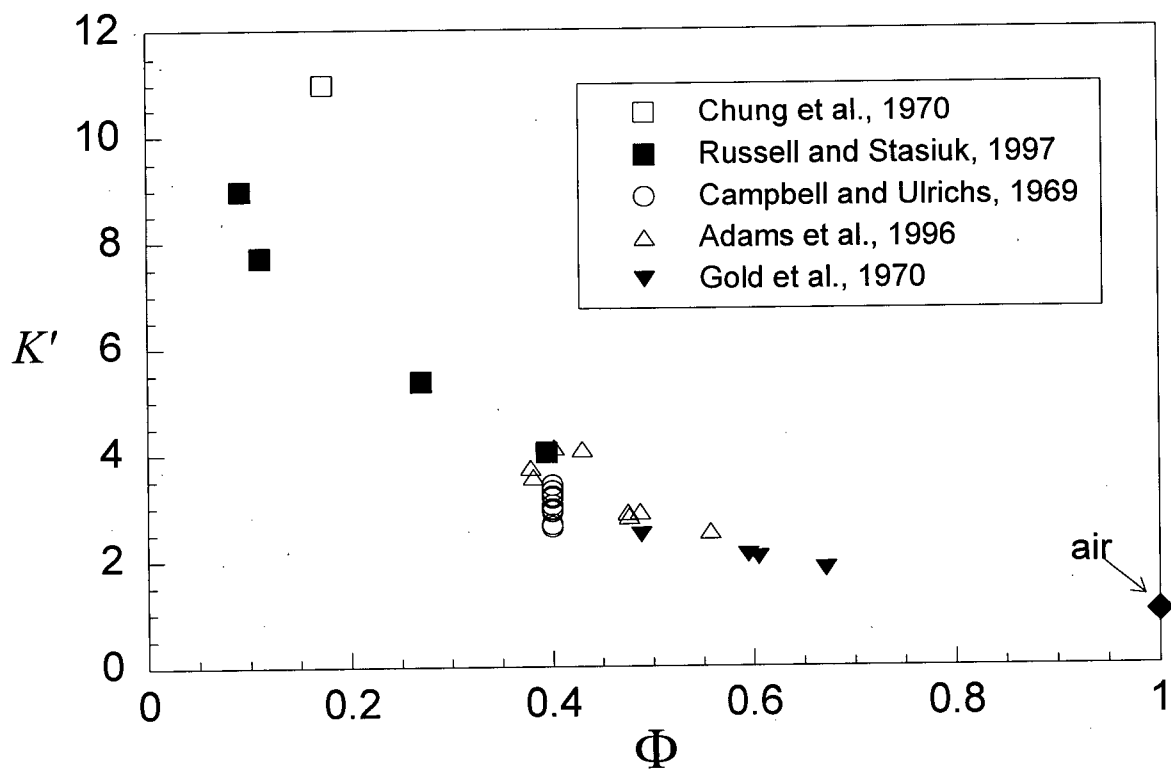


Figure 2.2 Published values of K' and Φ for volcanic rocks. Legend includes sources.

themselves are not reported but rather the fractional volumes are listed. Fractional volume is defined as $\rho_{T(\text{powder})}/\rho_S$; however, Adams et al., (1996) do not state how the solid densities were determined. Fractional volume is equivalent to $1-\Phi$ and the relationship between Φ and K' was indirectly explored by testing the validity of various mixing formulas in relating the dielectric constants of porous powders to the dielectric constants of their solid rock equivalents.

Russell and Stasiuk (1997) measured dielectric constants of four volcanic rocks (basalt lava, dacite pumice, dense obsidian breccia, and dacite lava). They argued that sample porosity is primarily responsible for variations in K' , implying that chemical composition, modal mineralogy, proportion of glass, and grain size have only secondary effects. Measurements were made on multiple sub-samples of each of the four hand-samples. Two of the rock types (basalt and pumice) showed significant variance in K' . Although there was not always a clear relationship between porosity (determined with a helium pycnometer) and dielectric constant in sub-sample suites, a direct correlation was found between the relative variance in sample porosity and the variation in dielectric properties between disks taken from the same hand-sample.

The data point from Chung et al. (1970) is from a lunar rock of unusual chemistry (Kanamori et al., 1970) with low silica (37 wt.% SiO_2) and very high titanium content (12 wt.% TiO_2). Porosity was calculated by examining the pore to rock ratio on the surface of the cylindrical sample. They assumed that this two-dimensional porosity was representative of the three-dimensional porosity (void volume over total volume) of the rock.

Effect of ilmenite on K'

Chung et al. (1970) attributed the higher dielectric constants of their lunar samples, relative to terrestrial basalts, to a greater ilmenite (FeTiO_3) content. Similarly, Hansen et al. (1973) found a positive correlation between dielectric constant and ilmenite content of some basalts. These findings are plausible as ilmenite has a dielectric constant of 30 - 80 (Parkhomenko, 1967; Nelson et al., 1989) compared to, for example, plagioclase, pyroxene and olivine which have dielectric constants between 4 and 11 (Keller, 1989; Nelson et al., 1989). However, neither Hansen et al. (1973) nor Chung et al. (1970) took into account relative porosities or densities of the samples. In fact, porosity data were reported for only one of the three samples examined by Chung et al. (1970). Olhoeft and Strangway (1975) compiled about ninety measurements for lunar rocks and soils and found no correspondence between K' and ($\text{TiO}_2 + \text{FeO}$) content when K' was normalized for constant bulk density (Eq. 2.3). This result, however, does not necessarily negate ilmenite as one of the principal controls on dielectric properties of igneous rocks, because density also increases with increasing ilmenite content. A better understanding of the role of ilmenite would be gained by comparing rock compositions and modal mineralogies to values of K' normalized for porosity rather than density. The effects of other semiconducting oxides commonly occurring in volcanic rocks (magnetite and titanomagnetite) should also be considered.

2.3 Selection of Sample Suites

The central aim of this study is to explore the relationship between the porosity (or vesicularity) of volcanic rocks and their dielectric properties. I also elected to sample a

variety of compositions of volcanic rocks in order to test for compositional controls on K' . Compositionally the study suite spans dacite to basalt. Specifically, it comprises: i) dacite (~ 68 wt. % SiO_2) lava and pumice collected from lava flow, airfall and pyroclastic flow deposits, Mount Meager, B.C. (Stasiuk et al., 1996); ii) dacite (~ 60-62 wt. % SiO_2) lavas from the Ring Creek lava flow, Garibaldi Volcanic Complex, (Sivertz, 1976; Brooks and Friele, 1992); iii) basalt (~ 55 wt. % SiO_2) from a Cheakamus Valley lava flow (Green, 1977; Higman, 1990), and iv) pahoehoe basalt (~ 50 wt. % SiO_2) lava from Mauna Ulu volcano (Swanson, 1973).

Hand samples were chosen in the field with the aim of maximizing the variance in vesicularity of samples from each deposit. This sampling scheme produced suites of rocks of similar composition and mineralogy with a spectrum of porosities (and bulk densities). Each hand-sample was cored, producing 5 cm diameter right cylinders. Bulk density (ρ_T) was calculated using measurements of weight, diameter and height. Redundant samples (rocks with equal bulk densities from the same deposit) were excluded from further procedures. From each core, a 0.5 cm thick disk was prepared. In several instances the cores showed large-scale textural heterogeneity, in which case multiple disks were prepared. For example, all five Mauna Ulu disks (each of which has a different porosity) derive from a single core. All disks were cleaned, dried in an oven at 105°C . Samples equilibrated with the room atmosphere for at least two days before physical properties were measured.

2.4 Measurement of porosity and density

In general, earlier studies of dielectric properties of volcanic rocks report values of

bulk density (ρ_T) and not porosity. I have also measured ρ_T , which depends both on porosity and rock composition, in order to integrate my results with a larger data set from the literature. Density measurements are also used to cross-check primary porosity measurements, by identifying samples with low apparent porosity due to unconnected pores.

Methods

Porosity (Φ) was measured in two distinct ways. Firstly, porosity is calculated from measurements of volume:

$$\Phi = \frac{V_T - V_S}{V_T} \quad (2.5)$$

where V_T is the total volume of the disk and V_S is the solid volume, excluding pores. Operationally, V_T is calculated geometrically on the basis of caliper measurements of height and diameter of the sample disks. V_S , on the other hand, is measured with a helium pycnometer, a technique based on the ideal gas law. If there are unconnected pores not accessed by the helium, then V_S is overestimated as it includes the unconnected pore volume. Therefore, this method of measurement yields the "connected porosity" (Φ_{Comm}). The connected porosity is equal to "total porosity" (Φ_T) only if all pores are connected.

The second way of determining Φ addresses the possibility that a fraction of the pores is not penetrated by helium during the pycnometer experiment. Φ_T as opposed to Φ_{Comm} is calculated from:

$$\Phi_T = \frac{\rho_S - \rho_T}{\rho_S} \quad (2.6)$$

where ρ_T is the bulk density of the disk, and ρ_S is the density of the solid phase. The bulk

density is determined by dividing the mass of the disks by their volumes based on calliper measurements. The density of the solid phase, ρ_s is the void-free density of the sample disk. This measurement is made by crushing a portion of the hand-sample to 200 mesh and calculating the solid density from the mass of the powder and the He-pycnometer measured volume of the same sample of powder. Based on replicate measurements, the precision (1s) associated with measurements of ρ_s , ρ_T , Φ_{Conn} and Φ_T are all less than 1%.

Results

Measured values of bulk density, connected and total porosity are listed in Table 2.2. Figure 2.3 is a comparison of the results of the two methods used to measure porosity. For porosities lower than 0.5 there is excellent agreement between Φ_T and Φ_{Conn} values. Sample PF1 represents a single notable exception ($\Phi_{Conn}=0.33$, $\Phi_T=0.40$). For porosities above 0.5, the measured total porosity is significantly greater than the connected porosity for many samples. The deviation ($\Phi_T - \Phi_{Conn}$) can be as large as 0.11. This indicates that there are unconnected pores in several disks and direct measurements using the helium pycnometer on solid samples may result in apparent porosities significantly lower than true porosities. In fact up to 17% of the pore space can be unconnected (e.g., sample PF1).

All samples showing differences in porosity values >0.01 are from the Mount Meager suite of dacites. In thin section, these rocks are glassy and show a bimodal distribution of vesicles comprising large (mostly macroscopic), well-connected pores and small (< 0.25 mm), more poorly connected vesicles within the glassy matrix. In contrast, the Mauna Ulu basalts have porosities greater than 0.52 yet have virtually identical values of Φ_T and Φ_{Conn} .

Table 2.2 Experimentally measured values of bulk density (ρ_T), connected porosity (Φ_{Conn}), total porosity (Φ_T) and dielectric constant (K') for samples of volcanic rocks. Dielectric constants are reported for a frequency of 10 MHz. Small letters indicate multiple disks from the same hand-sample.

location	sample	ρ_T	Φ_{Conn}	Φ_T	K'
Mount Meager	PM1a	1.083	0.528	0.575	3.411
	PM1b	1.086	0.529	0.573	3.429
	PM 2a	0.937	0.543	0.623	3.073
	PM2b	0.807	0.589	0.675	2.795
	PM3	0.534	0.752	0.789	2.478
	PM5	0.710	0.675	0.715	2.689
	PM6	0.514	0.697	0.796	2.505
	PM8	0.688	0.691	0.723	2.703
	PM9	0.732	0.609	0.706	2.722
	PM10	0.603	0.651	0.758	2.498
	PF1	1.505	0.332	0.398	4.362
	MM1	2.377	0.075	0.083	6.074
	MM2	2.241	0.129	0.138	6.080
	MM3	2.142	0.175	0.180	5.341
	MM4	1.257	0.486	0.501	3.847
MM5	1.454	0.408	0.417	4.366	
MB1	2.403	0.038	0.042	18.353	
Ring Creek	RC1	2.320	0.122	0.130	6.372
	RC2	2.492	0.077	0.083	6.678
	RC3	2.419	0.093	0.099	6.493
	RC5	2.080	0.212	0.214	5.738
	RC6	1.788	0.318	0.313	5.161
	RC9	2.376	0.108	0.115	6.606
	RC10	2.207	0.164	0.165	5.984
	RC11	2.236	0.158	0.164	6.022
Mauna Ulu	ULUa	1.370	0.554	0.557	5.183
	ULUb	1.349	0.564	0.564	4.979
	ULUc	1.476	0.522	0.523	5.573
	ULUd	1.274	0.589	0.588	4.866
	ULUe	1.317	0.571	0.574	4.668
Cheakamus	CB5a	2.712	0.094	0.103	8.322
	CB5b	2.732	0.088	0.096	8.203
	CB7a	2.181	0.265	0.272	11.633
	CB7b	2.272	0.233	0.241	13.472

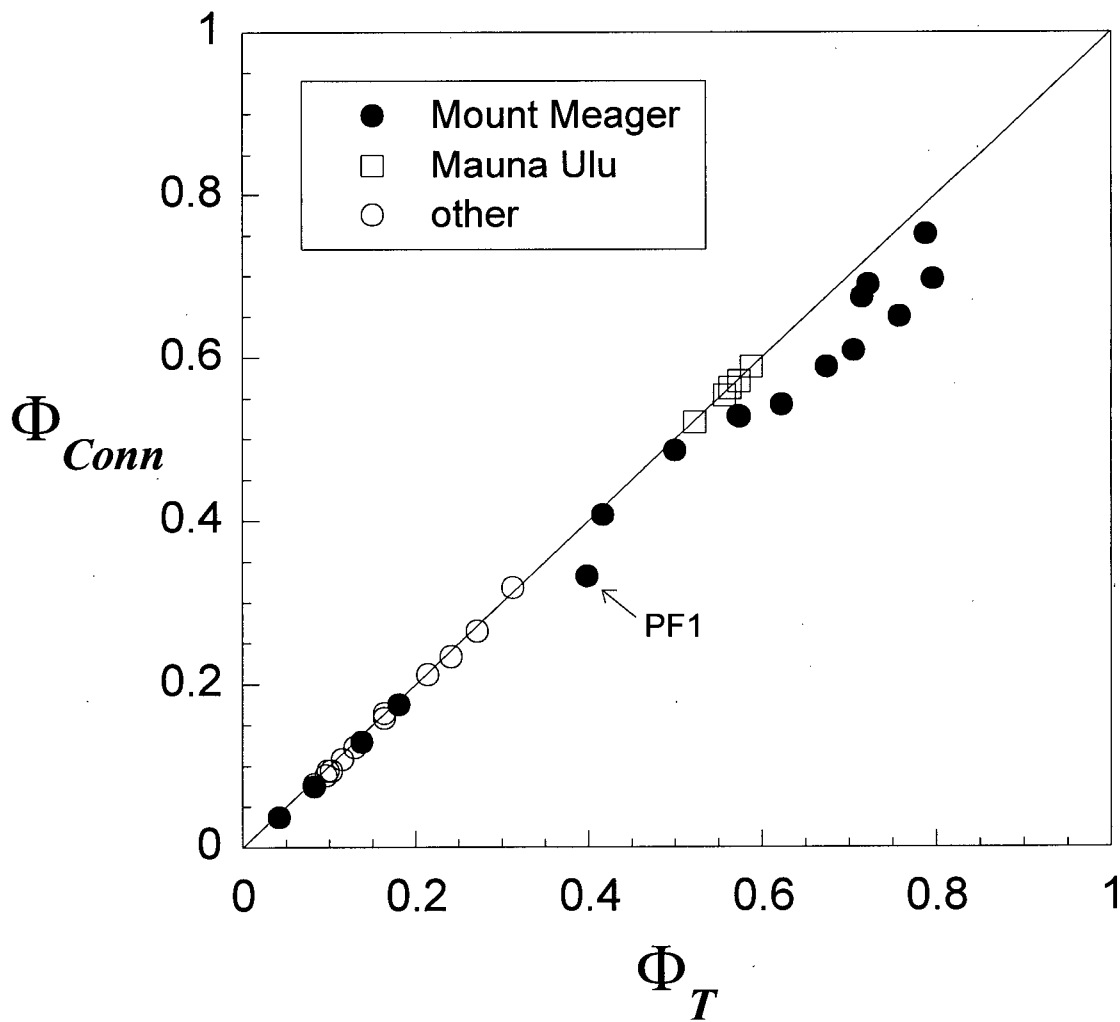


Figure 2.3 Comparison of values of measured porosity, determined as connected porosity calculated from Eq. (2.5), and total porosity calculated from Eq. (2.6). See text for details.

The implication is that all porosity is connected and in thin sections the samples of basalt show pores that are macroscopic and well-connected. Because both connected and unconnected pores should affect values of K' , all subsequent references to sample porosities refer to total porosities as determined by Eq. (2.6).

Figures 2.4a and 2.4b serve to illustrate, in another way, the importance of measuring Φ_T over Φ_{Conn} . For each rock suite of variable vesicularity and constant matrix, there should be a simple linear relationship between porosity and bulk density (Eq. 2.6). Values of Φ plotted against ρ_T should produce a linear trend with y-intercept (Φ) of 1 and x-intercept (ρ_T) of ρ_S , the true density of the solid with no porosity. Different volcanic rock suites will have different x-intercepts because they have intrinsically different compositions and hence densities.

Figure 2.4 develops this concept using values of Φ_{Conn} (Fig. 2.4a) versus Φ_T (Fig. 2.4b). The data show significantly more scatter in Figure 2.4a. In particular, plotted as Φ_{Conn} , the samples of dacite from Mount Meager are inconsistent with a straight line model suggesting different rock compositions. However when the same data are plotted as Φ_T they fit a line of the form of Eq. (2.6). Note that although the Ring Creek suite forms a clear trend, it does not extrapolate to a y-intercept (Φ_T) of 1 (corresponding to 100% air when the rock has no mass) with either set of porosity values. This indicates a small but systematic variation in solid density likely due to a correlation between mineralogy (e.g., % glass) and porosity.

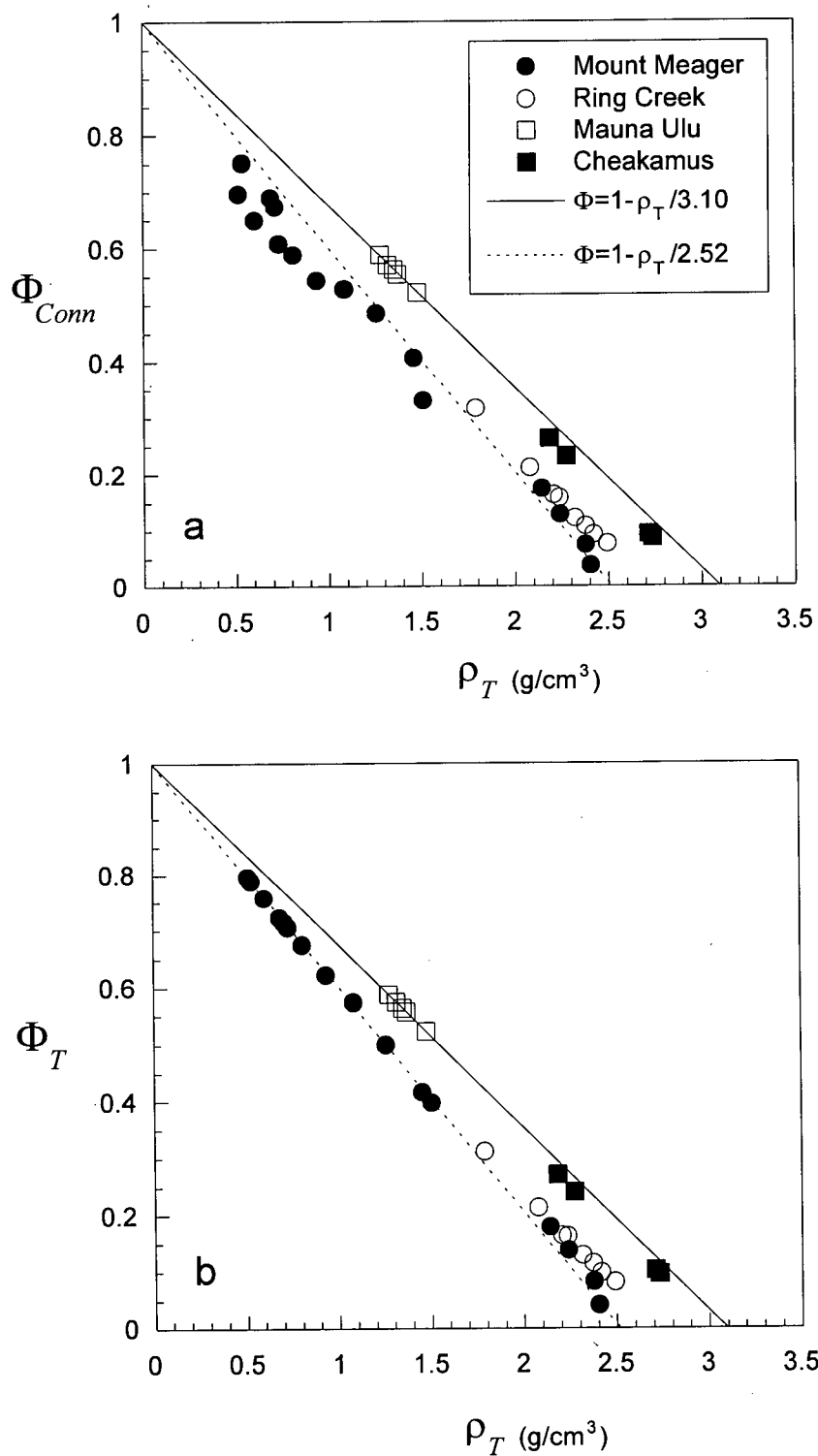


Figure 2.4 Values of Φ_{Conn} (a) and Φ_T (b) are plotted against ρ_T . Fits to data extrapolate to values of solid density of 3.10 g/cm^3 and 2.52 g/cm^3 (see text).

2.5 Measurement of K'

Capacitance data were collected with an HP4192A impedance analyzer using modified methods of R. Knight and co-workers in the Rock Physics Laboratory at The University of British Columbia (e.g., Knight and Nur, 1987; Knight and Abad, 1995). To make capacitance measurements, the dielectric material (rock) is placed between two parallel conductive plates (electrodes). Capacitance is a measure of the charge polarization that occurs in the sample between the plates. Dielectric constant (K') is the ratio of the capacitance with the dielectric material between the plates to the capacitance with a vacuum between the plates. Dielectric constant is calculated from capacitance (C) by:

$$K' = \frac{Cd}{\epsilon_0 A} \quad (2.7)$$

where A and d are the area and the separation of the electrodes, respectively, and ϵ_0 is the permittivity of free space (8.554×10^{-12} F/m). Sample disks are approximately 5 cm in diameter and 0.5 cm thick. Dielectric constant data were collected at 25 frequencies over the interval 10 kHz to 10 MHz.

Experimental Procedure

The standard procedure in the Rock Physics Laboratory at The University of British Columbia is to form electrodes (capacitors) by sputtering gold on the top and bottom faces of the sample disks. This method could not be used in the present study because many of the samples are extremely porous (up to 80% pores) and/or contain large pores. Gold sputtering of the samples would have resulted in electrodes which deviated significantly from ideal

parallel plates. The surface area of gold on a pumice sample, for example, would be much greater than the area calculated from the diameter of the disk. Also, the distance separating the electrodes would not be constant and in some cases would be substantially less than the height of the disk measured with callipers. Lastly, a few samples have pore networks which directly connect the upper and lower surfaces of the sample discs. Sputtering such samples may form a "gold path" connecting the upper and lower electrodes rendering dielectric constant measurement impossible.

Several electrode configurations were tested on five samples having variable porosity, as well as on a non-porous material of known dielectric constant (STYCAST HiK; $K'=6$).

The different electrode forms included:

- 0.85 mm thick copper disks
- 0.025 mm thick silver foil
- silver paint on copper disks or silver foil
- saline electrolyte-aqueous polymer gel (generally used to attach electrodes to skin) on copper disks or silver foil

Where wet silver paint or gel was used to couple the copper disks or silver foil to the sample, it was applied to the metal rather than the rock to ensure an even distribution of paint and minimize the amount of conductive material entering pores. Prior to all measurements, the impedance analyzer was tested on a platinum-sputtered STYCAST HiK ($K'=15$) disk with the same dimensions as the sample suite. Once placed in the sample holder and attached to the impedance analyzer, differences between repeated capacitance readings were insignificant for all electrode configurations tested.

The dielectric constant at low frequencies (below 10-100 kHz) was found to be extremely sensitive to the electrode configuration; however, at higher frequencies most methods converged to the same values of K' . Electrodes comprising copper disks or silver foil without Ag paint or gel as adhesive consistently produced the lowest values of K' . This is attributed to air gaps due to poor contact between the sample and the electrodes. When Ag paint was added (between sample and metal) higher dielectric constants were observed and using saline gel rather than Ag paint produced still higher values. Electrode configurations involving gel were rejected because measured values of K' for STYCAST HiK were always significantly higher than the reference value ($K'=6$).

In the end all data were collected using copper disks coupled to the sample with silver paint. I chose this method because: the procedure generated consistent, reproducible results, the copper discs are easier to handle than foil and the method reproduced the accepted value for the STYCAST HiK ($K'=6$) standard to within 4% over the entire range of frequencies measured (10kHz to 10 MHz). I also measured dielectric constant of four volcanic samples using silver foil in place of the copper disks; these two electrode configurations agree to within 1.4% at 10 MHz.

Although all samples were cored with the same bit, average disk diameters varied from ~48 mm to 50.5 mm due to drill movement and contrasts in rock competency. Three pairs of copper disks of different diameters were made. The electrodes for each sample used the largest pair of copper disks whose diameter did not exceed that of the sample. The area used in Eq. (2.7) is the area of the copper disk rather than the sample area. The entire circular surfaces of six of the low porosity samples (MM1, MB1, RC2, RC9, CB5a, and CB5b) were

coated with silver paint (no copper disks) and the entire area of the sample used in Eq. (2.7). In general, the dielectric constant determined using copper disks and silver paint is higher at lower frequencies and lower at higher frequencies than for silver paint alone (over the entire surface) but the deviation is less than 3% at 10 MHz except for a single outlier (MB1, ~8% difference).

K'-Frequency dependence

K' is a measure of polarizability and different polarization mechanisms dominate at different frequencies. The dominant mechanism at GPR frequencies is dipole polarization; at lower frequencies interfacial polarization (Maxwell-Wagner effect) can be important. The latter mechanism occurs in heterogeneous materials and is caused by charge accumulations along interfaces when an electric field is applied (Howell and Licastro, 1961).

The measured values of dielectric constant for all samples are shown as a function of frequency in Figure 2.5. Samples have higher dielectric constants at lower frequencies and decrease to a near-constant K' value at frequencies above 0.1-1 MHz. Notable exceptions are MB1 (a glassy clast from a "Merapi-style" breccia), CB7a and CB7b (scoria from the base of a basalt lava flow), and to a lesser degree all Mauna Ulu samples (Fig. 2.5b). Samples MB1 and CB7a,b have significantly higher dielectric constants than other samples from the same deposits (Fig. 2.5 and 2.6a). Furthermore, for these samples, the measured values of K' do not level off at higher frequencies suggesting that the high values of K' reflect interfacial polarization, although this mechanism usually contributes little to K' in dry rocks. The Mount Meager outlier (MB1) has the same mineralogy as the rest of the Mount Meager suite

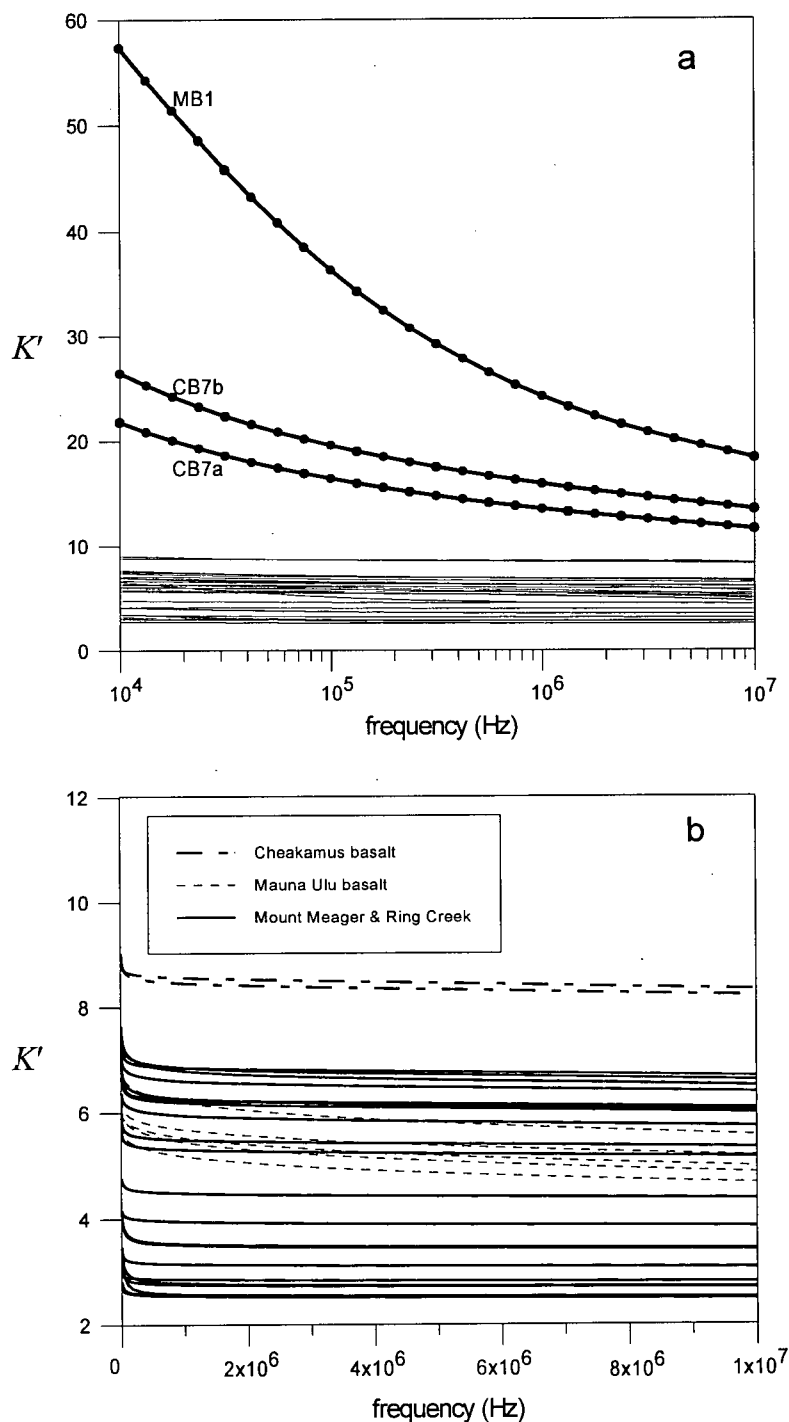


Figure 2.5 Measured values of K' plotted as a function of frequency. a) Sample MB1, CB7a and CB7b show greater frequency dependence and significantly higher dielectric constants than the rest of the sample set. Data points (filled circles) are shown for these three samples; K' measurements were made at the same 25 frequencies for all samples. b) Samples with lower values of K' (< 10) are plotted against a non-logarithmic frequency scale.

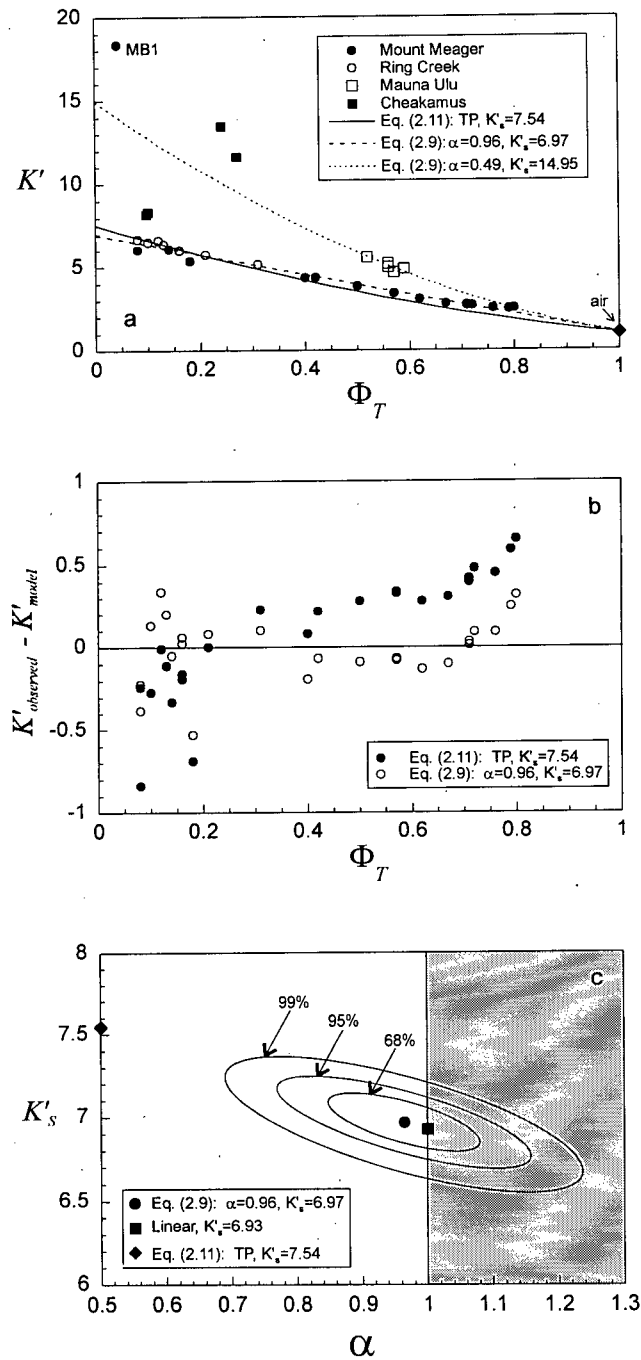


Figure 2.6 Plots of K' versus Φ . a) Experimental data from this study and fitted curves: Eq. (2.11) (TP, $K'_s=7.54$) fitted to MM-RC data; best fit of Eq. (2.9) to the MM-RC data ($K'_s=6.97, \alpha=0.96$) (i.e., Eq. 2.13); best fit of Eq. (2.9) to the Mauna Ulu suite ($K'_s=14.95, \alpha=0.49$). b) Plot of residuals for the two curves (Eq. 2.9 and 2.11) fitted to the MM-RC data set. c) Confidence limits for two parameter fit (Eq. 2.9) to MM-RC data set show the TP model ($\alpha=0.5$) to be outside the region of three standard deviations of uncertainty on the fit parameters. The linear model (volume average), however is within one standard deviation. The shaded region represents physically unrealistic solutions for the dipolar dielectric constant of a heterogeneous mixture.

but it is unique in that its pore spaces are almost exclusively in the form of cracks. It could be that the cracks host a thin ($\sim 10\text{\AA}$) layer of adsorbed water, the presence of which has been shown to increase dielectric constant (Knight and Endres, 1990). A similar argument does not hold for the Cheakamus samples as the porosity is mainly in the form of primary vesicles.

2.6 Relationship between Φ and K'

Comparisons of dielectric constant with porosity (Fig. 2.6a, 2.7) and bulk density (Fig. 2.8) are made with the highest frequency data (10 MHz). The suite with the most complete porosity spectrum is from Mount Meager. The data (excluding MB1) form a smooth and definite pattern in $K-\Phi_T$ space of increasing dielectric constant with decreasing porosity. The trend for Ring Creek data is approximately equivalent to that formed by the more felsic Mount Meager samples and, thus, the two suites are modeled as a single data set. The Mauna Ulu basalt samples show a similar pattern but define a distinct trend relative to the Mount Meager-Ring Creek samples and are therefore treated separately. There are not enough Cheakamus basalt samples to form a coherent trend and these data were not modeled. Because the Mount Meager and Ring Creek suites span the greatest porosity, further discussion concentrates on this combined data set (excluding the outlier, sample MB1), henceforth referred to as the MM-RC data set.

A simple approach to modeling dielectric constant of a heterogeneous material is to calculate the total dielectric constant (K_T') from the volume fraction (θ_i) and dielectric constant (K_i') of each of the i components using a model of the form:

$$(K_T^*)^\alpha = \sum \theta_i (K_i^*)^\alpha \quad (2.8)$$

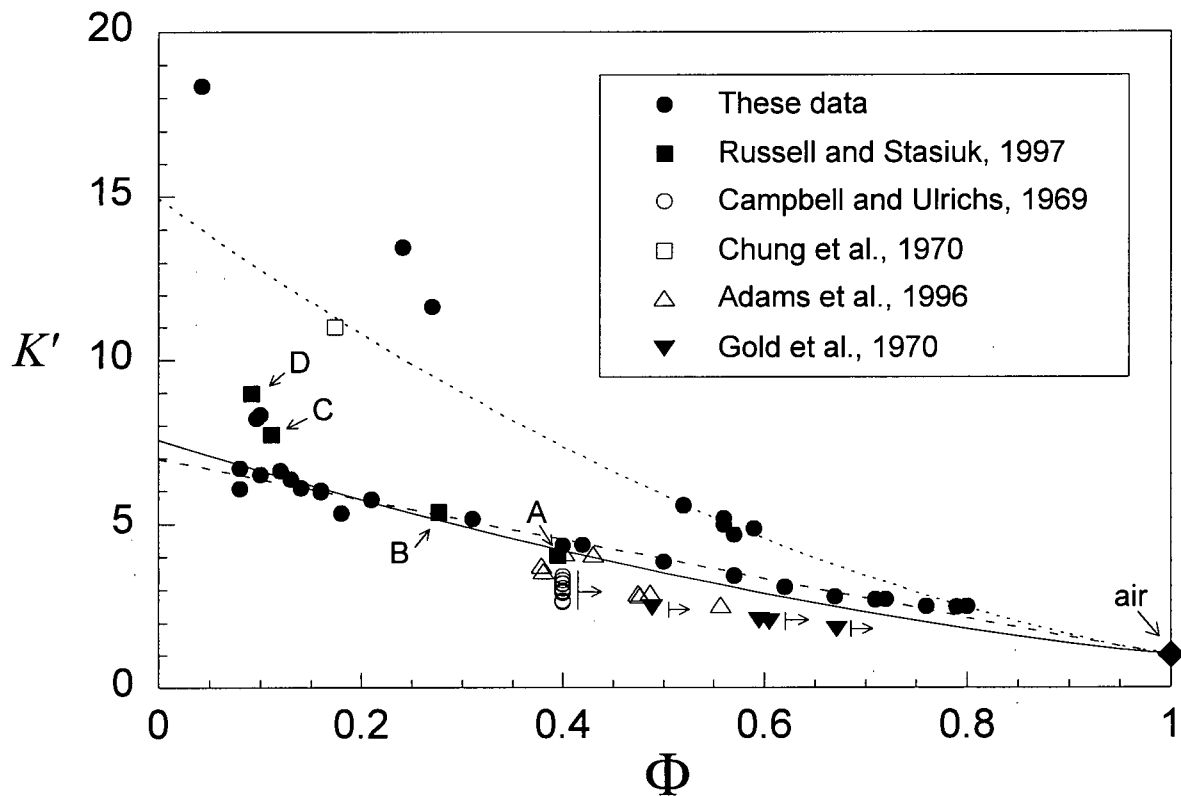


Figure 2.7 Comparison of new data (porosity values represent total porosity) and results from other sources (porosity values are not necessarily total porosity). Arrows attached to vertical lines indicate that porosities are minima but there is no significance to the arrow lengths. See text for details and explanations of labels. Model curves plotted are identical to those in Fig. 2.6.

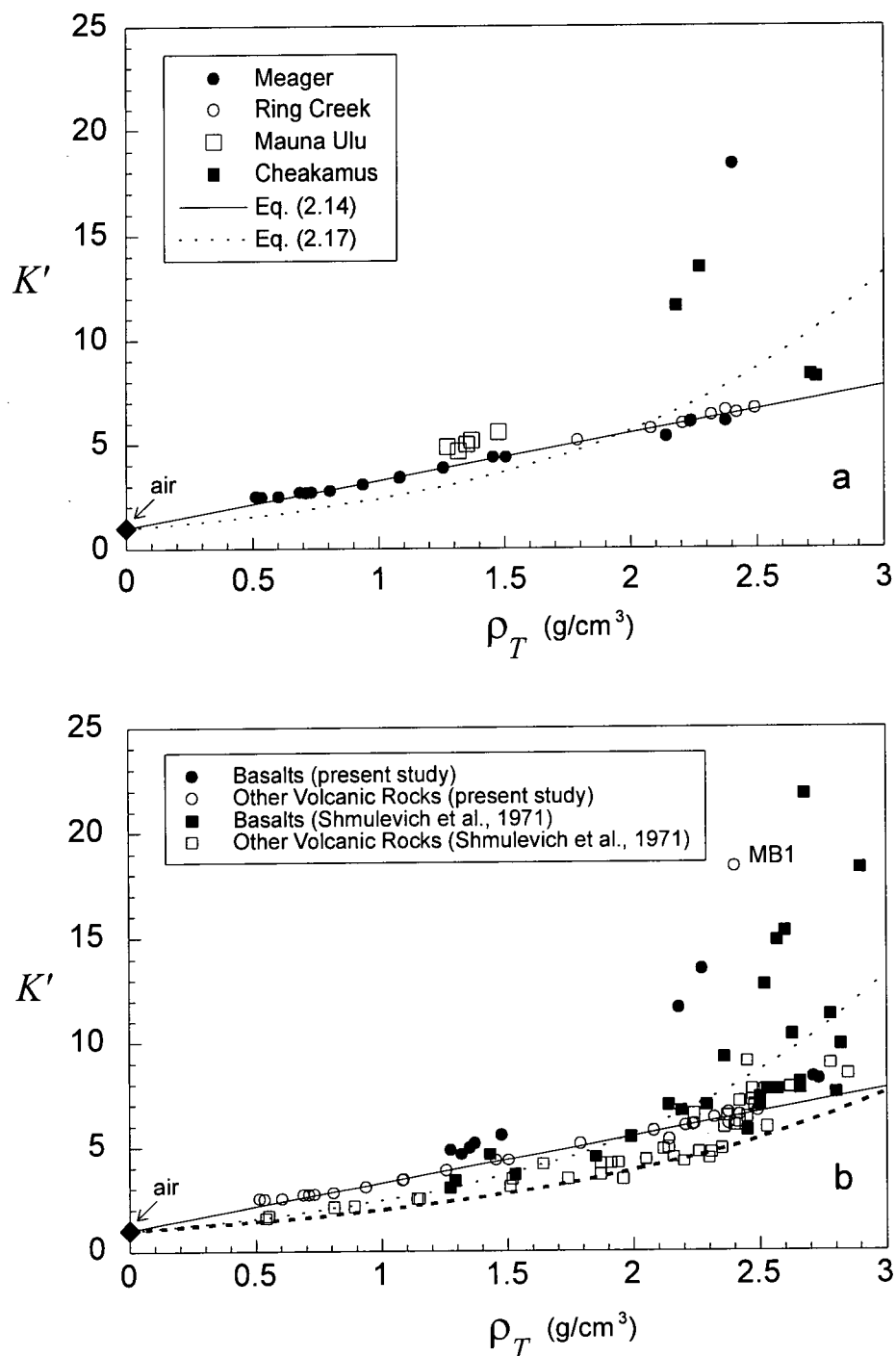


Figure 2.8 Plots of K' versus ρ_T . a) Experimental data from this study shown against two models fitted to the MM-RC data: Eq. (2.14) is the best straight line through theoretical value for air, and Eq. (2.17) is the best fit curve of the form used by Ulaby et al. (1990) and Olhoeft and Strangway (1975) (Fig. 2.1). b) Comparison of data from this paper to data of Shmulevich et al. (1971). Volcanic data are grouped as basalts and other volcanics. Heavy dashed line is model derived from Ulaby et al. (1990) data, also plotted in Fig. 2.1.

where K^* is the complex dielectric constant and α is a geometrical factor. This is known as the Lichtenecker-Rother (1931) equation. The theoretical lower and upper limits of dipolar dielectric constant for a heterogeneous mixture occur where the components are arranged in series ($\alpha=-1$) and in parallel ($\alpha=1$), respectively. When the components are non-conducting, as is assumed for the air and the solid in the samples used in this study, K^* can be approximated by K' to yield:

$$(K_T')^\alpha = \sum \theta_i (K_i')^\alpha \quad (2.9)$$

A commonly used model of this type is the time propagation (TP) model (Wharton et al., 1980):

$$\sqrt{K_T'} = \sum \theta_i \sqrt{K_i'} \quad (2.10)$$

In principle, one could build up the effective dielectric constant of a rock by taking into account the constituent minerals, glass, and air. Here I consider each sample as a mixture of air ($K'_{air}=1$) and a non-porous solid with a fixed dielectric constant K'_s , the expanded form of TP is:

$$\sqrt{K_T'} = \Phi_T + (1 - \Phi_T)\sqrt{K'_s} \quad (2.11)$$

The general least squared-residuals best fit of Eq. (2.11) for the MM-RC data set gives $K'_s = 7.54$ (Table 2.3). This curve is plotted in Figure 2.6a.

TP fits the MM-RC data well (Table 2.3); however, a plot of residuals (Fig. 2.6b) shows a systematic distribution. Part of this deviation from the model, particularly the large

residuals at high porosities, could be due to pore size and shape variation as TP does not take into account the geometry of the components. Alternatively, I have fit the data to Eq. (2.9) solving for both K'_s and α by minimization of the χ^2 function:

$$\chi^2 = \sum \frac{[K'_i - (K'(K'_s, \alpha))]^2}{\sigma_i^2} \quad (2.12)$$

(Press et al., 1986) where σ_i is the mean uncertainty on the measured values of K'_i . The optimal solution, $\alpha=0.96$, and $K'_s=6.97$:

$$(K'_T)^{0.96} = \Phi + 6.97^{0.96}(1 - \Phi) \quad (2.13)$$

fits the data very well (Table 2.3, Fig. 2.6a). Furthermore the residuals associated with this model show that the two parameter model is substantially better than the TP model for describing these data (Fig. 2.6b). Figure 2.6c shows the 1s, 2s, and 3s (or 68, 95, 99%) confidence limits on the model solutions and demonstrates clearly that a TP model ($\alpha=0.5$) lies outside the reasonable solution space. The α value for MM-RC data (0.96) is very close to the theoretical upper limit ($\alpha=1$) which is strictly linear. A linear model constrained to pass through the theoretical value for air, has the fitted parameter $K'_s=6.93$ (Table 2.3) and corresponds, in principle, to an arrangement of columns of rock and air perpendicular to the electrodes. Clearly, this is not an accurate description of the pore geometry of the entire MM-RC sample set. However, the Mount Meager pumice pores can be larger than, or of similar dimensions to, the thickness of the sample disks (0.5 cm), and the samples may be approaching a parallel arrangement at high porosities. The presence of such pores could explain why TP does not model these data as well as other data sets.

Table 2.3 Parameters to model lines describing K' -porosity data.

Data set	Model	K'_s	α	R^2
MM-RC	TP: Eq. (2.11)	7.543	0.5*	0.979
MM-RC	Two-parameter fit: Eq.(2.9), (2.13)	6.965	0.965	0.985
MM-RC	Linear, through (0,1)	6.927	1*	0.984
Mauna Ulu	TP: Eq. (2.11)	14.768	0.5*	0.833
Mauna Ulu	Two-parameter fit: Eq.(2.9)	14.955	0.488	0.833

*fixed value required by model

The Mauna Ulu basalt data were fit by least-squared residuals to the same models as the MM-RC data set (Table 2.3). TP (Eq. 2.11) gives $K'_s=14.77$ suggesting that the solid phase of the Mauna Ulu suite has a dielectric constant approximately double that of the Mount Meager and Ring Creek suites. The two-parameter fit (Eq. 2.9) has optimal values $K'_s=14.95$, $\alpha = 0.49$ which is essentially the same as TP ($\alpha=0.5$) and is also plotted in Figure 2.6a.

Comparison with previous results

Figure 2.7 combines information from Figures 2.2 and 2.6a by superimposing the new $K'-\Phi$ data on previous results. The data of Russell and Stasiuk (1997), labeled A through D, clearly agree with the data presented here, although Russell and Stasiuk (1997) used gold-sputtered surfaces as electrodes and only measured connected porosity. In particular, two samples of porous intermediate volcanic rocks (A and B) lie on the trend formed by Mount Meager and Ring Creek samples. Point D represents a sample of basalt from the same outcrop as sampled in this study (e.g. Cheakamus). It plots relatively close to correlative samples in this study. These results indicate that the copper disks with silver paint electrodes give similar results to gold sputtering at low and moderate porosities. Point C is equivalent to the outlier MB1 of the present study but unlike MB1, its porosity is not dominated by cracks. The large gap in K' between samples C and MB1 is consistent with the abnormally high value for MB1 being related to its pore geometry.

The data from Campbell and Ulrichs (1969), Gold et al. (1970) and Adams et al. (1996) deviate from the trends defined by my data. There are several possible explanations

for this disparity. Firstly, there are significant differences in rock composition. Secondly, the three previous studies measured K' on samples of powdered rock or natural ashes and, thus, the pore geometries would be substantially different from those found in the Mount Meager pumice samples. Thirdly, the porosities reported by Campbell and Ulrichs (1969) and Gold et al. (1970) are minima because it was assumed that the rocks from which the powders were crushed were non-porous. Finally, the data derived from the three previous studies were collected at much higher frequencies (450 MHz to 19 GHz versus 10 MHz for the present study).

2.7 Relationship between ρ_T and K'

Plots of K' vs. total porosity (Fig. 2.6a) and K' vs. bulk density (Fig. 2.8a) are approximately mirror images of each other. This is not surprising as, for small variation in ρ_S , there is a simple relationship between porosity and bulk density (Eq. 2.6). The basalts (Cheakamus and Ulu) have higher dielectric constants than the more acidic rocks (Mount Meager and Ring Creek) of similar porosity but the basalts also have higher ρ_S values (Fig. 2.4, Table 2.2). Bulk density is dependent on both Φ and ρ_S , and plotting K' vs. bulk density rather than porosity brings the data for basalt samples closer to the trend defined by MM-RC samples (Fig. 2.8a). However, the MM-RC and Ulu trends are still distinct in (ρ_T, K') space and only the MM-RC data set is modeled.

The MM-RC trend is remarkably linear (Fig. 2.8a). The best fit of a straight line constrained to pass through (0,1) is:

$$K' = 2.26\rho_T + 1 \quad (R^2=0.990) \quad (2.14)$$

Although the straight line fit is entirely empirical, it has two attributes: a) it describes all of these data well (excluding MB1 and basalts), and b) it offers a very simple model for making rapid estimates of K' for non-basaltic, dry, volcanic rocks based on a single measurement: ρ_T .

For the purposes of comparison, the MM-RC data were also fitted with a curve of the form used by Olhoeft and Strangway (1975) and Ulaby et al. (1990). Fits by Olhoeft and Strangway (1975) and Ulaby et al. (1990) relating K' to ρ_T -data, are based on a logarithmic addition formula (Lichtenecker and Rother, 1931):

$$\log(K'_T) = \sum \theta_i \log(K'_i) \quad (2.15)$$

Treating the system as a mixture of air and non-porous rock, (Eq. 2.15) simplifies to:

$$K'_T = K'_s^{(1-\Phi_T)} = K'_s \frac{\rho_T}{\rho_s} \quad (2.16)$$

Assuming ρ_s is constant, K' can be related to ρ_T as was done by Ulaby et al. (1990) and Olhoeft and Strangway (1975) (Fig. 2.1). The resulting fit for the MM-RC data is:

$$K' = 2.22^{\rho_T} \quad (2.17)$$

This curve is plotted in Figure 2.8a. The solution predicts higher K' for a given ρ_T than the models of Ulaby et al. (1990) and Olhoeft and Strangway (1975) (Eq. 2.2 and 2.3); however, the best fit to my experimental data is the linear model (Eq. 2.14).

Comparison with previous results

Figure 2.8b compares the (K' , ρ_T) data from this paper to data for 68 volcanic rocks measured by Shmulevich et al. (1971) (e.g., Fig. 2.1). Plotted as K' vs. ρ_T , the present study shows higher K' for a given bulk density than most of the volcanic samples measured by Shmulevich et al. (1971) (Fig. 2.8b). This is particularly true at low bulk densities (high porosities). Part of this disparity is due to the difference in measurement frequency (500 MHz vs. 10 MHz). The scaling problem of large pores compared to sample thickness may also be contributing to the higher K' of the new experimental data at high porosities.

The Shmulevich et al. (1971) data show a large spectrum of dielectric constants for basaltic rocks; indeed most of the dispersion in the K' - ρ_T trend is due to basaltic samples (Fig. 2.8b). The number of basalts in the present sample set is limited. Although the Mauna Ulu samples show a clear trend of increasing dielectric constant with decreasing porosity, the span of porosities is too small to model accurately. The Cheakamus basalts would not fit any air-rock mixing laws as the more porous samples (CB7a,b) from the base of the flow have much higher dielectric constants than the massive flow samples (CB5a,b). Perhaps the higher and more varied modal abundances of Fe,Ti oxides (magnetite, ilmenite, titanomagnetite) in basalts is responsible for the greater variance. Excluding all basalt samples, the results of this study parallel those of Shmulevich et al. (1971) and produce a single trend which can relate porosity or density to dielectric constant (Fig. 2.8b).

2.8 Applications and limitations of results for GPR

One of the attributes of this study is that I have established a clear relationship

between Φ and K' for dry, non-basaltic volcanic rocks over a wide range of porosities. The results indicate that inverse modeling techniques could be applied to ground penetrating radar (GPR) velocity data to derive estimates of porosities or map changes in porosity of dry volcanic deposits. One possible application is to map zones of welding in partially welded pyroclastic flows. The welded zones are composed of the same material as unwelded tops and bases but have lower porosity because slower cooling rates in the middle of the deposit provide sufficient time for hot clasts to flatten and thereby reduce porosity. If the change in porosity is gradational, a single, strong continuous reflection may not be generated (e.g., defining some critical porosity). However, by using CMP analysis, changes in velocity with depth could be determined and converted into a porosity profile.

Some caution should be taken in applying laboratory results directly to the interpretation of GPR data. Three main reasons are that: 1) the highest frequency used in these laboratory measurements is 10 MHz and this is significantly below conventional GPR frequencies for geological applications (e.g., 50-200 MHz), 2) there may be a problem in upscaling laboratory dielectric measurements on rock samples to the scale of deposits due to spatial heterogeneity (Chan and Knight, 1997), and most importantly, 3) in nature, the pore space may be partially saturated with water which could drastically alter the dielectric properties of a deposit because of the large contrast between K'_{water} (80) and K'_{air} (1).

Although GPR has been used in geological studies since the 1960s, its application to problems associated with volcanic deposits is in its infancy. GPR will never replace traditional stratigraphic mapping but rather should complement it by extending observations of physical properties, distributions, thicknesses and internal structures to areas which lack

exposure. In order to realize the full potential of GPR, a better understanding of the factors that contribute to the dielectric constant of volcanic rocks is paramount. The development of an empirical model relating porosity and dielectric constant of dry, non-basaltic volcanic rocks is an important step. Further work incorporating such factors such as mineralogy (e.g., ilmenite mode), pore and mineral geometries, and water content are required to enhance the simple models presented here.

Chapter 3

Detection and mapping of welding in pyroclastic flows with GPR: Forward modeling results

3.1 Introduction

Porosity, or vesicularity, is a first order, primary physical property of volcanic deposits. Porosity variation relates to the type of deposit (e.g., pyroclastic deposits vs. lava flows), to stratigraphic position within an individual unit (e.g., flow top vs. flow interior), and to lateral facies changes (e.g., proximal vs. distal lava flows). Chapter 2 showed a strong correlation between the degree of vesicularity of volcanic rocks and their dielectric properties. Specifically I used laboratory measurements on dry, non-basaltic samples of volcanic material to develop the following relationship between porosity (Φ) and dielectric constant (K'):

$$(K')^{0.96} = \Phi + 6.97^{0.96}(1 - \Phi) \quad (3.1)$$

These results have import for the potential of GPR as an aid to volcanological studies as K' is the primary physical property controlling the velocity of radar through low loss material:

$$V = \frac{c}{\sqrt{K'}}, \quad c = 3 \times 10^8 \text{ m/s} \quad (3.2)$$

Indeed, these laboratory results, in conjunction with Eq. 3.2, suggest that there is great potential to constrain the actual or relative porosities of volcanic deposits using GPR.

Specifically, radar data from the field elucidate variations in dielectric properties of deposits; in volcanic rocks these variations in K' can commonly be related to differences in porosity.

Pyroclastic flow deposits represent an obvious target for this type of survey because welding of pyroclastic flows can cause substantial variations in porosity. Pumice clasts and shards within hot, thick pyroclastic flows collapse, flatten and anneal under the weight of overlying material, causing substantial porosity reduction in the interiors of the deposits (Fig. 3.1). For example, the porosity of the Battleship Rock ash-flow tuff ranges from 70% at the top and base of the unit, to 24% in the interior of the deposit (Ross and Smith, 1961). The process of welding can produce considerably lower porosities (e.g., 3.4%; Marshall, 1935 *in* Ross and Smith, 1961). These changes in porosity suggest substantive changes in the dielectric properties of the deposit and, therefore, should be mappable with GPR.

In this paper I investigate the potential and the limitations of using GPR to delineate and trace welded portions of pyroclastic flows. This is accomplished with numerical modeling of electromagnetic wave propagation through two subsurface K' models that derive from porosity profiles of a pyroclastic flow. Furthermore, I use a case study comprising GPR data collected at a well exposed, welded pyroclastic flow in central Oregon to test ideas derived from my model results. Two possible approaches to detecting and mapping welding are considered: i) identification of characteristic signals or textures in radargrams for unwelded to strongly welded facies; ii) tracing of strong, continuous reflections produced by rapid porosity changes bordering welded zones.

3.2 Subsurface model profiles

I have used data of Freunt and Schmincke (1995) to construct model profiles of welded pyroclastic deposits. Their study of a welded basaltic ignimbrite on Gran Canaria

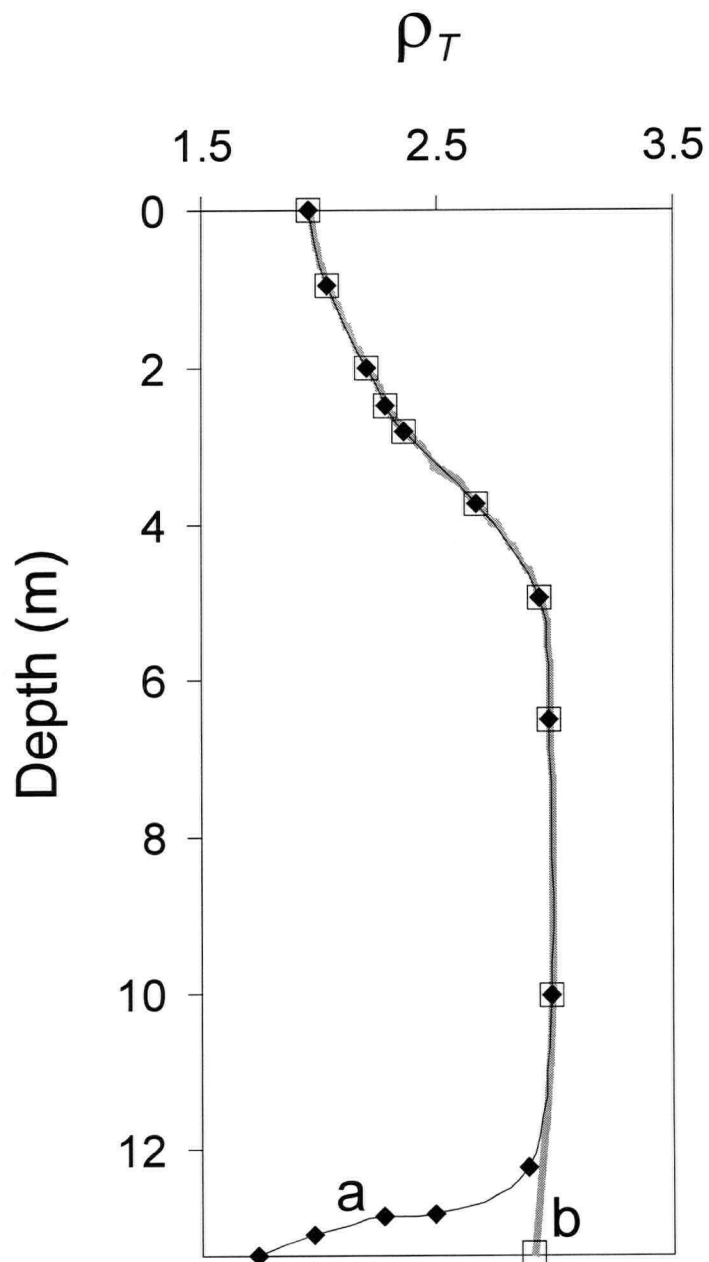


Figure 3.1 Bulk density (ρ_T) versus depth profiles for a basaltic ignimbrite at Playa de Tasarte, Gran Canaria (after Freunt and Schmincke, 1995): a) profile over cold ground shows unwelded base (thin line and solid symbols); b) profile over hot ground shows welding to base (heavy line and open squares).

produced bulk density (ρ_T) profiles which are well constrained by abundant measurements of ρ_T and classic in shape. I chose two of these profiles (Fig. 3.1) for my forward modeling. The profiles differ only at the base: one section showed the ignimbrite to be unwelded at the base, whereas, the other section was welded to the very base of the deposit.

Although the shapes of the Playa de Tasarte profiles are ideal for my modeling, the unusual composition (basalt) of the pyroclastic flow is less than ideal. The empirical relationship between Φ and K' established by Chapter 2 (Eq. 2.13, Eq. 3.1) is applicable only to intermediate to felsic volcanic rocks. Basaltic tephra have different dielectric properties. Thus, although I have used the Φ profiles of the Gran Canaria deposit (calculated from ρ_T data) I have treated the deposit as dacitic in composition in the calculation of K' profiles. In short, these results are for a dacitic flow with the porosity distribution of the basaltic Gran Canaria deposit.

The porosity profiles (e.g., Fig. 3.2a) were constructed from the ρ_T profiles by assuming a fractional porosity (Φ) of 0.05 (i.e., 5%) for the most densely welded part of the flow ($\rho_T = 2.98 \text{ g/cm}^3$). Using these ρ_T , Φ values and assuming that the solid (void-free) density (ρ_S) does not change with depth, the solid density is calculated from:

$$\Phi = \frac{\rho_S - \rho_T}{\rho_S} \quad (3.3)$$

Knowing ρ_S , each published bulk density value (Fig. 3.1) is then converted to Φ by Eq. (3.3). Figure 3.2a shows the porosity versus depth data that are interpolated by a curve constrained to pass through the calculated data.

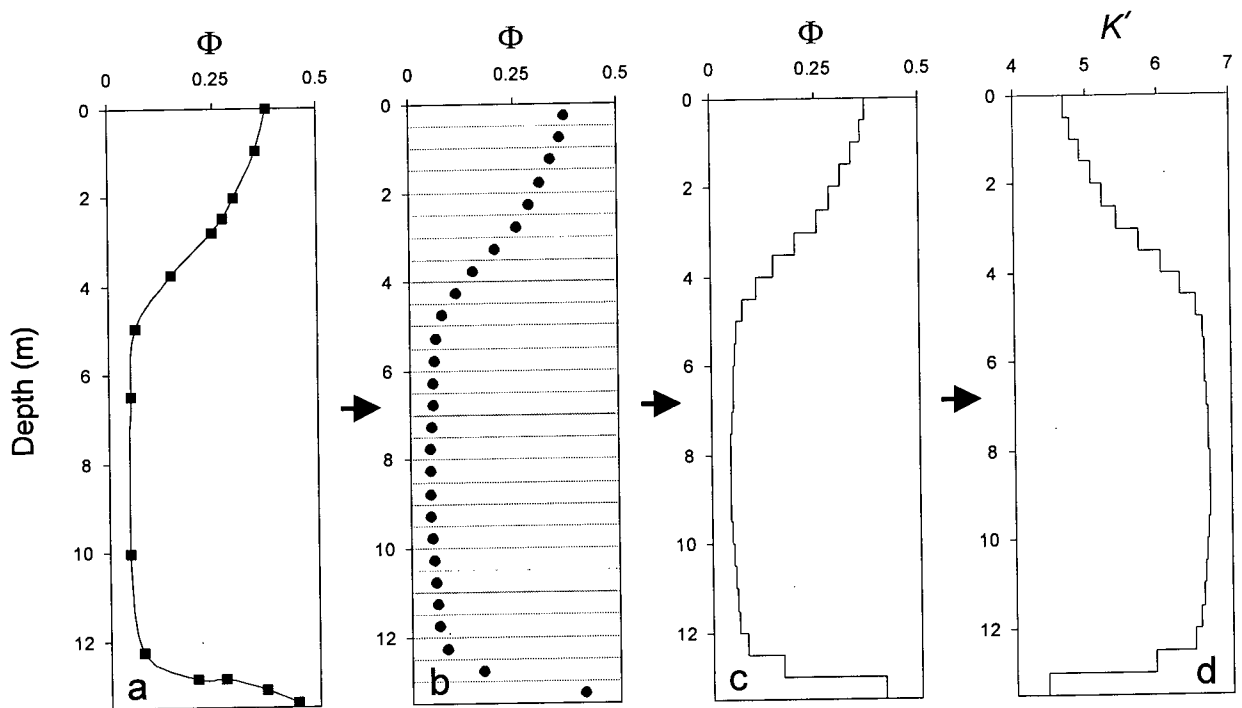


Figure 3.2 Schematic demonstration of steps in conversion from continuous porosity (Φ) profile to discretized profile of dielectric constant (K'): a) Solid line denotes curve fitted to data to create a continuous profile of Φ based on actual data points (squares) in Figure 3.1a (see text); b) Φ profile is divided into layers of equal thickness (e.g., $L = 50$ cm) and solid circles show Φ values at the center of each layer interpolated from curve in 2a; c) Layered Φ profile: each layer assigned the interpolated Φ value from 2b. d) Layered K' profile constructed by converting Φ to K' values with Eq. (3.1).

I have approximated the continuous porosity profile by a series of homogeneous layers. This discretization involves dividing the profile into layers of constant thickness and assigning each layer the porosity corresponding to the depth at the center of the layer. This is illustrated in Figure 3.2 b,c where the continuous profile is divided into 27, 50 cm-thick layers. This layered porosity profile (Fig. 3.2c) is then converted into a layered K' profile using Eq. (3.1). The resulting variations in K' are shown in Figure 3.2d. Figure 3.3 comprises K' profiles for layers 1 cm thick, with a 10 m thick layer of $K'=7$ added to the base of the ignimbrite. This layer represents a uniform, homogeneous substrate.

3.3 Critical layer thickness (L_c)

I have modeled actual gradational changes in porosity (and K') of the welded pyroclastic flow by a series of homogeneous layers. It is essential that the layers are sufficiently thin to ensure that the radar wave interacts with the actual K' profile and not an artificial profile generated by the discretization process. Schematic, zero-phase Ricker source wavelets are shown in Figure 3.3c with wavelengths (λ) scaled to the axes of Figure 3.3a,b to allow comparison between the range of wavelengths used in the simulations and the thickness of discrete layers. Where a "high" frequency (f), small wavelength pulse is propagated through a subsurface model with "large" layer thickness (L), each layer is resolved and a reflection is produced at each interface. For example, in a simulation through profile a (Fig. 3.1-3.3) with $L=100$ cm and $f=200$ MHz (upper left corner, Fig. 3.4), a reflection (trough-crest-trough or crest-trough-crest) forms at every interface with zones of zero amplitude between these reflections. As λ/L is increased either by a decrease in layer

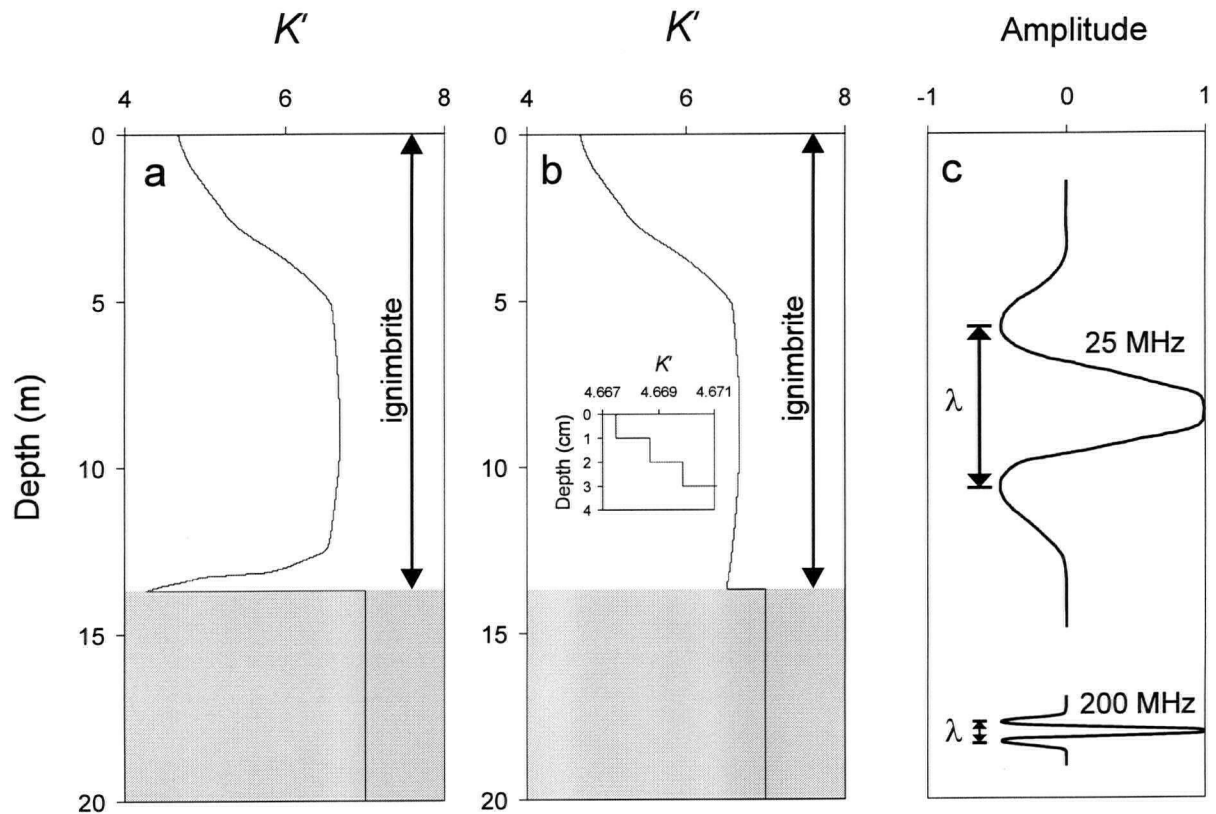


Figure 3.3 Discretized profile of K' using 1 cm thick layers. Profiles are the K' equivalents of the ρ_T profiles in Fig. 3.1 overlying a 10 m thick layer of $K'=7$, and include: a) ignimbrite with unwelded base, b) ignimbrite with welded base. Inset is enlargement of top of profile showing actual discretized form of curve, and c) scaled wavelengths (λ) of the 25 MHz and 200 MHz source wavelets through a material with $K'=6$ (λ scaled to depth axes of a and b).

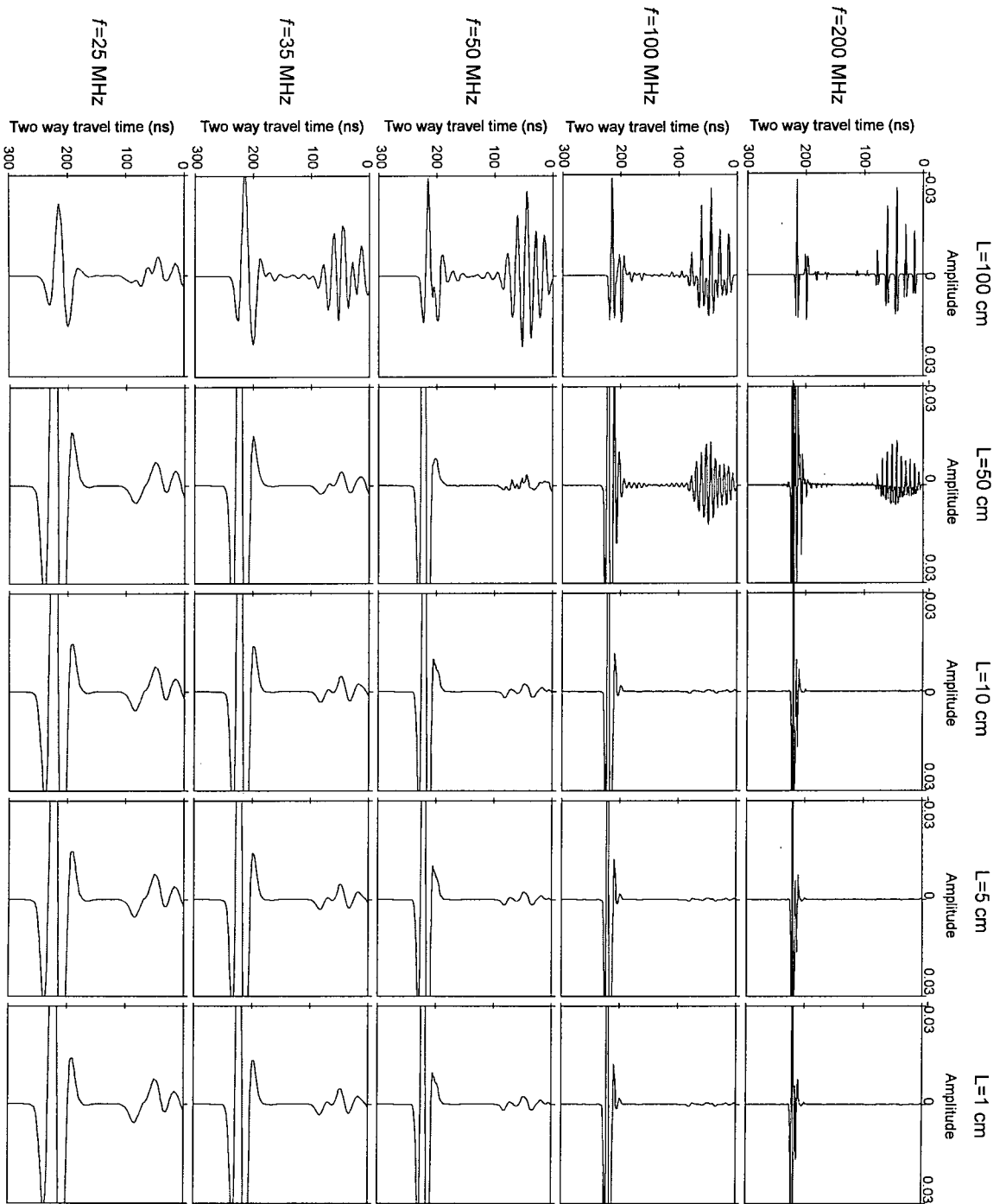


Figure 3.4 Simulations for profile a (Fig. 3.1-3) at a variety of frequencies (f) and layer thicknesses (L). The similar results for $L=1$ cm and $L=5$ cm support the notion that 1 cm layers adequately model the gradational profile for the frequencies of our simulations (see text).

thickness or frequency, reflections derived from the top and base of each layer begin to overlap and the layers cannot be resolved (Fig. 3.4).

For a given f and K' , there will be some critical layer thickness (L_c) such that further decreases in L do not produce significant changes in the resulting synthetic traces. In order to model gradations in porosity with homogeneous layers, it is crucial that $L \leq L_c$. An accepted criterion for vertical resolution is about $L = \lambda/4$ (Yilmaz, 1987). Therefore $L < \lambda/4$ is a minimum requirement for subsurface models. I have used 1 cm layers for the simulations presented in this paper (Fig. 3.5-3.7) which, for the range of frequencies (25 to 200 MHz) and dielectric constant values ($4 < K' < 7$) used, falls in the interval $\lambda/57$ ($f=25$ MHz; $K'=7$) to $\lambda/600$ ($f=200$ MHz; $K'=4$). Figure 3.4 shows that for a given frequency, amplitudes converge as L is decreased. Results for $L=1$ cm and $L=5$ cm are practically identical, corroborating the notion that 1 cm layers adequately model the gradational changes in physical properties of the pyroclastic flows modeled.

3.4 Forward Modeling Results

I have modeled the propagation of electromagnetic waves through the profiles shown in Figure 3.3 using a program developed by Steven Cardimona of the University of Missouri-Rolla. This program is based on wave propagation matrices (Ursin, 1983) and uses the propagator calculation method of Kennett and Kerry (1979). The simulations are run for 1 cm thick layers at five frequencies: 25, 35, 50, 100 and 200 MHz. All layers are given a magnetic permeability of 1 and conductivity of zero. Dacitic ignimbrites are, in fact, resistive but have non-zero conductivity. Setting conductivity to zero removes the imaginary

part of the complex dielectric constant and avoids the need to gain results to compensate for signal attenuation.

Figure 3.5 shows the synthetic traces resulting from the propagation of a 25 MHz wave of amplitude 1.0 through the two Playa de Tasarte profiles (a and b of Fig. 3.3). The traces show three distinct patterns: i) the first 115 ns exhibit abundant, relatively low amplitude reflections; ii) from 115 to 175 ns, the amplitude is essentially zero; iii) from 175 or 190 ns to 260 ns there are one or more strong reflections. Below 260 ns, the waveform has virtually no amplitude due to the thick homogeneous layer of $K'=7$ added to the base of the ignimbrite profiles. The three divisions of the synthetic trace correspond to: i) a zone of moderate increase in degree of welding (decrease in Φ and K' ; increase in ρ_T with depth); ii) a zone of dense welding with relatively constant physical and electrical properties; iii) the base of the flow preceded in profile **a** by a sharp decrease in degree of welding (increase in Φ and K' ; decrease in ρ_T with depth). The lowermost reflection (crest-trough-crest) is approximately centered at the basal contact of the pyroclastic flow, marked by the top of the stippled region.

The results for the two profiles (**a** and **b**) are coincident except for the last division (iii). This is because the K' profiles (Fig. 3.3) are identical except at the base of the flow. The three divisions of the 25 MHz traces (Fig. 3.5) are also seen in the higher frequency simulations although the two way travel times for the division boundaries shift somewhat. In all cases, there is a middle section (ii) of near-zero amplitude. Patterns and variations with changing frequency for the top (i) and basal (iii) sections are explored in Figures 3.6 and 3.7

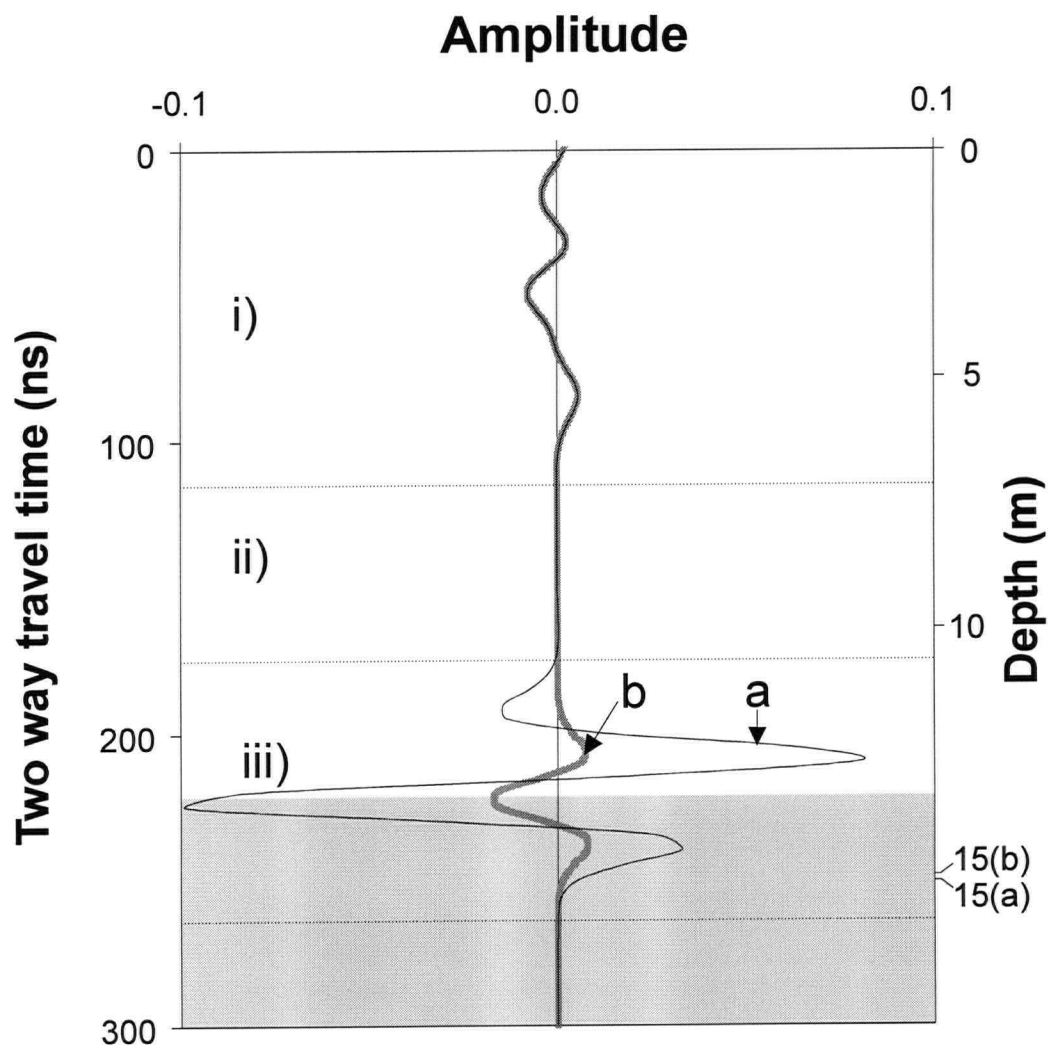


Figure 3.5 Synthetic traces resulting from modeling propagation of 25 MHz electromagnetic wave through the two (**a** and **b**) Playa de Tasarte sections (Fig. 3.3). The traces are divided into three sections: i) zone of abundant crests and troughs; ii) zone of zero amplitude signal; iii) simple, distinct reflection(s) marking the base of the flow. The two geological sections have coincident results down to 150 ns. The profile with the unwelded base (**a**) shows a higher amplitude reflection at the base of the flow (~220 ns) and an extra trough (~200 ns). Depths are calculated from input K' profiles using an effective medium theory found to give accurate average velocities for $\lambda/L < 1$ (Chan and Knight, 1997). Differences in K' near the base of the flow result in a slight disparity between the travel time corresponding to a depth of 15 m for profile **a** (15a) and profile **b** (15 b). The top of the stippled region indicates a depth of 13.38 m, the boundary of the pyroclastic flow and the $K'=7$ substrate as calculated from profile **a** K' values. The equivalent region for profile **b** begins 1.69 ns earlier.

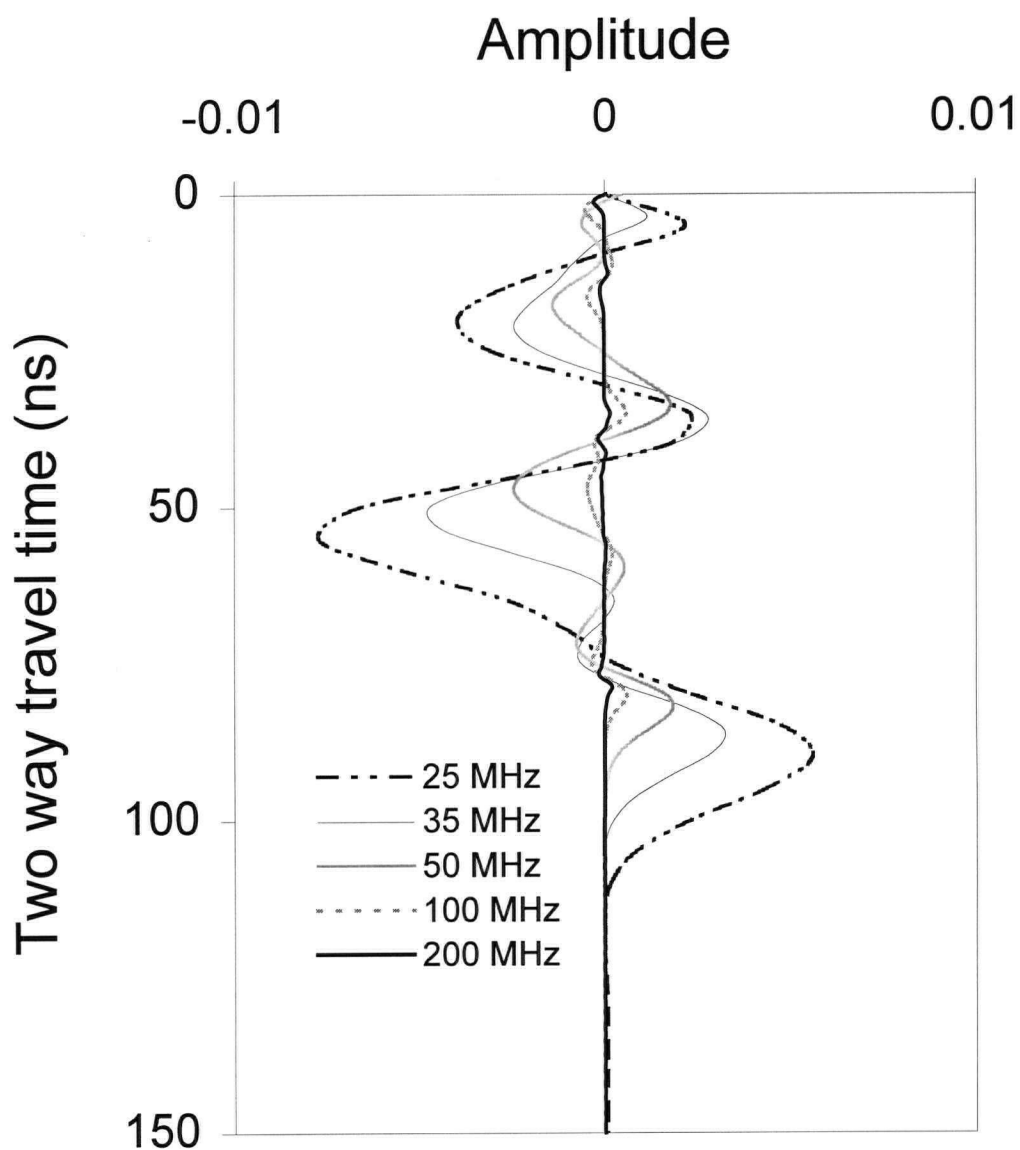


Figure 3.6 Synthetic traces (0-150 ns) resulting from modeling 25, 35, 50, 100 and 200 MHz waves passing through the two Playa de Tasarte sections (Fig. 3.3). As degree of welding increases, reflection crests and troughs are produced (0 to ~100 ns); no reflections are apparent in the densely welded zone (below ~100 ns).

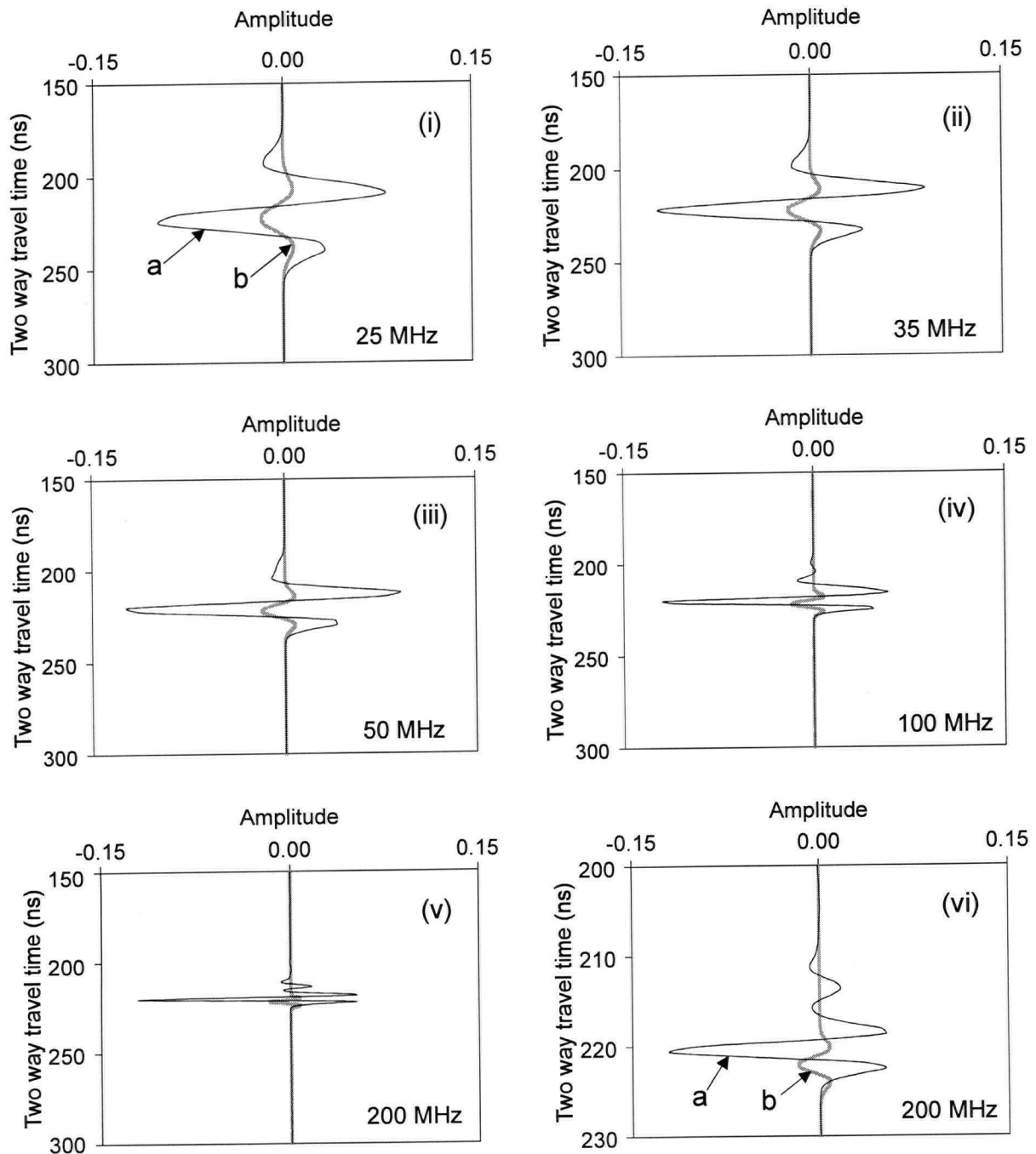


Figure 3.7 Results (150 to 300 ns) of simulations for K' profiles of Fig. 3.3 at a variety of frequencies. In each case, the thin trace corresponds to profile **a** (unwelded base) and the thick trace to profile **b** (densely welded base). The box in panel (v) is stretched vertically in panel (vi) because of the smaller wavelength of the 200 MHz transmitted pulse.

respectively.

Figure 3.6 shows the first 150 ns of the simulations for both profiles at frequencies of 25, 35, 50, 100 and 200 MHz. As degree of welding increases, reflections are produced (0 to ~100 ns); in the densely welded zone no reflections are apparent (below ~100 ns).

Amplitudes decrease with increasing frequency and there are shifts in the position of peak amplitudes. In principle, each EM frequency is capable of delineating the zones of increasing welding and densest welding based on distinctive amplitude patterns. In practice, however, noise will suppress all small amplitude reflections and, in particular, will affect high frequency (lower amplitude) responses. Noise can be related to scattering, instrumental or cultural sources. If noise is truly random then averaging of repeated measurements will improve the signal to noise ratio.

Figure 3.7 shows the synthetic traces for the two Playa de Tasarte profiles from 150 to 300 ns. The results from profile **b** (densely welded at base) are simpler than for profile **a** which shows a rapid change in degree of welding just above the base of the flow (Fig. 3.3). At all frequencies, the synthetic trace for profile **b** consists of a crest, a trough and a crest with the trough centered in the 220-230 ns interval. The crest-trough-crest pattern is the shape of the propagating wave (Fig. 3.3c) and this reflection marks the actual base of the flow.

The trace produced by profile **a** also ends with a crest-trough-crest pattern centered at about 220-230 ns (Fig. 3.7). However, the reflection has a greater amplitude which is a consequence of the larger contrast in K' of the unwelded base of the ignimbrite and the underlying layer of $K'=7$. The rapid, gradational change in K' just above the base of the flow

results in an extra trough immediately preceding the final crest-trough-crest reflection for the 25, 35, and 50 MHz simulations (Fig. 3.7 i, ii, iii). An enlargement of the 200 MHz panel (Fig. 3.7 vi) clearly shows a reflected pulse (trough-crest-trough) before the reflection from the basal contact of the flow. It is possible to see both reflections in the 200 MHz trace because of the small wavelength of the high frequency wave.

3.5 Applicability to field GPR studies

The relevance of these modeling results to the interpretation of real ground penetrating radar (GPR) data is tested below using data from a welded pyroclastic flow (Tumalo Tuff; Hill, 1985) near Tumalo, central Oregon (Fig. 3.8). The data were collected every 0.5 m using a PulseEKKO 100 GPR system with 1000 V transmitter and 50 MHz antennas separated by 2.5 m. Each trace of the radargram is the result of stacking (averaging) 64 traces collected consecutively without moving the apparatus.

The 89.5 m long survey (Fig. 3.8) was run parallel to a vertical wall of a quarry pit operated by the Cascade Pumice Company. This allowed comparison of outcrop observations and radar results. The top of the exposure is an erosional surface and comprises partially welded pyroclastic flow; the rock is solid, shows some alignment of pumice clasts, but lacks eutaxitic texture. The degree of welding decreases with depth and the base is unconsolidated and completely unwelded. At the base of the flow is a 0.5 m ash layer. This is underlain by an airfall deposit (Bend Pumice) identical in mineralogy and chemical composition (rhyodacite) to the pyroclastic flow (Hill, 1985). The water table in the Tumalo area is about 185 m below surface (Sceva, 1968; Caldwell and Truini, 1997) and the

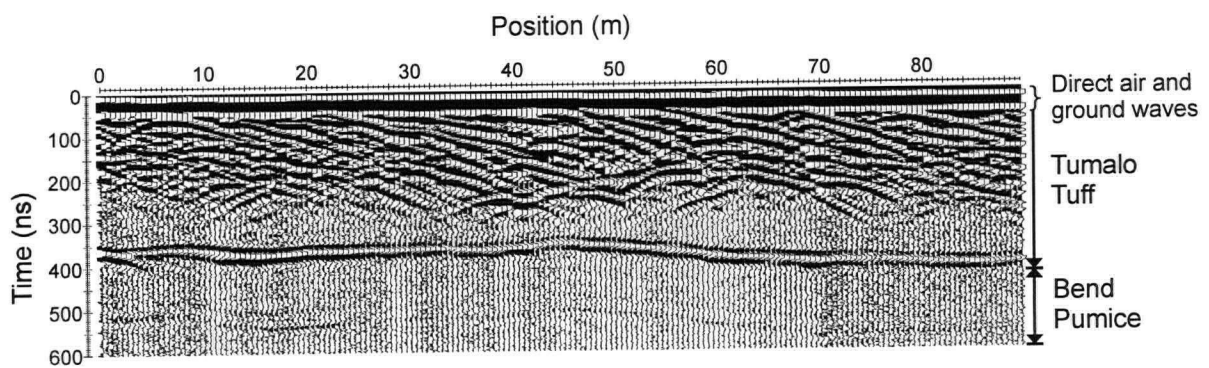


Figure 3.8 Raw GPR data with minimal processing (see text). The Tumalo Tuff and Bend Pumice are co-eruptive welded pyroclastic flow and airfall deposits, respectively. Because velocity varies with depth, the time/depth relationship is not linear. However, the time axis is scaled so that a depth scale would be approximately equal to the lateral position scale (i.e., no vertical exaggeration).

deposits are relatively dry but there is still some moisture in the ground.

My approach is to interpret the corresponding radargram, in part, by comparison to the signal patterns generated for my model sections. Figure 3.8 shows the complete radargram with standard minimal processing: "dewow" to remove low frequency instrumental noise and SEC (spreading and exponential compensation) gain. The strong reflection at about 370 ns represents the base of the pyroclastic flow and the horizontal reflections from 370 down to 500 ns correspond to the underlying stratified, airfall deposit. The pyroclastic flow itself generates abundant reflections in the upper two thirds with very little response from the lower third of the flow. Numerous hyperbolic events (concave down) occur with apices in the middle and upper portions of the deposit. These hyperbolas are caused by diffraction sources of contrasting K' compared to surrounding material. The diffraction hyperbolas are interpreted to originate from relatively large lithic or pumice clasts of unusual porosity compared to the surrounding matrix. These hyperbolas represent sharp, small scale discontinuities caused by clasts in the pyroclastic flow. They can be "removed" by migrating or averaging the section (see Appendix II).

The model simulations presented in this paper (e.g., Fig. 3.5) represent baseline responses caused solely by changes in welding. Figure 3.9 compares a spatially averaged GPR trace derived from Figure 3.8 (average of 31 traces from position 10 to 40m) to a simulation for profile **b** of the Playa de Tasarte ignimbrite. Spatially averaged data were used (see Appendix II) to remove the effects of erratic clasts and steeply dipping reflectors, thus exposing the desired baseline pattern. The simulation and field traces (Fig. 3.9) show similar amplitude patterns, including: i) an upper zone of crests and troughs; ii) a middle zone

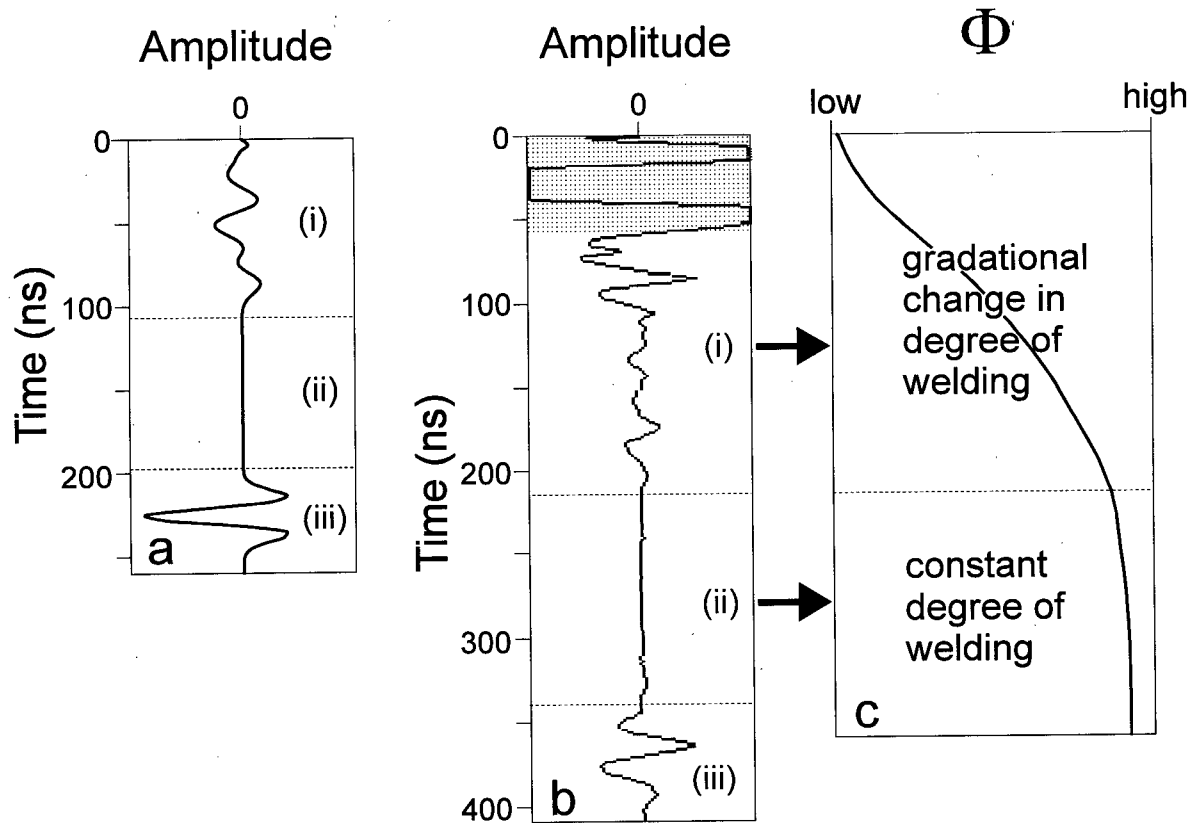


Figure 3.9 Comparison of model and field GPR traces: a) synthetic trace for Playa de Tasarte, profile **b** (welded to base); b) average of 31 GPR traces from positions 10 to 40 m of Fig. 3.8a. The stippled region marks the direct air and ground waves. An SEC gain was applied in b) using an attenuation of 0.5 dB/m. c) Schematic, interpretive porosity profile of pyroclastic flow consistent with GPR trace amplitude patterns of b).

lacking reflections, and iii) a strong reflection at the base of the flow. The similarity in traces, however, is not the consequence of similar porosity profiles: the Playa de Tasarte flow (profile **b**) is densely welded at the base whereas the Oregon flow is unwelded at the base. Rather, the resemblance arises because zone (i) corresponds in both cases to gradational changes in porosity with depth while zone (ii) corresponds to a relatively constant porosity. These data demonstrate how regions of constant porosity and regions of changing porosity with depth can be effectively identified with GPR.

The striking similarity of the model and field traces (Fig. 3.9) despite very different porosity profiles, reveals the ambiguity of the characteristic radar signals recognized in my modeling: "Are zones of near-zero amplitude unwelded or strongly welded regions? Do zones of abundant crests and troughs represent increase or decrease in welding with depth?" These ambiguities can be rectified with analysis of velocity versus depth using in situ velocity estimates from common midpoint GPR surveys or from fitting diffraction hyperbolas. For example, if velocity decreases/increases with depth, portions of traces that show abundant low amplitude crests and troughs can be identified as defining zones of increasing/decreasing degree of welding with depth.

A velocity profile for the data in Figure 3.8, has been derived from a central midpoint survey and shows that velocity increases with depth within the pyroclastic flow. Thus the upper zone, comprising abundant reflections, is interpreted as a zone of decreasing degree of welding with depth while the lower portion lacking reflections, is interpreted as a zone of relatively homogeneous, unwelded pyroclastic material. Figure 3.9c is a possible relative porosity profile deduced from the radargram data. This interpretation, based on GPR data, is

also consistent with the welding pattern seen in outcrop.

3.6 Conclusion

Reflections of radar energy occur in response to spatial variations in electrical properties, which in the case of welded pyroclastic flow units can be related to porosity and degree of welding. These forward modeling results indicate that moderate, gradational changes in welding generate radar responses with low amplitude crests and troughs but no distinct, reflected wavelets. Densely welded areas with little change in porosity produce sections of zero amplitude. A similar signal is generated by zones of unwelded flow of uniform porosity as demonstrated by the Tumalo Tuff GPR data (Fig. 3.8). An extremely high rate of change in porosity with depth can produce a distinct reflection (Fig. 3.7 vi) but if the sharp change occurs very near the base of the flow it can only be resolved by high frequency pulses.

Ground penetrating radar (GPR) can be used to map welding in pyroclastic flows by identifying characteristic signals indicative of zones with strong changes in the degree of welding and zones in which the degree of welding is constant. This is substantiated both by modeling results and, empirically, by case study. Simulations indicate that where porosity increases or decreases at an extremely high rate with depth then a distinct reflection could be used to delimit welded zones. The ability to map zones of welding in volcanic stratigraphy with GPR is particularly useful because young volcanic deposits frequently lack extensive vertical exposure and can show rapid facies changes both vertically and laterally. The characterization of the degree of welding is also of interest for the evaluation of suitability for

nuclear waste disposal.

Chapter 4

Mapping and characterization of pyroclastic flow and fall deposits with GPR

4.1 Introduction

In recent years, ground penetrating radar (GPR) has been used increasingly for imaging the shallow subsurface, however, it has rarely been applied to studies of volcanic deposits (e.g., Lowe, 1985; Russell and Stasiuk, 1997; Russell and Stasiuk 1998). Modern volcanic deposits are ideal candidates for GPR surveys because they possess properties which facilitate the probing of their entire depth; they are commonly electrically resistive and form relatively thin, surficial deposits. Furthermore, GPR can address a number of challenges posed by conventional mapping of volcanic stratigraphy. Firstly, the undissected landscapes associated with many Modern volcanic edifices offer little vertical exposure. Secondly, the stratigraphic correlation of specific units is frequently hindered by complex facies variations or by deposit distributions strongly influenced by paleotopography.

In this chapter, I demonstrate the utility of GPR in the study of pyroclastic deposits. I use two sets of GPR data collected near Bend, central Oregon to illustrate the effectiveness of GPR in delineating and characterizing pyroclastic units and facies with GPR. The two case studies demonstrate strategies to discriminate between deposit types (e.g., airfall versus pyroclastic flow), and facies (e.g., welded versus unwelded pyroclastic flow), and to map deposit geometries.

All data were collected using a PulseEKKO 100 GPR system with 1000 V transmitter

and 50 MHz and 100 MHz antennas. Two types of surveys were conducted: reflection surveys with constant antenna separation and common midpoint (CMP) surveys where antenna separation is increased about a central point.

The first study consists of data collected at a pumice quarry which exposes a welded pyroclastic flow and an airfall of the same rhyodacite eruption. Geophysical survey results are directly compared to vertical outcrops in pit walls for the purpose of correlating distinctive radar signals to the actual pyroclastic deposits. This process of calibrating the radar signal against visible stratigraphy allows the user to determine which units are mappable with GPR. Subsequently, these units may be identified in radargrams generated for locations where there is little or no exposure. Analysis of a series of CMP surveys at the pumice quarry illustrates a more quantitative method of mapping lateral and vertical changes in velocity; these changes in velocity reflect changes in relative porosities due to differential welding. The second field area provides limited vertical exposure of welded to unwelded andesitic pyroclastic flow and unwelded rhyodacite pyroclastic flow deposits exposed in the steep banks of a canal. GPR signals are calibrated against stratigraphic exposures and GPR is then used to delineate deposit geometries away from the exposure.

4.2 Field sites

The locations of the two field sites near Bend, Oregon are shown in Figure 4.1. The Cascade Pumice Company pits, are located 2 km west of the town of Tumalo. The quarried material is pumice from an 0.4 Ma (Hill and Taylor, 1990) rhyodacite airfall deposit called the Bend Pumice. The pumice is overlain by the Tumalo Tuff, a welded pyroclastic flow

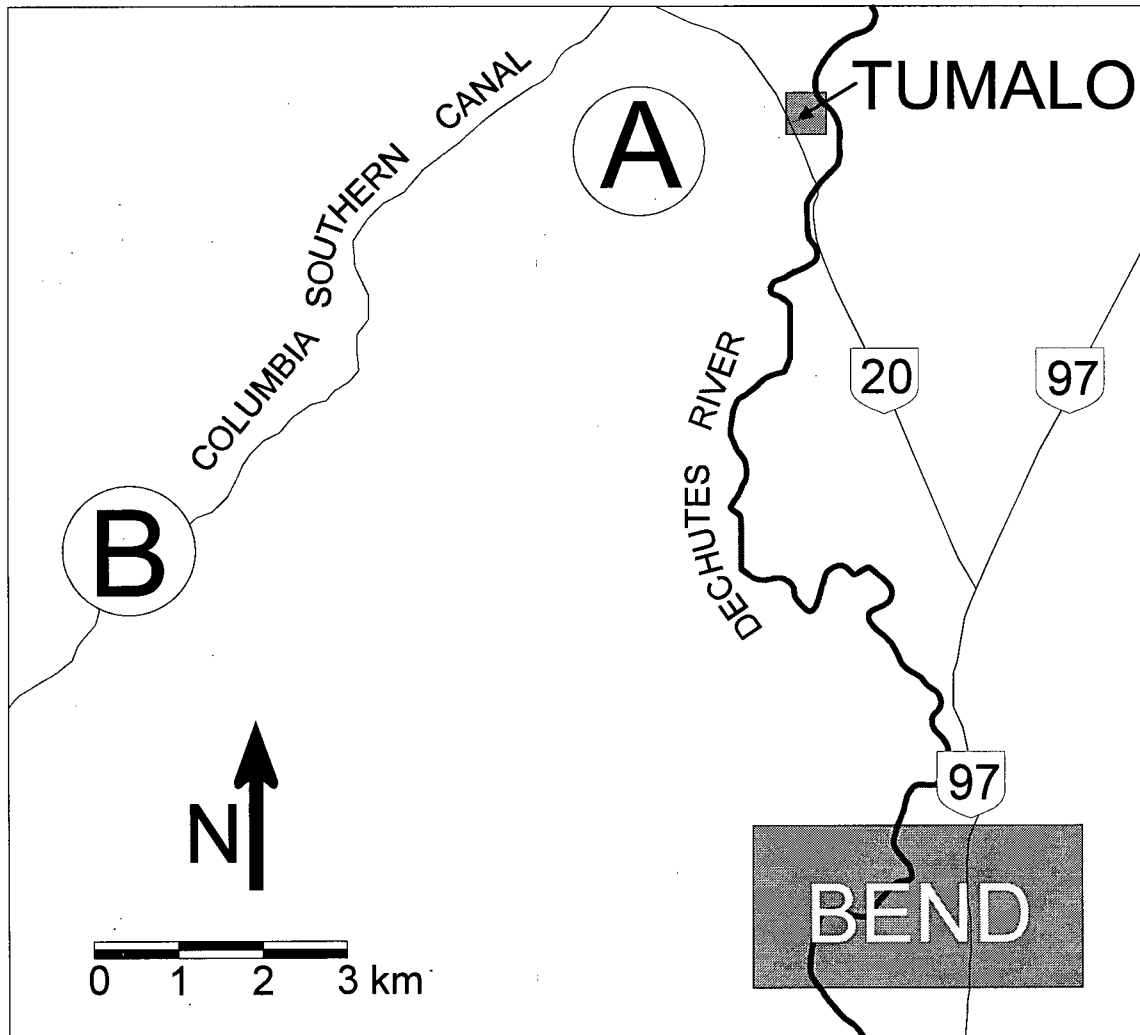


Figure 4.1 Location of two field sites near Bend, Oregon. A) Cascade Pumice Company pits. B) Site along the Columbia Southern Canal.

deposit (Hill, 1985; Hill and Taylor, 1990). It is identical in composition and mineralogy to the Bend Pumice. This flow is welded and varies from unconsolidated and unwelded to solid, welded rock; however, eutaxitic texture has not developed. At the base of the flow is an ash layer, about 0.5 m thick. This ash and the immediately overlying pyroclastic flow are completely unwelded at the quarry. All lines were run parallel to pit walls to facilitate comparison of geophysical data and stratigraphy.

The Southern Canal site, about 10 km northwest of Bend is a wooded area along the Columbia Southern Canal (Fig. 4.1). Where possible, GPR lines follow jeep and horse trails; however, surveys were also run where no trail exists. Two Quaternary pyroclastic flow deposits are exposed in the walls of the canal. The youngest, the Shevlin Park flow, is andesitic (Hill and Taylor, 1990). This deposit is variably welded and ranges from strongly welded with eutaxitic texture to unconsolidated and unwelded. Underlying the Shevlin Park flow is the Tumalo Tuff, the same pyroclastic flow as at the Cascade Pumice pits; however it is completely unwelded at this locality.

4.3 Calibration of characteristic signals in radargrams

The Cascade Pumice Company pits provide excellent vertical exposure which makes it possible to match radar signal patterns with stratigraphy. In this section, I identify characteristic signals for pyroclastic flow (Tumalo Tuff) and fall (Bend Pumice) deposits and for welded facies of the pyroclastic flow deposit. Figure 4.2 shows the survey locations at this site. Collection parameters and processing for all radargrams are listed in Table 4.1.

Table 4.1 Collection parameters and processing for radargrams.

Figure	Field site*	Line #	Frequency (MHz)	Antenna separation (m)	Step size (m)	Stacks	Gain†	processing~
4.3 a	CP	line 1	50	2.5	0.5	64	SEC	-
4.3 b	CP	line 1	100	1.25	0.25	128	SEC	av
4.3 a	CP	line 2	50	2.5	0.5	64	SEC	top
4.5	CP	line 1	50	2.5	0.5	64	SEC	mig
4.6	CP	CMP 1	50	variable	0.5	64	SEC	-
4.11 (left)	CP	line 1	50	2.5	0.5	64	SEC	av
4.11 (right)	CP	line 3	50	2.5	0.5	128	SEC	av
4.15 a	SC	A to G	50	2.5	1	128	AGC	-
4.15 a	SC	J-K	50	2.5	0.5	128	AGC	-
4.16	SC	H-I	100	1.25	0.5	128	SEC	av; top
4.16	SC	J-K; M-N	100	1.25	0.25	128	SEC	av; top
4.16	SC	F-O; O-P	100	1.25	1	128	SEC	av; top
4.17	SC	E-F; P-G	100	1.25	1	128	SEC	av; top
4.17	SC	F-P	100	1.25	0.5	128	SEC	av; top
4.17	SC	H-L	100	1.25	0.25	128	SEC	av; top
4.18	SC	numerous	100	1.5	variable	128	AGC	-
4.2	SC	F-P	100	1.25	0.5	128	SEC	mig

* CP = Cascade Pumice Company; SC = Columbia Southern Canal

† SEC = Spreading & Exponential Compensation; AGC = Automatic Gain Control

~ excluding de-wow and gains; av = 3 point down-trace average; top = topographic correction; mig = migration

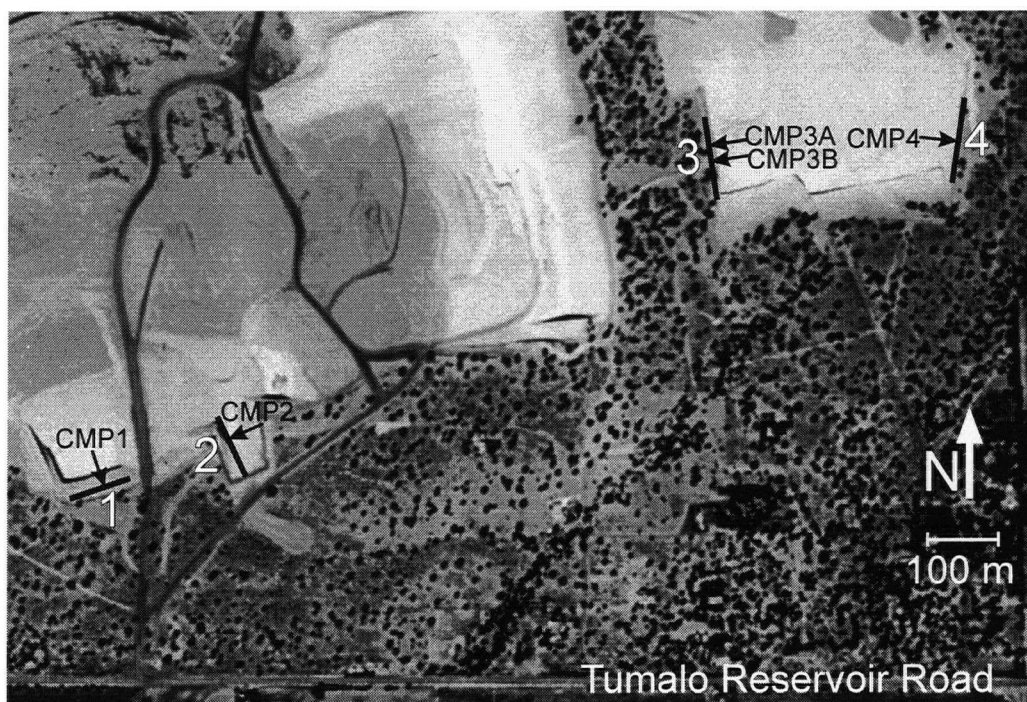


Figure 4.2 Aerial photograph indicating locations of surveys at the Cascade Pumice Company pits. Black arrows mark centers of common midpoint (CMP) surveys.

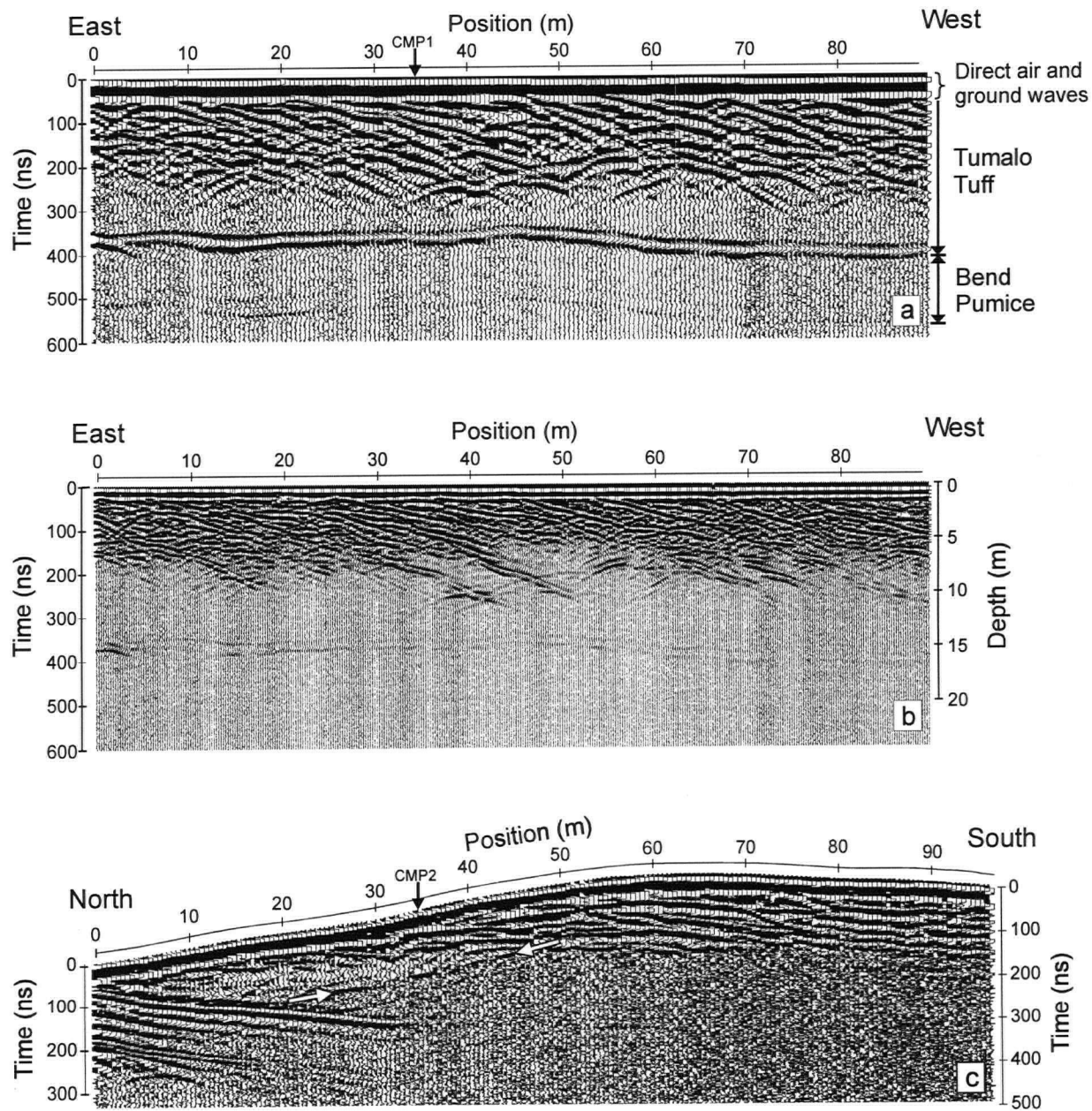


Figure 4.3 Radargrams from the Cascade Pumice pits. See Table 4.1 for collection and processing details. Survey locations are indicated in Fig. 4.2 and field photographs of survey sites in Fig. 4.4. a) 50 MHz, common offset along survey line 1. b) 100 MHz common offset survey along survey line 1. Depth axis corresponds to a constant velocity of 0.08 m/ns. c) 50 MHz, common offset survey up a ramp through pyroclastic deposits (line 2). White arrows mark an above ground reflection off a pit wall. The locations of midpoints of CMP surveys 1 and 2 are indicated in a) and c) respectively. The CMP surveys were run along the survey lines of the common offset surveys.

Figure 4.3 a,b are radargrams from an 89.5 m long GPR survey (line 1, Fig. 4.2), run on horizontal ground (Figure 4.4a). At this location, the erosional top of the Tumalo Tuff is welded and consists of solid rock with some alignment of pumice clasts. The degree of welding decreases with depth and the base is unconsolidated and completely unwelded. The strong reflection at about 370 ns represents the base of the pyroclastic flow and results from reflections off the upper and lower interfaces of a 0.5 m ash layer at the base of the flow. (Figure 4.4b). The pyroclastic flow itself generates abundant reflections and diffraction hyperbolas (concave down) with apices in the upper two thirds with very little response from the lower third of the flow. The horizontal reflections from 370 down to 500 ns in the 50 MHz survey (Fig. 4.3a) correspond to the underlying airfall deposit. The 100 MHz system does not penetrate to a sufficient depth to image below the Tumalo Tuff/Bend Pumice boundary. However, the higher frequency, smaller wavelength radar has greater resolution and therefore allows more closely spaced reflections to be distinguished (Fig. 4.3b).

A comparison of outcrop-scale observations and radargrams leads to the development of characteristic radar signals for elements within the stratigraphic section: 1) The welded pyroclastic flow is characterized by abundant reflections and diffraction hyperbolas. 2) The less welded to unwelded zone shows essentially no response. 3) The base of the pyroclastic flow is marked by a strong, laterally continuous reflection. 4) The pyroclastic fall generates horizontal reflections parallel to its upper and lower boundaries.

Figure 4.3c shows results of another GPR survey at the Cascade Pumice pits, collected along a ramp from the top of the airfall deposit up through the unwelded and then welded Tumalo Tuff (Figure 4.4c). This survey confirms the interpreted pyroclastic

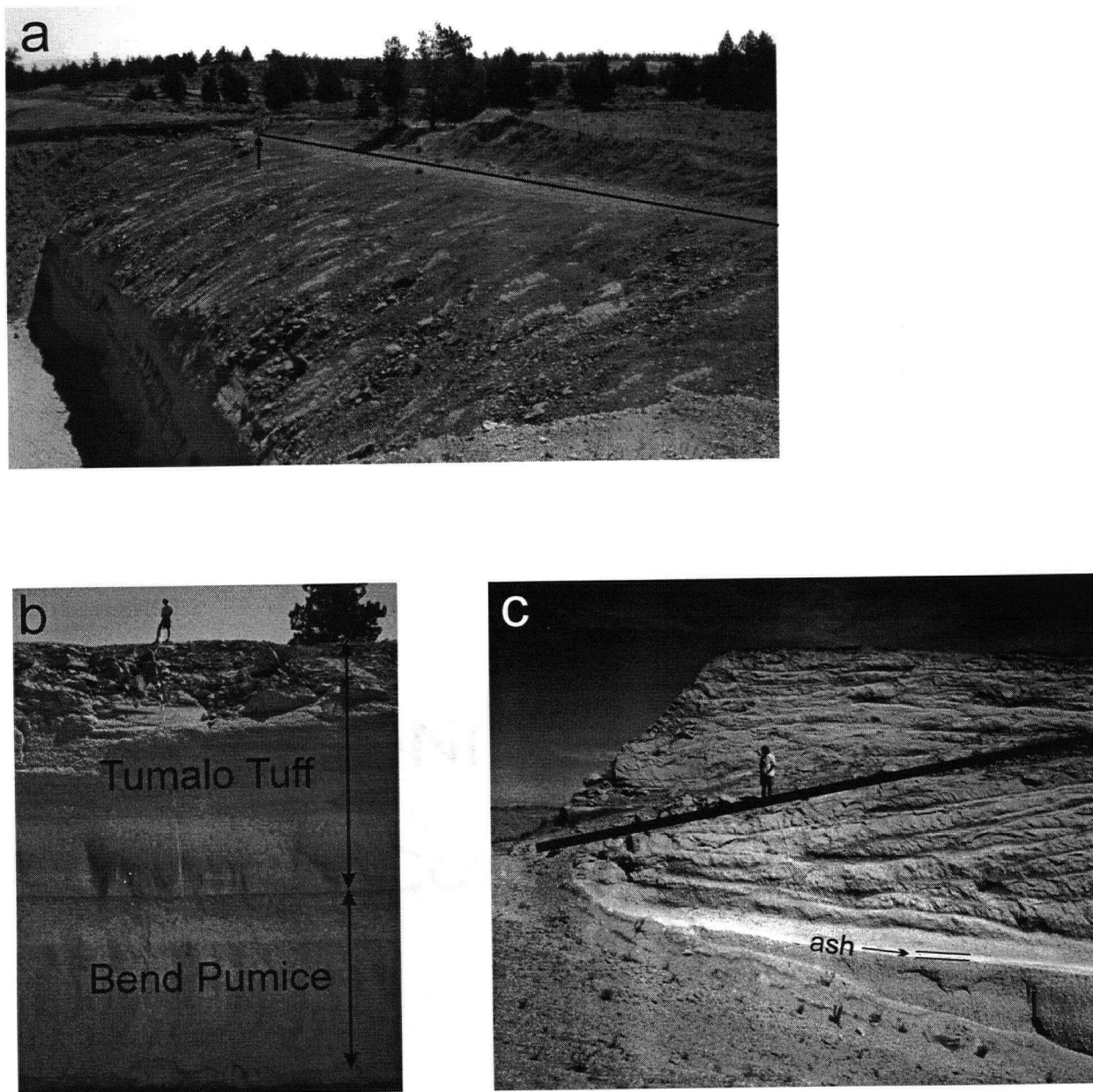


Figure 4.4 Field photographs of GPR lines at Cascade Pumice Company pits. a) Survey line 1 (Fig. 4.2). Vertical arrow marks start of survey. b) Pit wall exposed along line 1. The degree of welding in the Tumalo Tuff decreases with depth. c) Start of survey line 2 (Fig. 4.2) which continues to the right, up the ramp. The Bend Pumice underlies the white ash layer which marks the base of the Tumalo Tuff.

flow/airfall boundary reflection of Figure 4.3a because this reflector begins near surface at the start of line 2. More importantly, this radargram allows examination of signals from the airfall and the lower portion of the flow at very shallow depths where the signal energy is strongest. Near surface, the airfall deposit is marked by abundant reflections parallel to the top and base of the unit and the number of identifiable internal reflections decreases with depth (Fig. 4.3c). Of primary significance is the lack of reflections in the lower, unwelded or poorly welded portion of the pyroclastic flow, even where the deposit is in direct contact with the GPR antennas (positions 7 to 24 m, Fig. 4.3c). This observation confirms that the low amplitude response from the basal portion seen in Fig 4.3a is caused by relatively uniform electrical properties and is not due to energy dissipation from earlier reflections or uncompensated signal attenuation. The ground surface-parallel reflection in this low amplitude zone from 24 to 48 m positions, at about 150 ns two-way travel time in Figure 4.3c is interpreted to be an above ground reflection off a pit wall. This origin was corroborated by common midpoint (CMP) survey velocity analysis (see Velocity analysis, page 75).

Origins of characteristic signals observed

The airfall and pyroclastic flow deposits at the Cascade Pumice site are characterized by different signal textures in radargrams despite nearly identical mineralogy and chemistry (Hill, 1984). This indicates that the Tumalo Tuff, a pyroclastic flow, and the Bend Pumice, an airfall deposit, have distinctive physical properties which affect propagating radar waves. Possible causes for the patterns seen in the radargrams of the Cascade Pumice pits (fig. 4.3) are discussed below.

Pyroclastic flow

Much of the character of the signals in the pyroclastic flow can be attributed to variations in porosity. Using computer simulations of radar waves through welded pyroclastic flow profiles (Chapter 2), I demonstrated that the response generated by gradational changes in porosity depends on the rate of change of porosity with depth. A moderate change in degree of welding generates abundant crests and troughs, a relatively constant porosity results in a flat, zero amplitude response and a discrete jump or extremely high rate of change in degree of welding (abrupt at scale of radar wavelength) can produce a strong, distinct reflection. Based on these results, I interpret the characteristic signals of the pyroclastic flow in Figure 4.3a to indicate a zone with a moderate rate of change in porosity with depth (upper two thirds of flow), overlying a zone with relatively constant porosity (lower third) with a strong reflection caused by a sudden change in electrical properties marking the base of the flow. The degree of welding does in fact decrease with depth in both the upper two thirds and the lower third of the deposit but the rate of change is apparently considerably lower towards the base of the flow.

Another characteristic which separates the upper portion (2/3's) of the radargram from the lower third of the deposit is that the upper portion generates abundant point diffraction hyperbolas. These are notably absent in the lower third of the flow. Considering the lack of eutaxitic texture, I interpret the diffraction sources in the upper portion to be large pumice clasts whose electrical properties contrast with the surrounding, less porous, welded matrix. In the lower, less welded portion of the flow, point diffraction sources are lacking because the matrix and pumice clasts have more similar porosities. However, the clast size and porosity distribution of the rocks have not been studied in detail and the diffraction hyperbola pattern

could be related to the primary concentrations of relatively large pumice or lithic clasts. The hyperbolas are not internal structures of the deposit because migration of the data removes the tails of the hyperbolas (Fig. 4.5). While diffraction hyperbolas are seen in other radargrams at the Cascade Pumice site, the line 1 (Fig 4.2) radargrams (Fig. 4.3a,b) have by far the densest hyperbola population. The simplest explanation is that there is a concentration of larger clasts near survey line 1.

In addition to hyperbolic events, the upper portion of the pyroclastic flow is characterized by numerous, parallel, westward dipping reflectors which are apparent in both the raw and migrated (Fig 4.5) versions of Fig. 4.3a,b. Such dipping reflectors are not seen in the perpendicular survey, collected 200 m to the east (Fig. 4.3b). The origin of this geophysical anisotropy is not clear. No corresponding bedform was evident in outcrop but the slope at survey line 1 (Fig. 2) is not conducive to such observations (Fig 4.4a). These reflectors could be related to emplacement processes, possibly accentuated by welding. Further work exploring this geophysical anisotropy would be worthwhile as it is a potential indicator of flow direction.

Airfall

The strong, continuous reflection marking the Tumalo Tuff/Bend Pumice boundary indicates a sudden change in velocity between the two deposits. Given the common mineralogy of these two deposits (Hill, 1984), this velocity contrast must be related to a change in grain size and sorting. The parallel reflections below the pyroclastic flow/airfall boundary reflection of Figures 4.3 and 4.5 are interpreted to be the result of internal stratification. Stratification is commonly seen in fall deposits and may be produced by

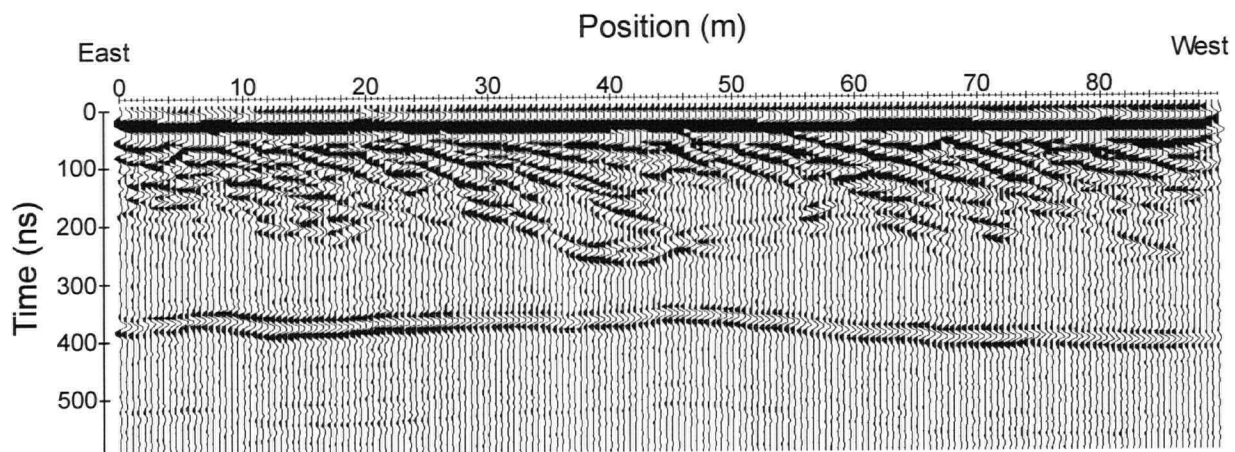


Figure 4.5 Migrated version of 50 MHz, line 1 radargram (Fig. 5.4a). A constant velocity of 0.08 m/ns was assumed.

changes in discharge rates, temporary blocks of the conduit, changes in lithic content, instabilities in the column, compositional zoning, vent widening, or changes in wind direction and speed (e.g., Cas and Wright, 1988). Hill (1984) attributes vertical grain size variations in the Bend Pumice to fluctuations in the diameter of the vent.

General application of characteristic signals

The calibration of radar patterns against stratigraphic exposures is a key concept to extending GPR from areas with outcrop to areas which lack exposure. At the most basic level, it is possible to map deposits and facies by tracing characteristic signals in radargrams, without understanding the physical properties responsible for the radar signals. However, to apply the concept of characteristic radar signals generally, and to be able to deduce physical or volcanological information from distinctive radar patterns, an understanding of the origins of the characteristic signals is required.

The expected radar signal for a pyroclastic fall deposit is either i) a lack of reflections due to high degree of sorting, homogeneous properties and small grain size compared to the radar wavelength (e.g., Russell and Stasiuk, 1998), or ii) reflections parallel to the paleotopography caused by internal stratification (e.g., Fig. 4.3, 4.5). Diffraction hyperbolas formed by large lithics, pumice clasts or charred wood could also be observed, especially proximal to the vent where clasts are larger (e.g., Russell and Stasiuk, 1997).

The signals generated by pyroclastic flow deposits are considerably more complex and variable. At the Cascade Pumice pits alone, diffraction hyperbolas, dipping reflections, flat reflections and areas lacking reflections are all observed. If properties are homogeneous,

as for an unwelded, lithic poor, fine-grained deposit, then no reflections are produced. Bedforms, joints, and moderate to high rates of change of porosity with depth could generate reflections, and large clasts can form hyperbolic diffraction patterns. The correlation between hyperbola abundance and degree of welding seen in Figure 4.3a is not expected to be a universal correlation. For instance, a completely unwelded flow could contain a large number of lithic blocks producing hyperbolic events. Also, if an ignimbrite is extremely densely welded with eutaxitic texture (e.g., vitrophyre) then there would be no contrast in the porosity of the pumice clasts and the matrix. This uniform, low porosity medium would not be a likely source of diffraction hyperbolas.

A single deposit can generate radargrams with a variety of appearances due to the depth of the deposit, properties of overlying material, and variations in cultural noise. This is illustrated by the signal texture produced by the airfall deposit (Bend Pumice) at the Cascade Pumice Company pits. The character of the Bend Pumice varies in the two radargrams presented and is most noticeable in Figure 4.3c. It is implausible that the internal stratification of the pyroclastic fall deposit changes so drastically over such a short distance. In general, the deeper the airfall deposit, the less detailed is the stratification seen in the radargrams. This can be attributed to loss of signal energy from earlier reflections and attenuation, and a reduction in peak frequency with depth. In Figure 4.3c, these effects are aggravated by a cultural noise source. The signal to noise ratio worsens systematically towards the right (south) end of the Figure 4.3c radargram. This is because at the north end of the survey (base of ramp), the GPR receiver is shielded from the noise source by the rock of the ramp and pit walls. At the top of the ramp (positions $>63\text{m}$, Fig 4.3c), there is nothing

to the shield the receiver.

4.4 Velocity analysis

Common midpoint (CMP) surveys provide data on subsurface radar velocity which are essential for converting two-way travel times into reflector depths. A further application of velocity analysis is determining spatial variations in dielectric constant which can be converted to physical properties. Therefore, there is the potential to use vertical and lateral changes in velocity derived from CMP surveys to infer spatial variations in relative degree of welding.

CMP surveys and velocity calculations

A CMP survey involves the progressive increase in separation of the transmitter and receiver from a central point. Arrows in Figure 4.2 mark the CMP survey locations at the Cascade Pumice Company pits. The midpoints for two of these CMP surveys are also marked on the radargrams of Figure 4.3. Figure 4.6 gives an example of a CMP survey collected. The results of velocity analysis on the five CMP surveys are found in Figures 4.7 to 4.9.

Each reflector corresponds to a hyperbola on the CMP profile, the shape of which depends on the velocity of the radar wave through the material above the reflector. Hyperbolas are converted to (V_{rms} , time) data points (Fig. 4.7). The V_{rms} is neither the instantaneous nor the average velocity but rather is the root mean squared velocity, defined by:

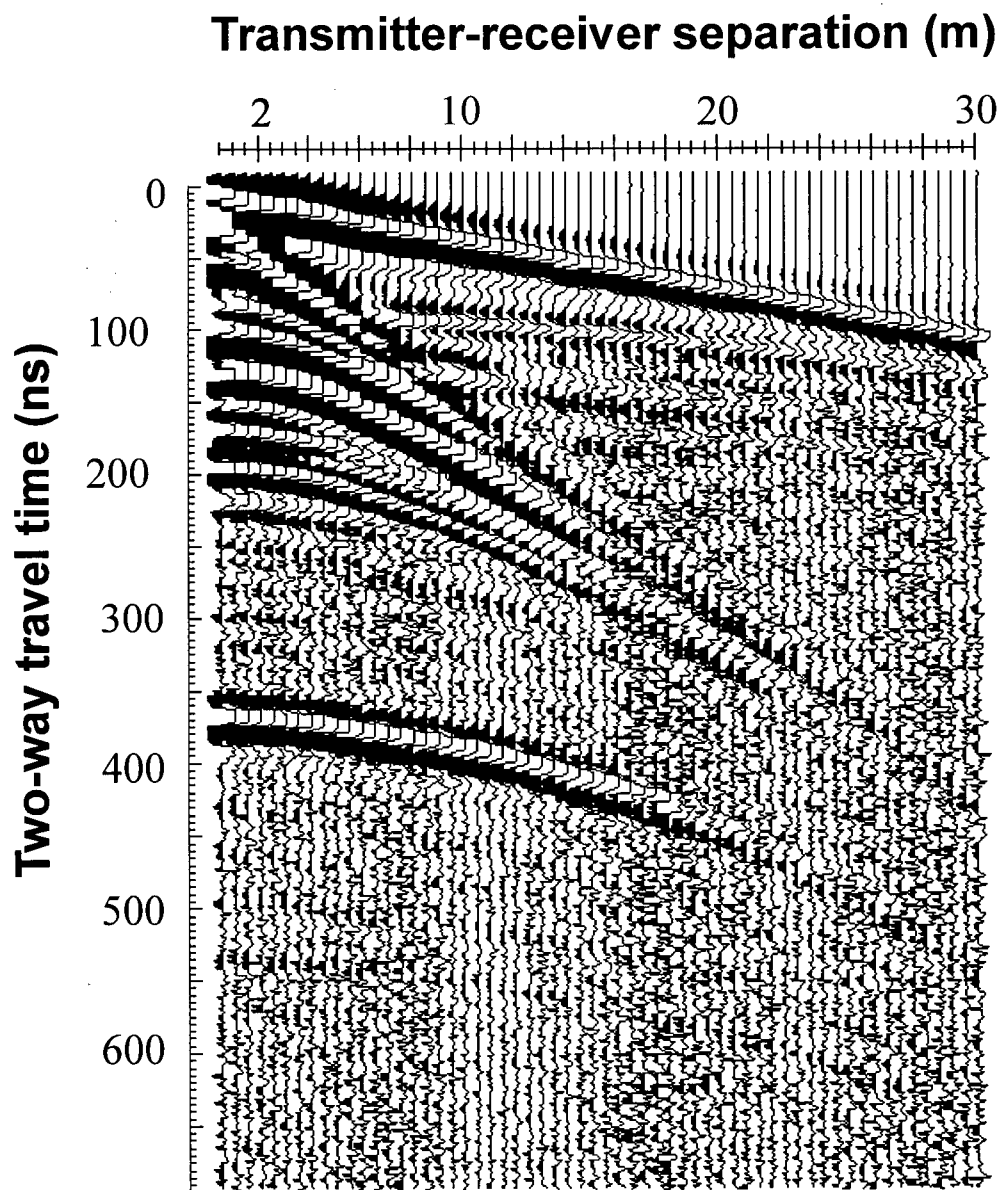


Figure 4.6 50 MHz common midpoint survey CMP1 (Fig 4.2). See Table 4.1 for details.

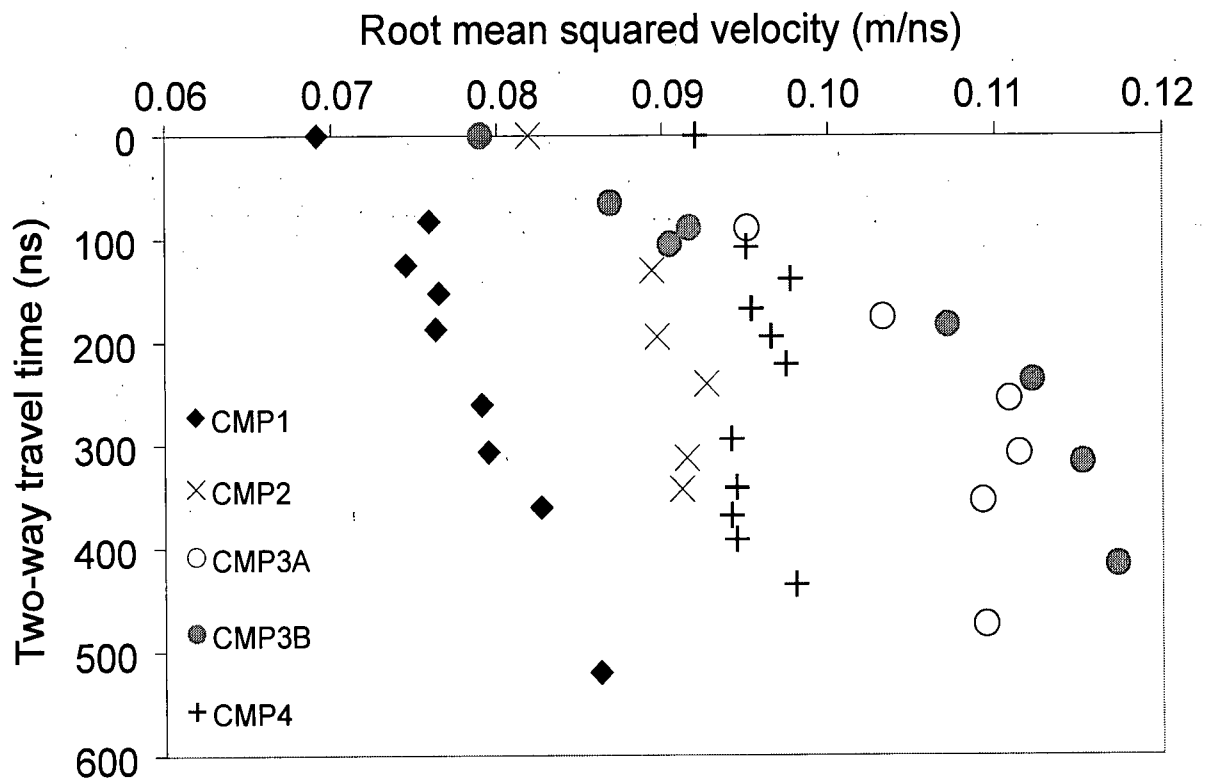


Figure 4.7 Results of five CMP surveys plotted as root mean squared velocity vs. time. Velocities at time=0 represent velocities along ground surface between the antennas and do not involve reflection. Other data derive from fitting hyperbolas to reflections in CMP radargrams (e.g., Fig. 4.6).

$$V_{\text{rms}}^2 = \frac{\int_0^{t_0} V^2(t_0) dt_0}{t_0} \quad (4.1)$$

Examining the results for all five CMP surveys (Fig 4.7, 4.8), two general patterns are evident: 1) within the Tumalo Tuff, V_{rms} increases with depth; 2) within the Bend Pumice, V_{rms} is relatively constant. Based on these observations, for each CMP survey, I fit the V_{rms} -time data for the two deposits separately. The Tumalo Tuff data are fit by least squared residuals (in velocity) with 1st or 2nd order polynomials, whereas, the Bend Pumice data are fit with lines of constant velocity (Fig. 4.8). Velocities are re-sampled along polynomial fits, keeping the original two-way travel times (Fig. 4.8). Each re-sampled velocity is within 5% of the original V_{rms} data.

I expect the overall velocity pattern to be gradational due to gradational changes in porosity associated with welding. However, I model the system with a stack of homogeneous (constant velocity) layers; one between each pair of reflections fitted. The re-sampled V_{rms} data are converted into interval velocities (V_{int}) using Dix's equation (Dix, 1955):

$$V_{\text{int}}^2 = \frac{\overline{V}_2^2(t_2) - \overline{V}_1^2(t_1)}{t_2 - t_1} \quad (4.2)$$

where V_{int} is the velocity through a particular layer and \overline{V}_1 and \overline{V}_2 denote rms velocities for the regions between the ground surface and the top and the base of the layer respectively (Fig. 4.8). Figure 4.9 plots interval velocities against height above the Tumalo Tuff/Bend Pumice boundary. Interval thicknesses are calculated from V_{int} and travel time data.

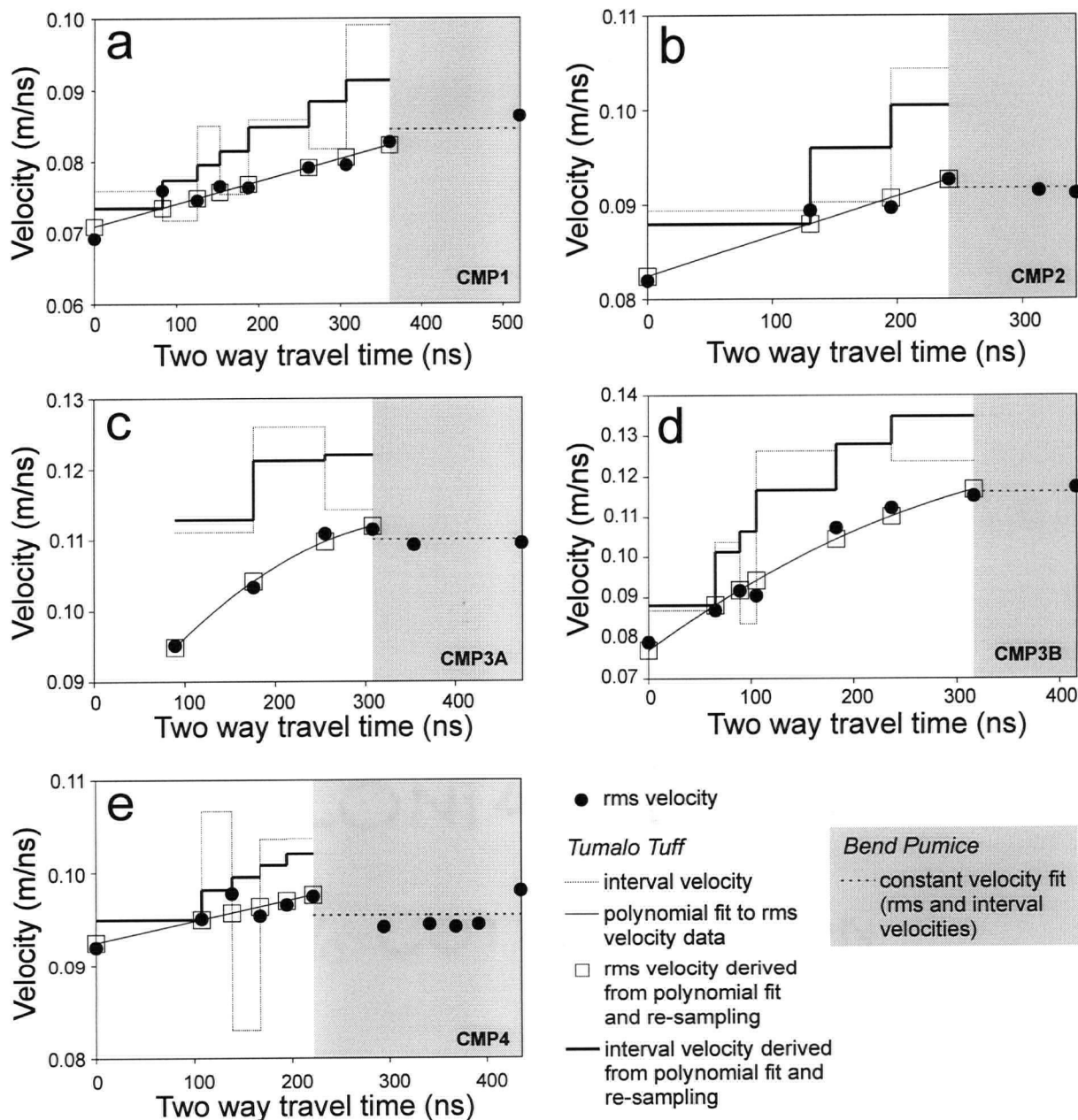


Figure 4.8 Plots showing velocity analysis results for five CMP surveys. Dark circles are same data as presented in Fig. 4.7. In each plot, the Tumalo Tuff data are fit to the 1st or 2nd order polynomial curves. V_{rms} data are re-sampled along the polynomial curve, keeping the same two-way travel times. Interval velocities are calculated for both the original V_{rms} (circles) and re-sampled (squares) data. The results of the latter are considerably less erratic. Velocities in the Bend Pumice are averaged to give a constant V_{rms} and V_{int} .

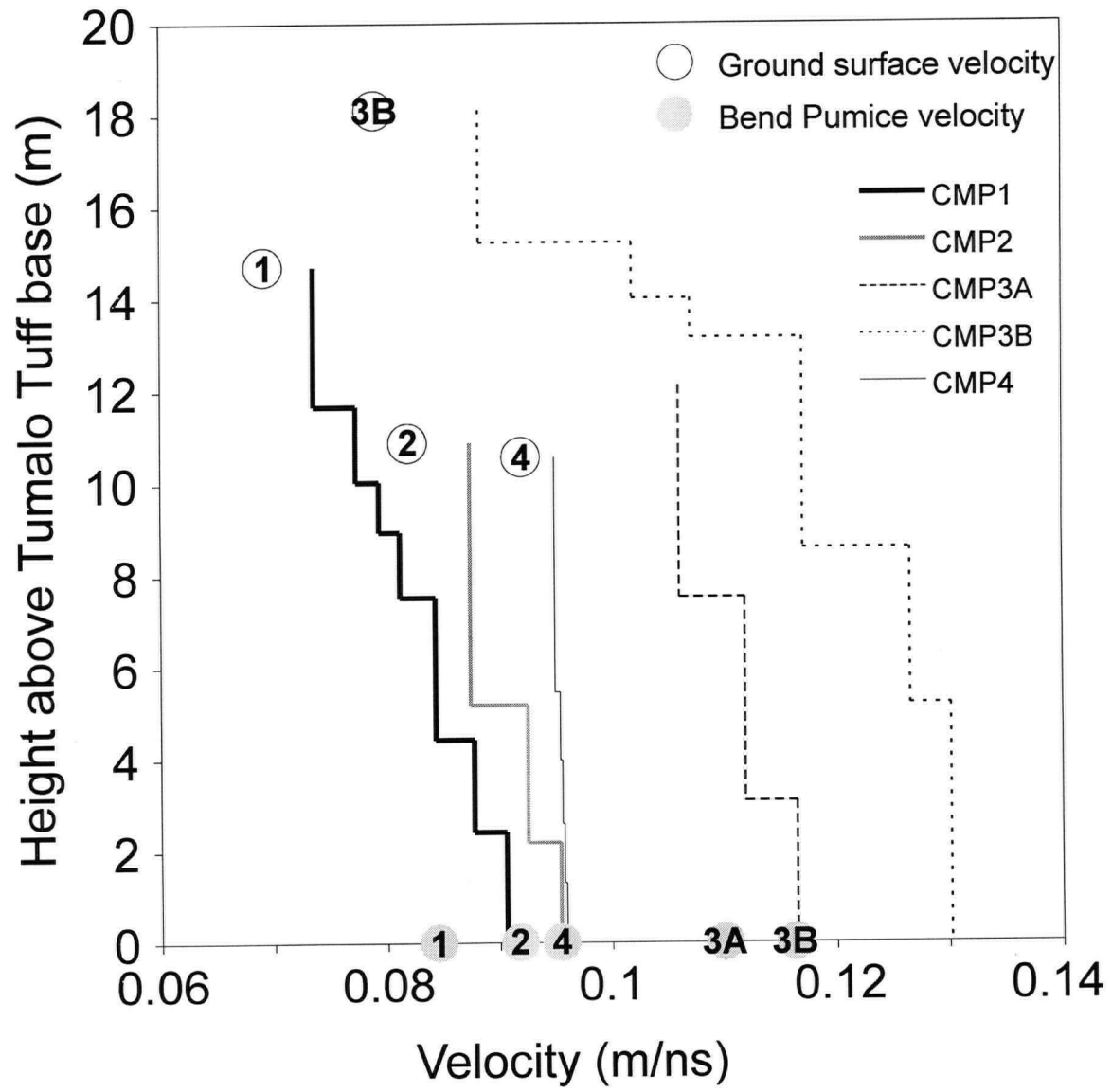


Figure 4.9 Plot of velocity versus height above Tumalo Tuff/Bend Pumice boundary. Lines are interval velocity data derived from polynomial fit and re-sampling (Fig. 4.8). Open circles mark velocities of direct ground waves at surface of surveys. Grey circles indicate Bend Pumice velocities from Fig. 4.8.

Interpretation of velocity patterns

I attribute decreases in velocity to decreases in porosity due to welding, and therefore use relative velocity patterns to determine relative changes in degree of welding. The increase in velocity with depth through the Tumalo Tuff (Fig. 4.7-4.9) is interpreted as a decrease in degree of welding with depth as observed in pit walls. The relatively constant velocity through the unwelded Bend Pumice suggests fairly constant porosity with depth.

The velocity analyses of all five CMP surveys indicate a lower velocity in the Bend Pumice than in the unwelded base of the overlying pyroclastic flow. If the assumption that velocity changes are primarily related to porosity differences is true, the relative velocities imply that the pyroclastic fall deposit has a lower porosity than the base of the pyroclastic flow deposit. This is an unexpected result because fall deposits are generally better sorted than flow deposits. However, the lower velocity in the Bend Pumice is confirmed by the polarity of the reflection associated with the Tumalo Tuff/Bend Pumice boundary. In Figure 4.3a, the direct air wave is positive-negative-positive (white-black-white), whereas, the reflection at about 360 ns is negative-positive-negative. This polarity reversal indicates a lower velocity below the reflection surface (e.g., Reynolds, 1997).

A comparison of the four velocity profiles suggests a decrease in degree of welding laterally from survey 1 to 2 to 4. This is in fact confirmed by outcrop observations. Site 4 shows the least degree of welding and CMP analysis reveals a relatively constant velocity profile. The analyses of CMP surveys 3A and 3B show substantially higher velocities than the other three surveys. This suggests much higher porosities than for other survey locations but this is not corroborated by field observations.

Variations in velocity of the Bend Pumice provide clues to the origins of lateral velocity variation in the Tumalo Tuff. The Bend Pumice is a pyroclastic fall deposit and the bulk physical properties of the unit are not expected to significantly vary laterally on the scale of this set of surveys. However, the average velocity in the Bend Pumice varies from 0.084 to 0.116 m/ns (Fig 4.10). Considering the deposition process of pyroclastic falls, the cause of this velocity diversity is likely post-depositional. One possible contributor is differences in the original thickness of Tumalo Tuff overlying the fall deposit. Increased thickness would cause greater compaction and lower porosities. The thickness of pyroclastic flows can be severely effected by changes in paleotopography, however, the Tumalo Tuff/Bend Pumice boundary is relatively flat. Therefore, it is unlikely that there were dramatic differences in the original thickness of the Tumalo Tuff at surveys 1, 2 and 4 compared to surveys 3A and 3B which lie between surveys 2 and 4 (Fig. 4.2). A second, more plausible origin for the lateral variation in Bend Pumice velocity is a difference in degree of water saturation between survey lines. Water has a much higher K' than air or volcanic rock. Thus small changes in water concentration and geometry of the water phase can have a large effect on velocity (Appendix 3). Water content variation may be natural but in this case some of the variation between surveys could be caused by evaporation off pit walls. The wall surfaces are completely dry and the proximity of surveys to walls and the azimuth of the walls could affect water content.

There is a direct relationship between the velocity in the Bend Pumice and the velocity in the lowermost interval velocity of the Tumalo Tuff (Fig. 4.10). Given that a perfectly dry airfall deposit would be expected to have a constant lateral velocity, I conclude

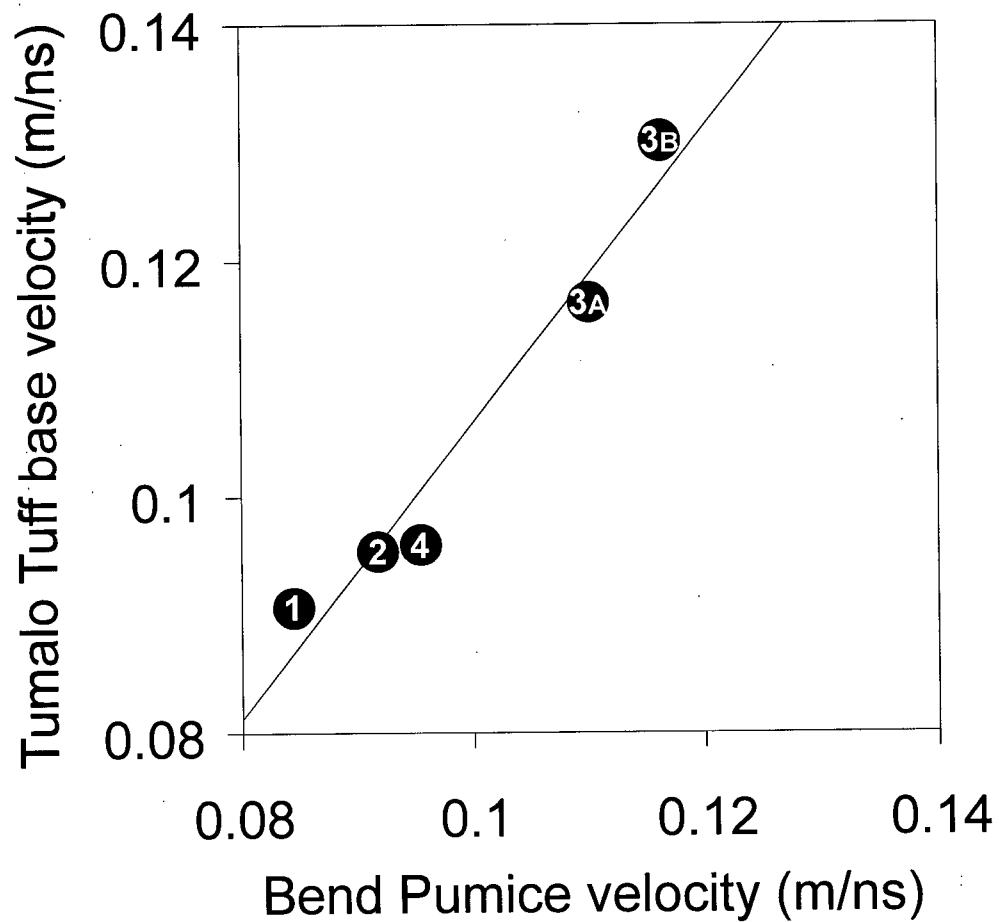


Figure 4.10 Plot of velocity in lowermost interval velocity for Tumalo Tuff (V_{TT}) vs. Bend Pumice velocity (V_{BP}) (Fig. 4.8, 4.9). Line of best fit is $V_{TT} = 1.253V_{BP} - 0.019$.

from the correlation seen in Fig 4.10, that water equally affects the velocities of the Bend Pumice and the base of the Tumalo Tuff. Therefore a direct comparison of interval velocities from survey to survey will not necessarily give accurate lateral porosity variation. There is the possibility, however, of normalizing the Tumalo Tuff data using the Bend Pumice velocities. Further research on the effect of water on velocities is required to normalize effectively.

Depth conversion

A common application of CMP survey results is converting reflection times to depths. The lateral velocity variation at the Cascade Pumice pits means that a single travel time-depth conversion will not be applicable to all radargrams at the site. For example, the travel time to the Tumalo Tuff/Bend Pumice boundary in CMP4 is less than for CMP1 although the boundary is further below the ground surface in CMP4 than CMP1. Figure 4.11 compares surveys and depth scales of lines 1 and 4 determined from V_{int} data.

Using interval velocity and travel time data, total thicknesses of the Tumalo Tuff are calculated (Fig. 4.9). Figure 4.12 compares the calculated depths to the Tumalo Tuff boundary to those measured on outcrops with a tape measure. The results show the CMP-derived depths are accurate to within approximately 15%. Figure 4.11 also indicates that the CMP velocity analysis and conversion into interval velocities give reasonable results and that the significantly greater velocities calculated for survey line 3 are real.

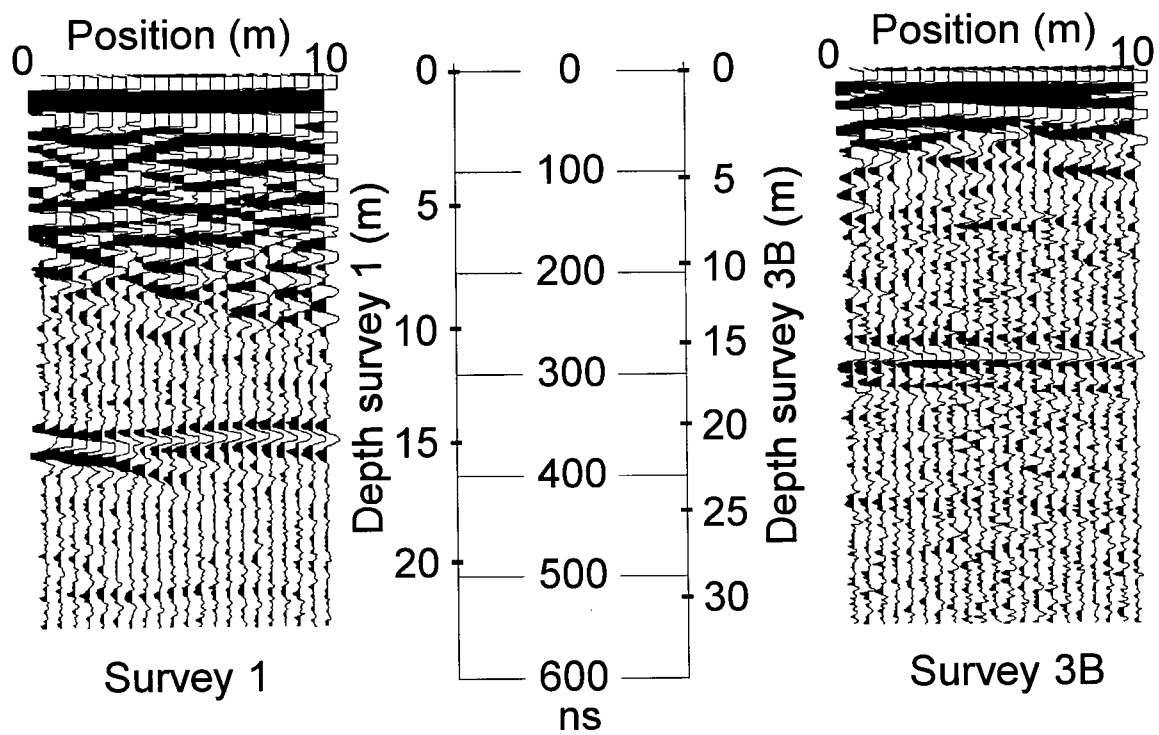


Figure 4.11 The first 10 m of surveys 1 and 3 (Fig. 4.2) are displayed with common two-way travel time (center column). The depths scales for each survey derive from CMP analyses (Fig. 4.8, 4.9).

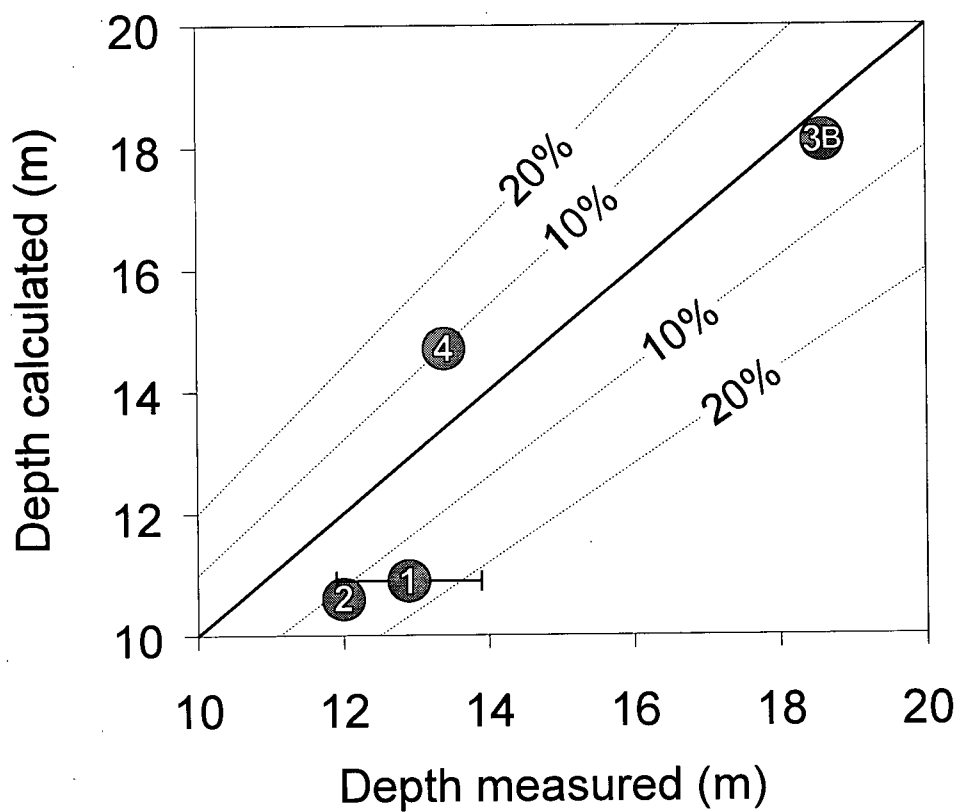


Figure 4.12 Comparison of depth to Tumalo Tuff/Bend Pumice boundary calculated from CMP velocity analysis (Fig. 4.9) and depth measured with a tape measure. Dashed lines envelope areas where calculated depths are within 10% and 20% of measured depths.

4.5 Columbia Southern Canal: mapping deposit geometries

At the Columbia Southern Canal, we move away from the control of a quarry site. I used steep stream bank exposures (Fig. 4.13) to calibrate the radargrams with volcanic stratigraphy. I include data from this site primarily to demonstrate the use of GPR in mapping deposit geometries away from exposures. In addition, I apply ideas developed in the Cascade Pumice case study to elucidate information of volcanological interest from the radargrams.

Figure 4.14 indicates the positions of the surveys in map view. Initial surveys employed 50 MHz antennas with a relatively large step size (1 m) to cover the area quickly. These radargrams are presented without topographic correction in Figure 4.15. Using these data, I chose a portion of the area covered by 50 MHz surveys, to examine in further detail with 100 MHz antennas. The 100 MHz radargrams are presented in Figures 4.16 and 4.17 with topographic correction assuming a constant velocity of 0.1 m/ns based on CMP survey analyses. To aid the visualization of deposit geometries four views with the sections fenced together are also included (Fig 4.18).

Deposit boundaries

The reflection corresponding to the Shevlin Park/Tumalo interface is identified by comparison of radargrams to field exposures. At point **O** (Fig. 4.16), the contact is 8.7 m below the GPR survey and at point **L** (Fig. 4.17), the top of the Tumalo Tuff is at a depth of 10.5 m with 0.6 m of reworked material, including vesicular basalt cobbles, at the base of the Shevlin Park flow. Using these two calibration points, the contact is traced to other



Figure 4.13 View of Columbia Southern Canal site, looking upstream. Most exposed rock is the Shevlin Park flow. Outcrops of the Tumulal Tuff (TT) are visible in foreground. The Black line marks survey **H-L** (Fig. 4.14).

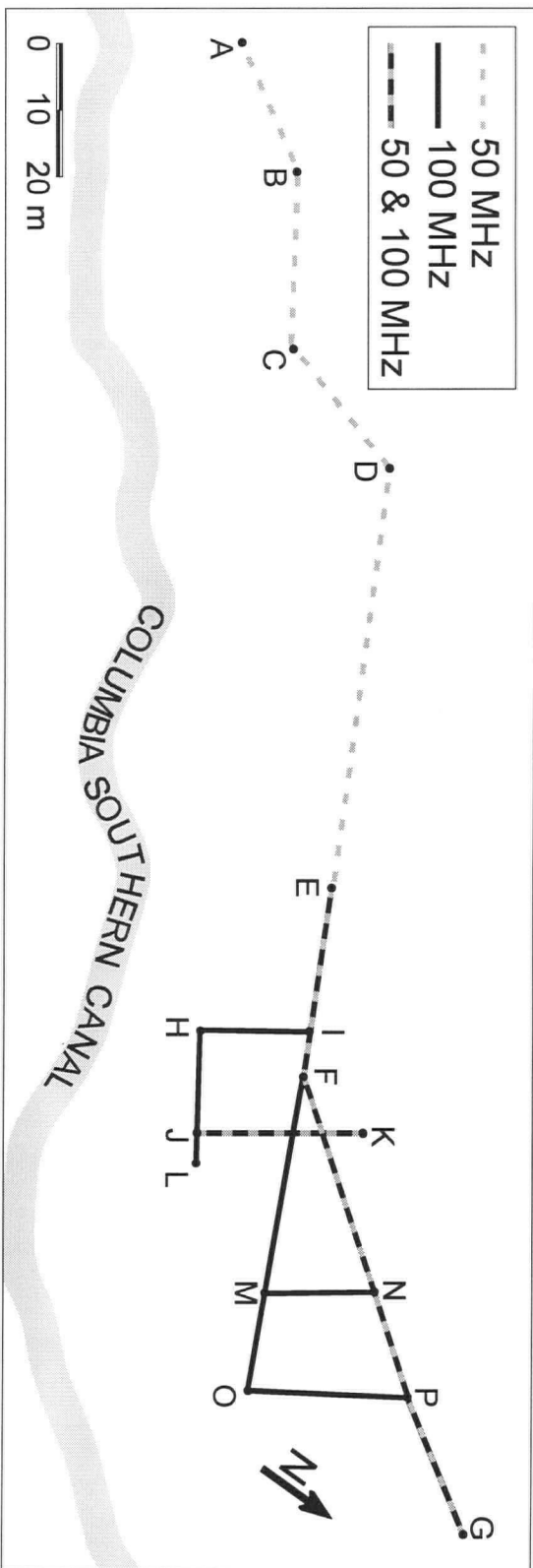


Figure 4.14 Location of GPR surveys at the Columbia Southern Canal site.

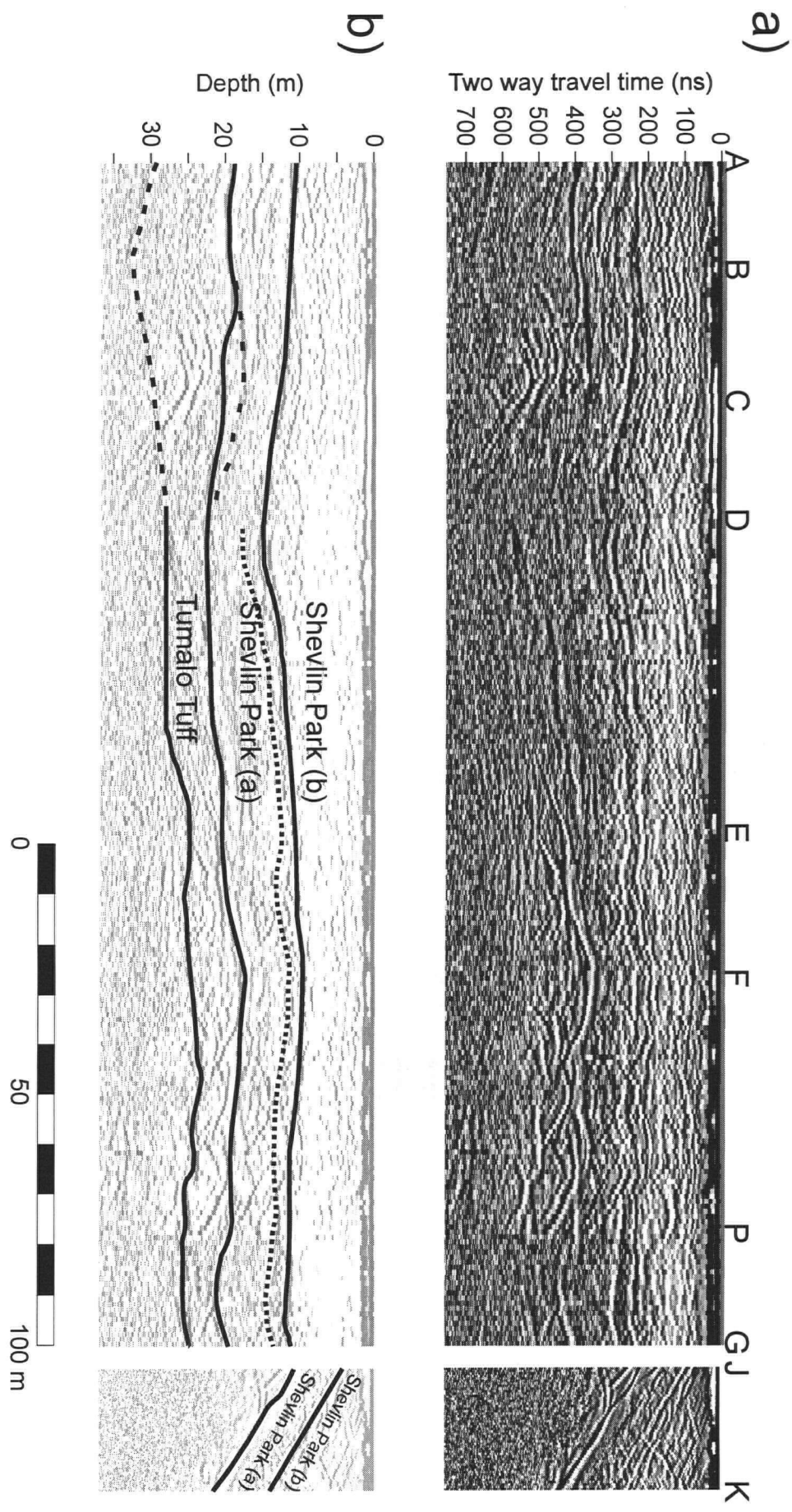


Figure 4.15 50 MHz surveys at the Columbia Southern Canal displayed without topographic correction. See Table 4.1 for details. a) Data with de-wow and AGC gain. b) Interpreted stratigraphy draped on subdued radargrams.

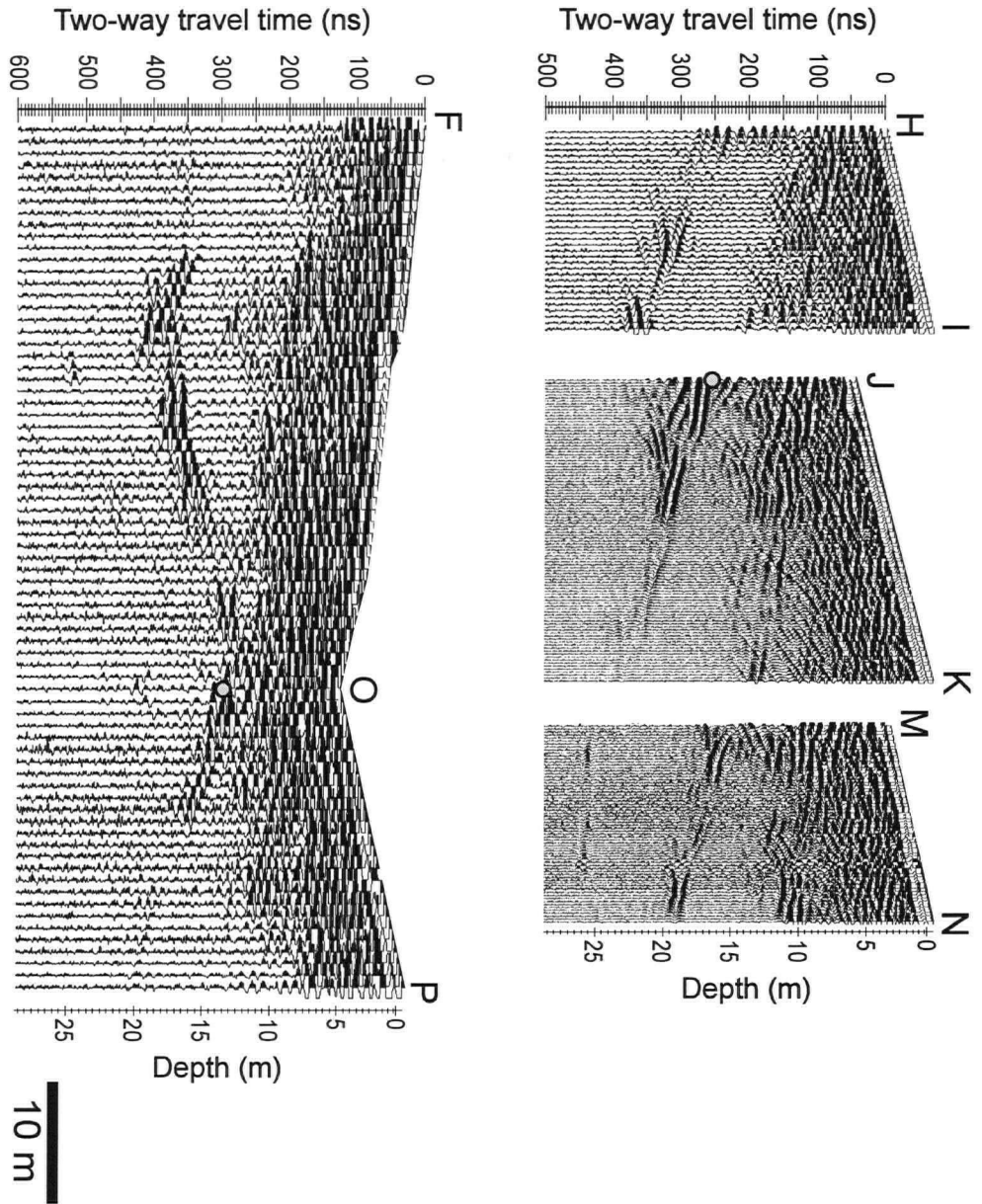


Figure 4.16 100 MHz radargrams at Columbia Southern Canal trending approximately north-west (except survey F-O). Grey dots below points J and O are calibrations of Shevlin Park/Tumalo Tuff boundary as determined on nearby outcrop (See text for details). Topographic corrections and depth scales based on constant velocity of 0.1 m/ns.

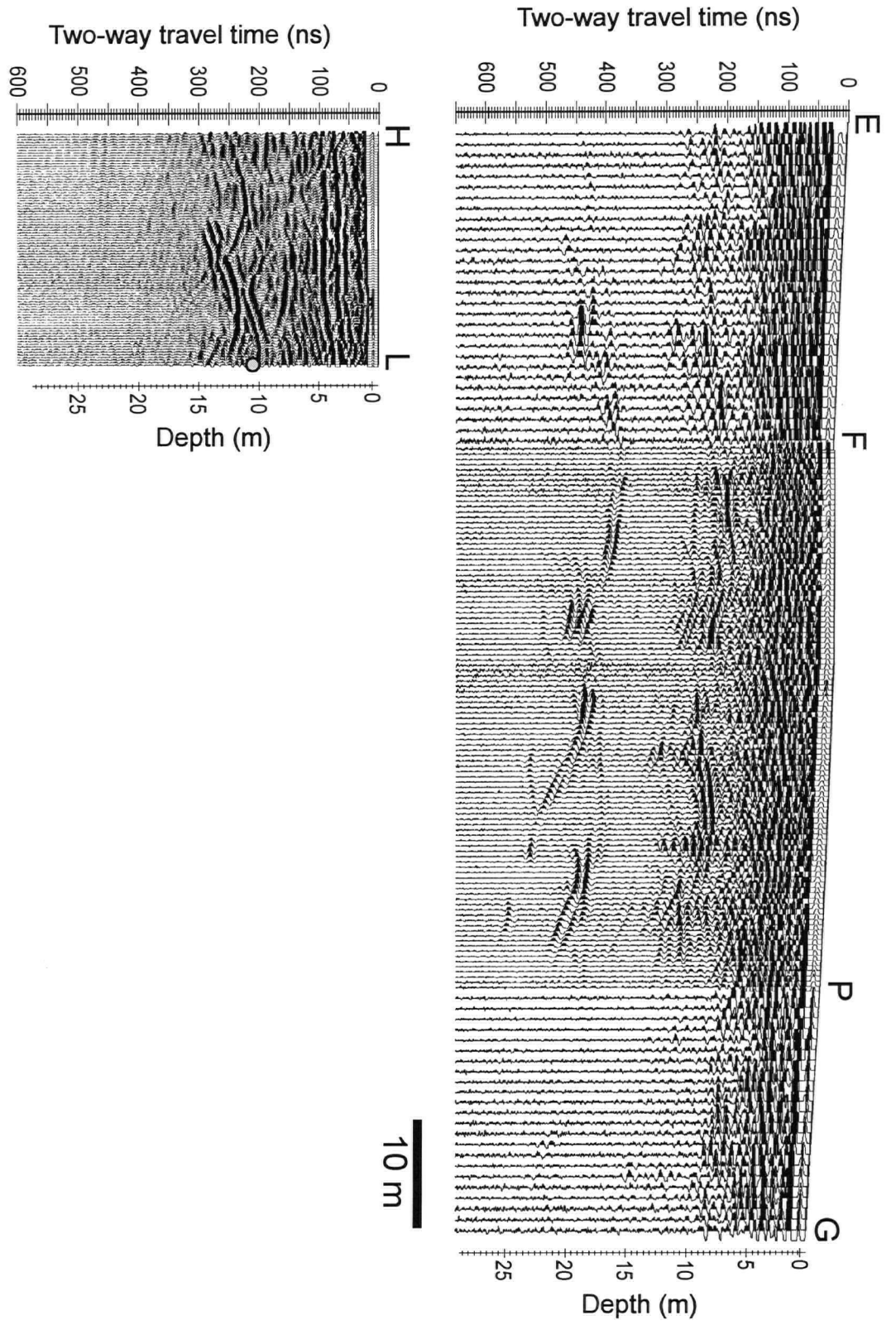


Figure 4.17 100 MHz radargrams at Columbia Southern Canal trending approximately north-east. Grey dot below point L indicates Shevlin Park/Tumalo Tuff boundary as determined on nearby outcrop (See text for details). Topographic corrections and depth scales based on constant velocity of 0.1 m/ns.

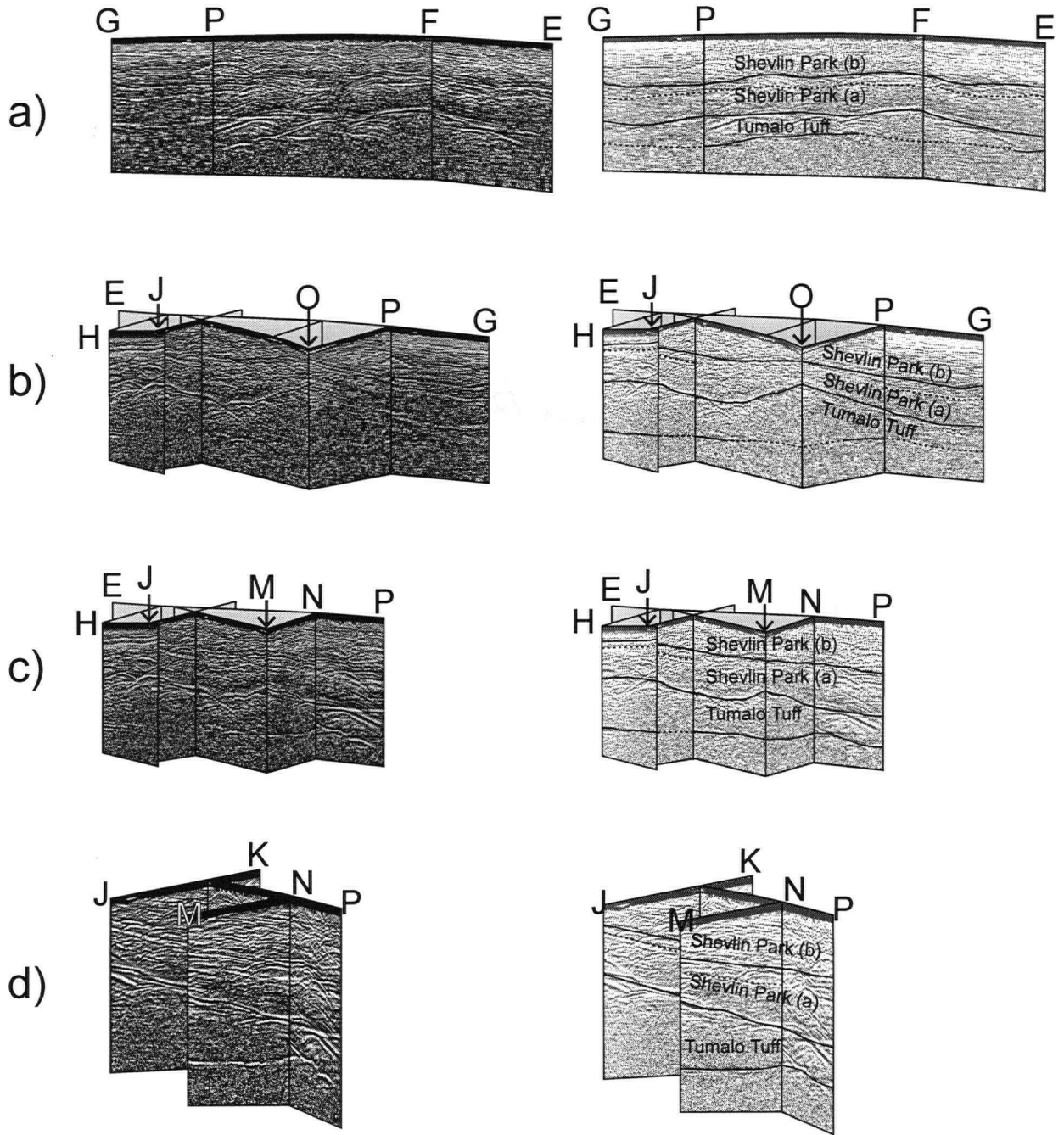


Figure 4.18 Four views of 100 MHz radargrams fenced together. Raw data (AGC gain) on left; interpreted stratigraphy on right. See Fig. 4.14 for orientations of surveys and Figs. 4.16 and 4.17 for dimensions.

radargrams. In northwest trending surveys (radargrams **H-I**, **J-K**, **N-M**, and **O-P**, Fig. 4.16), the base of the andesitic flow (Shevlin Park) dips at about 15° NW; whereas, in most surveys trending approximately northeast, (radargrams **E-F**, **H-I**, **F-P**, **P-G**, Fig. 4.17), the base of the flow is practically horizontal. This geometry likely delimits the edge of a channeled flow, the result of paleotopography and scouring of the loose Tumalo Tuff during emplacement of the Shevlin Park flow. The Shevlin Park/ Tumalo Tuff boundary is frequently characterized by apices of hyperbolic events (eg., surveys **H-L**, **H-P**, Fig 4.17) which are likely generated by a concentration of non-juvenile clasts at the base of the younger, Shevlin Park flow.

The base of the Tumalo Tuff is not exposed in outcrops along these GPR surveys. On the other side of the canal, across from survey point **C** (Fig. 4.14), the Bend Pumice appears to underlie the Tumalo Tuff (Fig. 4.19 a); however, I was not able to get close enough to positively identify the deposit. The 13 m long, strong, continuous reflection at 450-500 ns in radargram **M-N** (Fig. 4.16, 4.18) probably marks the base of the flow. This reflector is also recognized in surveys **H-L** and **F-P** (Figs. 4.17, 4.18), and to a lesser extent surveys **F-O**, and **O-P** (Fig. 4.18). The reflector is not pervasive because its depth is close to the limits of penetration of the system. In all sections, regardless of the apparent dip of the basal contact of the Shevlin Park flow, the base of the Tumalo Tuff is horizontal or slightly dipping to the north-east.

Internal structures of pyroclastic flows

There is a definite and continuous reflection within the Shevlin Park flow that approximately parallels the flow base with some thickening of the lower portion as the

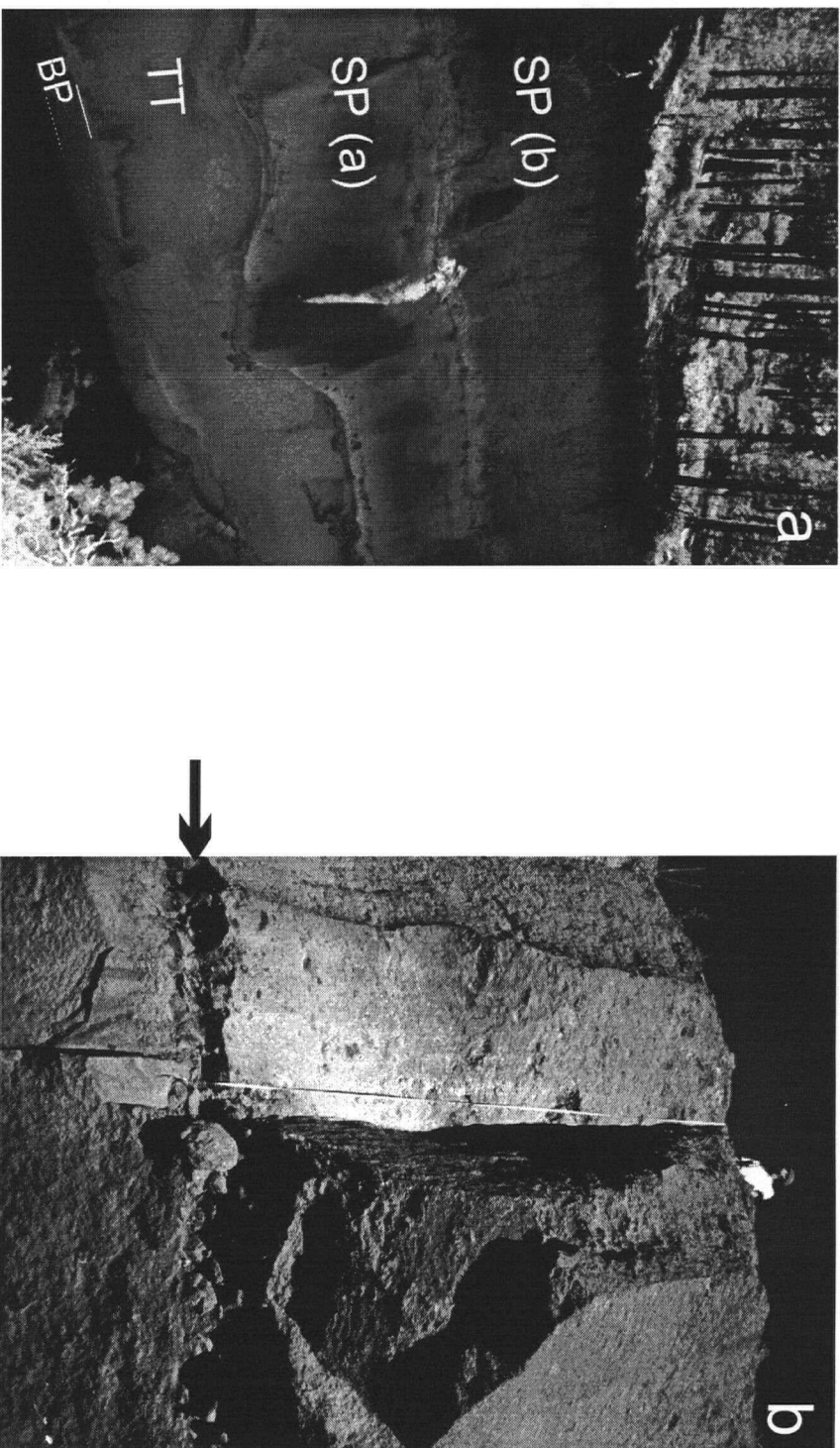


Figure 4.19 Photographs from Colombia Southern Canal site. a) Exposure on south-east side of canal across from survey point C (Fig. 4.14). All deposits show little or no welding on this exposure. SP a,b = Shevlin Park flow phases; TT = Tumalo Tuff; BP = possible exposure of Bend Pumice. b) Layer of cobbles in strongly welded Shevlin Park flow marking the boundary of the phases of the flow.

channel deepens. This horizon is interpreted to be the boundary between two phases of the andesitic pyroclastic flow. In the upstream (southwest) portion of the 50 MHz survey, near point **B** (Fig. 4.14) this reflection coincides with a cobbly layer in a densely welded portion of the andesitic flow (Fig 4.19 b). The two phases were emplaced in relatively close succession because they form a single cooling unit. The presence of two phases is also evident is the unwelded/poorly welded flow seen in Figure 4.19 a. The contact between the phases is not always so apparent, particularly in densely welded sections.

Base-parallel reflections are present in both phases of the andesitic flow and are particularly abundant in the upper phase (e.g., **H-I**, **J-K**, **N-M**, and **H-L**, Figs. 4.16, 4.17). These may be caused by emplacement or welding processes and could be related to bedforms, rheomorphism, or clast geometries and orientations. A particularly strong and continuous reflection is found 50 ns below the interpreted boundary of the two Shevlin Park phases (Fig 4.15, 4.18). Diffraction hyperbolas, mostly in the upper phase, cross this fabric (e.g., surveys **H-I**, **J-K**, Fig 4.16). Radargram **F-P** shows a particularly high density of hyperbolic events. As with the hyperbolic events at the Cascade Pumice Company site, these are interpreted to be formed by diffraction at relatively large clasts within the flow. Migration of this radargram (Fig. 4.20) removes these hyperbolas and clarifies unit boundaries. The signal amplitude decreases with depth within the Shevlin Park flow (excluding the phase boundary reflection) despite there being sufficient energy to produce a relatively strong reflection at the base of the flow. This pattern indicates that the lower phase is more homogeneous than the later phase.

The general lack of reflections produced by the Tumalo Tuff at the Southern Canal

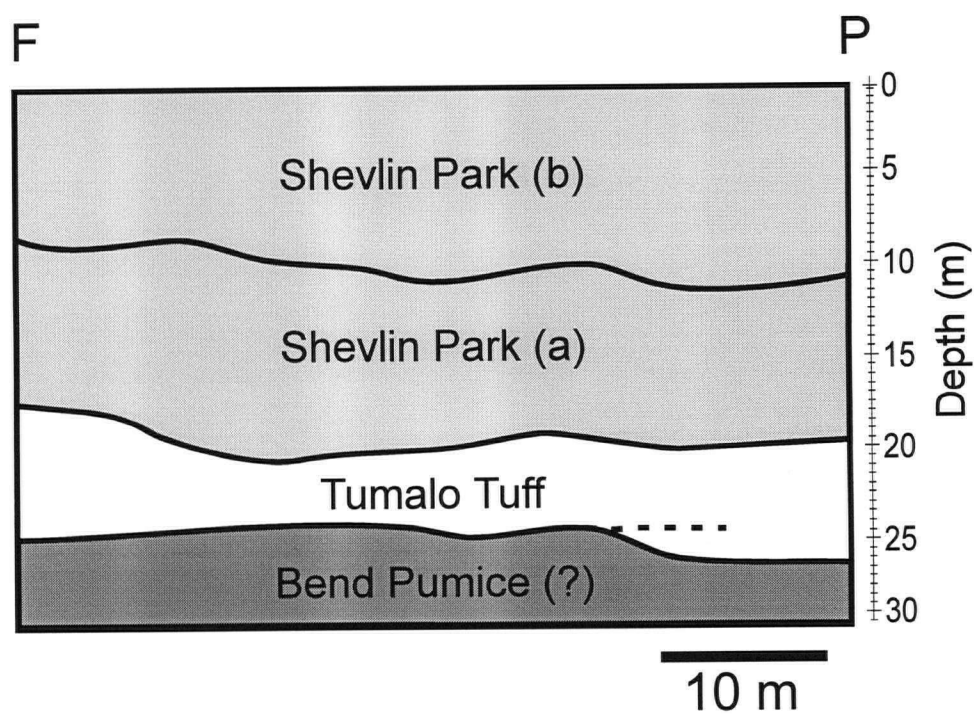
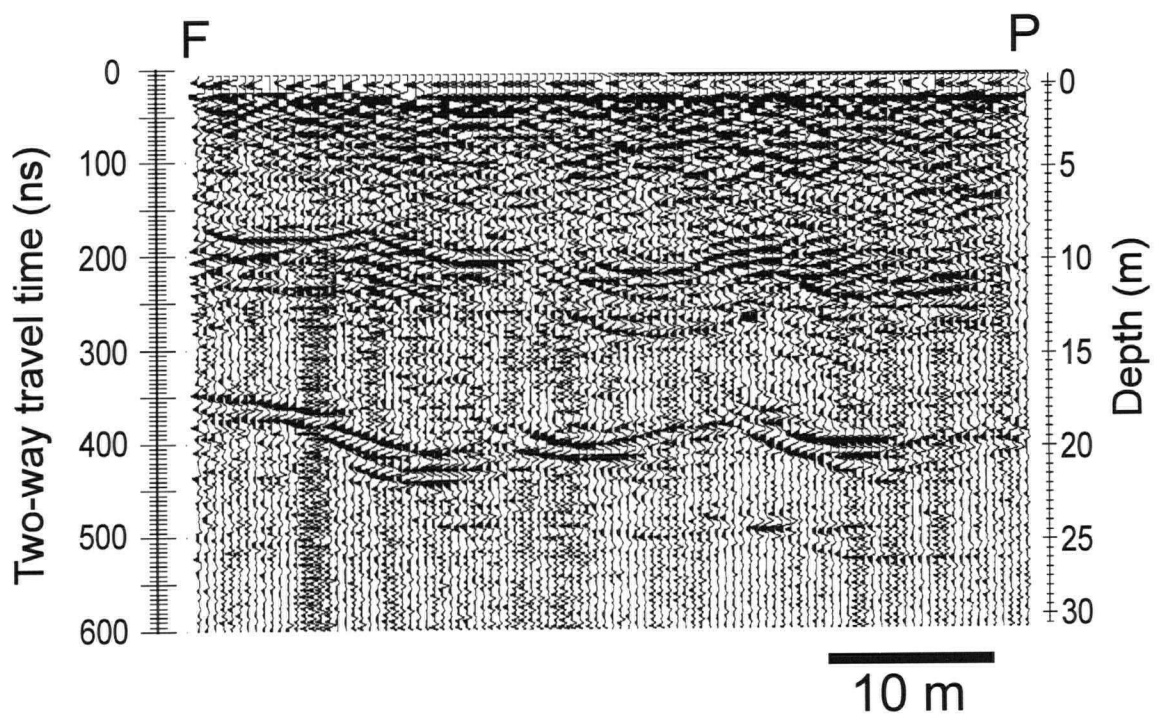


Figure 4.20 a) Radargram of migrated data for survey F-P (100 MHz) using a constant velocity of 0.1 m/ns. b) Interpreted stratigraphy for a).

site is consistent with a massive, homogeneous deposit. All exposures near the surveys show no evidence of welding in the rhyodacite flow. The low amplitude response of the Tumalo Tuff is therefore interpreted to result from a lack of welding (i.e., constant, high porosity) through the entire depth of the deposit. The signal is similar to the lower, unwelded portion of the Tumalo Tuff at the Cascade Pumice pits (Fig 4.3).

4.6 Summary and conclusions

The results of two case studies demonstrate GPR to be capable of mapping unit boundaries, distinguishing between airfall and pyroclastic flow deposits and recognizing welded facies of a pyroclastic flow. At the Cascade Pumice quarry, it was possible to compare geophysical signals to vertical outcrops. I used data from this site to recognize the signals produced by different deposits and facies and understand the origin of these characteristic signals. At the Cascade Pumice pits, the pyroclastic fall deposit is identified by continuous, parallel reflectors created by internal stratification. At both the Cascade Pumice and Southern Canal sites, the unwelded Tumalo Tuff, rhyodacite pyroclastic flow produces an essentially zero amplitude response due to its homogeneous character compared to the scale of the radar wavelength. The welded material at the Cascade Pumice pits produces a much more complex signal with abundant reflections and hyperbolic events. Hyperbolic events are created by the contrast in porosity between relatively large clasts and the welded matrix. In one radargram (Fig. 4.3a) there are dipping reflectors, possibly indicative of flow direction but their origin is not clear.

CMP surveys were used to evaluate velocity variation with depth. A series of CMP

surveys, collected at the Cascade Pumice pits, demonstrate that GPR data can be applied to interpreting and quantifying spatial porosity variations. However, the amount of moisture in the ground has a strong effect on velocity. I advocate the interpretation of these data in terms of relative porosities from which welding patterns can be identified. A combination of velocity profiles and the recognition of characteristic signals for different welding facies, together provide confident geological interpretations of welding patterns.

In addition to the recognition of characteristic signals, criteria used in traditional mapping can also be applied to the identification of deposit types with GPR. For instance, an airfall deposit may be recognized by its high degree of sorting, high porosity, mantling of paleotopography and the reduction of thickness and grain size away from the source.

Theoretically, all of this information can be deduced from GPR surveys. Crude estimates of grain size and degree of sorting information could be gained by running a series of GPR surveys at different frequencies and looking at the density of diffraction hyperbolas as a function of radar wavelength. GPR will never replace traditional mapping but rather it should be used as a supplementary tool providing data where conventional methods are not adequate due to lack of vertical exposure.

Chapter 5

Conclusion

This thesis examines the relationship between porosity and dielectric constant of volcanic rocks through laboratory measurements, and explores the utility of GPR in mapping and characterizing young pyroclastic deposits. In particular, simulations and field studies demonstrate how GPR data can be used to both image, and quantify, porosity variations in pyroclastic deposits. It is evident that GPR is an effective tool for mapping paleotopography, defining major unit boundaries and internal structures, and tracing facies variations (e.g., welding). Furthermore, the nature of unexposed units may be identified based on their geometry and characteristic radar signals. There are numerous applications of GPR in mapping volcanic stratigraphy including the estimation of eruption volumes, airfall isopach maps, correlation of units, and mapping of complicated geometries and facies changes. On a more applied level, GPR also offers an alternative to drilling at potential pumice quarry sites to assess the extent of pumice deposits and the thickness and character of overburden.

My research demonstrates the utility of GPR to basic volcanology; however, there remain a number of areas requiring further research. A model relating porosity to dielectric constant of intermediate-felsic rocks was developed in Chapter 2. The trend formed by these data is remarkably tight and coherent especially considering the samples derive from five deposits and two volcanoes; however, no such relationship was found for basalt samples. Perhaps the higher and more variable concentration of Fe-Ti oxide minerals in basalts causes the data dispersion. The effect of the modes and the geometries of these minerals also needs

to be investigated experimentally. Also, there is a single conspicuous outlier in the intermediate-felsic sample suite (sample MB1) with significantly higher dielectric constant than predicted by the trend formed by other samples in Φ - K' or ρ - K' space. What makes this sample distinct is that it has the lowest porosity of the intermediate-felsic set of rocks and the pore space is dominated by cracks in the glass rather than vesicles. Further work is required to evaluate whether pore geometry and ambient moisture are responsible for the outlier and to determine whether this phenomenon is important at GPR survey frequencies.

An additional factor, not addressed by experiment (Chapter 2), is the effect of partially saturating the pore space with water. Due to the contrasting electrical properties of water compared to air and volcanic rocks at GPR frequencies, this is an important consideration. In fact, water appears to affect GPR velocities at the Cascade Pumice pits near Bend, Oregon, where the water table is more than 150 m below the depths of the surveys (Chapter 4). Therefore, there are few locations where it can be assumed that deposits are absolutely dry and velocity data can be converted to porosity data using the empirical relation developed in Chapter 2. Laboratory studies treating intermediate-felsic volcanic rocks as ternary systems consisting of rock, air and water are a logical extension of the work of Chapter 2. However, even with an understanding of the dielectric properties of variable saturated volcanic rocks, evaluating absolute porosity information of GPR data would still not be a trivial task because water saturation levels must be assumed. For this reason, I advocate interpretations based on relative rather than absolute velocity (porosity) patterns.

An interesting and poorly understood feature of the field GPR data collected is a set of strong, parallel, dipping reflectors observed only in one radargram (line 1). Of particular

interest is the genetic origin of these signals. The structure may indicate primary flow direction and thus GPR would be an important volcanological tool, especially considering the bedform is not readily visible in outcrops. Surveys in other areas would determine whether the dipping reflectors are a common feature in pyroclastic flows. Comparison of survey results in well-exposed areas with flow direction indicators such as imbricated clasts would aid in discerning whether the dipping reflectors are in fact related to flow direction.

References

- Adams, R. J., Perger, W. F., Rose, W. I. and Kostinski, A., 1996. Measurements of the complex dielectric constant of volcanic ash from 4 to 19 GHz. *J. Geophys. Res.*, 1: 8175-8185.
- Bondarenko, A. T., 1971. Influence of high pressure and high temperatures on the dielectric constant of rocks of the Kola Peninsula. *Earth Phys.*, 2: 92-96.
- Brooks, G. R. and Friele, P. A., 1992. Bracketing ages for the formation of the Ring Creek lava flow, Mount Garibaldi volcanic field, southwestern British Columbia. *Can. J. Earth Sci.*, 29: 2425-2428.
- Caldwell, R. R. and Truini, M., 1997. Ground-water and water-chemistry data for the Upper Deschutes Basin, Oregon: U.S. Geological Survey Open-File Report 97-197, 77 pp.
- Campbell, M. J., and Ulrichs, J., 1969. Electrical properties of rocks and their significance for lunar radar observations. *J. Geophys. Res.*, 25: 5867-5881.
- Carey, S. and Sigurdsson, H., 1987. Temporal variations in column height and magma discharge rate during the 79 A.D. eruption of Vesuvius. *Geol. Soc. of Am. Bull.*, 99; 2: 303-314.

- Cas, R.A.F., and Wright, J.V., 1988. *Volcanic Successions: Modern and Ancient*. Chapman & Hall, London: 528pp.
- Chan, C. Y. and Knight, R. J., 1997. The transition zone between effective medium theory and ray theory for the propagation of electromagnetic waves, SEG Annual Meeting Expanded Technical Program Abstracts with Biographies, 67: 422-425.
- Chung, D. H., Westphal, W. B., and Simmons, G., 1970. Dielectric properties of Apollo 11 lunar samples and their comparison with earth materials. *J. Geophys. Res.*, 75: 6524-6531.
- Davis, J. L., and Annan, A. P., 1989. Ground-penetration radar for high-resolution mapping of soil and rock stratigraphy. *Geophys. Prosp.*, 37: 531-551.
- Dix, C.H., 1955. Seismic velocities from surface measurements. *Geophysics* 20: 68-86.
- Dorn, R. I., 1995. Digital processing of back-scatter electron imagery; a microscopic approach to quantifying chemical weathering. *Geol. Soc. of Am. Bull.*, 107; 6: 725-741.
- Drury, M. J., 1978. Frequency spectrum of the electrical properties of seawater-saturated

ocean crust and oceanic island basalts. *Can. J. Earth Sci.*, 15: 1489-1595.

Freunt, A. and Schmincke, H.-U., 1995. Eruption and emplacement of a basaltic welded ignimbrite during caldera formation on Gran Canaria. *Bull. Volc.*, 56: 640-659.

Frisnillo, A. L., Olhoeft, G. R., and Strangway, D. W., 1975. Effects of vertical stress, temperature and density on the dielectric properties of lunar samples 72441,12, 15301,38 and a terrestrial basalt. *Earth Planet. Sci. Lett.*, 24: 345-356.

Gardner J.E., Sigurdsson H., Carey S.N., 1991. Eruption dynamics and magma withdrawal during the Plinian phase of the Bishop Tuff eruption, Long Valley Caldera. *J. Geophys. Res.* 96: 8097-8111.

Gardner J.E., Thomas R.M.E., Jaupart C. and Tait S., 1996. Fragmentation of magma during Plinian volcanic eruptions. *Bull. Volcanol.* 58: 144-162

Gold, T., Bilson, E., and Yerbury, M., 1973. Grain size analysis and high frequency electrical properties of Apollo 15 and 16 samples. *Proc. 4th Lunar Sci. Conf. Geochim. Cosmochim. Acta. Suppl.*, 3: 2149-2154.

Gold, T., O'Leary, B. T., and Campbell, M., 1971. Some physical properties of Apollo 12 lunar samples. *Proc. Second Lunar Sci. Conf. Geochim. Cosmochim. Acta. Suppl.*, 3, 2173-2181.

- Gold, T., Campbell, M. J., and O'Leary, B. T., 1970. Optical and high-frequency electrical properties of the lunar sample. *Science*, 167: 707-709.
- Green, N. L., 1977. Multistage andesite genesis in the Garibaldi Lake area, southwestern British Columbia, Ph.D. Thesis, University of British Columbia, Vancouver, Canada.
- Hansen, W., Sill, W. R., and Ward, S. H., 1973. The dielectric properties of selected basalts. *Geophys.*, 38(1): 135-139.
- Hawton, M., and Borradaile, G., 1989. Dielectric determination of rock fabric anisotropy. *Phys. of the Earth and Planet. Int.*, 56: 371-376.
- Hill, B.E., 1985. Petrology of the Bend Pumice and Tumalo Tuff, a Pleistocene Cascade eruption involving magma mixing. Unpublished M.Sc. Thesis, Oregon State University. Corvallis, OR, United States, pp. 109.
- Hill, B.E., and Taylor, E.M., 1990. Oregon central High Cascade pyroclastic units in the vicinity of Bend, Oregon. *Ore. Geol.*, 52(6): 125-126 and 139-140.
- Higman, S.L., 1990. Chemical discrimination of Cheakamus Valley basalt lava flows, southwestern, British Columbia: statistical constraints. B.Sc. Thesis, University of

British Columbia, Canada.

Houghton B.F. and Wilson C.J.N., 1989. A vesicularity index for pyroclastic deposits. *Bull. Volcanol.*, 51: 451-462

Howell, B.F., and Licastro, P. H., 1961. Dielectric behaviour of rocks and minerals. *Am. Mineral.*, 46: 269-288.

Kanamori, H., Nur, A., Chung, D. H., Wones, D., and Simmons, G., 1970. Elastic wave velocities of lunar samples at high pressures and their geophysical implications. *Science*, 167: 726-728.

Keller, G.V., 1989. Electrical properties. In: R. S. Carmichael (Editor), *Practical Handbook of Physical Properties of Rocks and Minerals*. CRC Press Inc., Boca Raton, Florida, pp. 359-534.

Kennett, B.L.N. and Kerry, N.J., 1979. Seismic waves in a stratified half space. *Geophys. J. Roy. Astr. Soc.*, 57: 557-583.

Klug C and Cashman KV, 1996. Permeability development in vesiculating magmas: implications for fragmentation. *Bull. Volcanol.* 58: 87-100.

Knight, R. and Abad, A., 1995. Rock/water interaction in dielectric properties; experiments

with hydrophobic sandstones. *Geophys.*, 60: 431-436.

Knight, R. J., and Endres, A., 1990. A new concept in modeling the dielectric response of sandstones: Defining a wetted rock and bulk water system. *Geophys.*, 55: 586-594.

Knight, R. J., and Nur, A., 1987. The dielectric constant of sandstones, 60 kHz to 4 MHz. *Geophys.*, 52: 644-654.

Lichtenecker, K., and Rother, K., 1931. Deduction of the logarithmic Mixture law from general principles. *Phys. Zeitsch.*, 32: 255-260.

Lowe, D. J., 1985. Application of impulse radar to continuous profiling of tephra-bearing lake sediments and peats; an initial evaluation. *N. Zeal. J. Geol. Geophys.* 28(4): 667-674.

Manger G.E., 1965. The best value of porosity of lapilli tuff from the Nevada test site. U.S. Geol. Survey Prof. Paper 525-B: 146-150.

Marshall, P., 1935. Acid rocks of Taupo-Rotorua volcanic district. *Roy. Soc. N. Zeal. Trans.*, 64(3): 323-366.

Nelson, S. O., Lindroth, D.P. and Blake, R. L., 1989. Dielectric properties of selected minerals at 1 to 22 GHz. *Geophys.*, 54: 1344-1349.

- Olhoeft, G. R., and Strangway, D. W., 1975. Dielectric properties of the first 100 meters on the moon. *Earth Planet. Sci. Lett.*, 24: 394-404.
- Olhoeft, R. G., Frisnillo, A. L. and Strangway, D. W., 1974. Electrical properties of Lunar Soil Sample 15301,38. *J. Geophys. Res.*, 79: 599-1604.
- Parkhomenko, E. I., 1967. *Electrical Properties of Rocks*. Plenum, New York, 314 pp.
- Press, W. H., Flannery, B. P., Teukolsky, S. A. and Vetterling, W. T., 1986. *Numerical Recipes: The Art of Scientific Computing*. 2nd ed., Cambridge University Press, New York .
- Reynolds, J.M., 1997. *An introduction to applied and environmental geophysics*. John Wiley and Sons, New York, N.Y., pp. 796.
- Roberts, J.J., and Lin, W., 1997. Electrical properties of partially saturated Topopah Spring tuff: water distribution as a function of saturation. *Water Resour. Res.*, 33: 577-587.
- Robertson E.C., and Peck D.L., 1974. Thermal conductivity of vesicular basalt from Hawaii. *J. Geophys. Res.* 79: 4875-4888.
- Ross, C.S. and Smith, R.L., 1961. Ash-flow tuffs: their origin, geologic relations and

identification. U.S. Geol. Surv. Prof. Pap. 366, pp.77.

Russell, J. K., and Stasiuk, M. V., 1997. Characterization of volcanic deposits with ground penetrating radar. *Bull. Volcanol.*, 58: 515-527.

Russell, J.K. and Stasiuk, M.V., 1998. Ground penetrating radar mapping of volcanic deposits and the Late-Bronze-Age paleotopography, Thera, Greece. in, *Volcanoes, Earthquakes and Archaeology* (edited by B. McGuire and D. Griffiths), Spec. Publ. Geol. Soc. Lond. (in press).

Sahagian D.L., Anderson A.T., and Ward B., 1989. Bubble coalescence in basalt flows: comparison of a numerical model with natural examples. *Bull. Volcanol.*, 52: 49-56.

Saint-Amant, M., and Strangway, D. W., 1970. Dielectric properties of dry, geologic materials. *Geophysics*, 35: 624-645.

Sceva, J. E., 1968. Liquid waste disposal in the lava terrane of central Oregon. Report No. FR-4, U. S. Dept. of the Interior, Federal Water Pollution Control Administration, Northwest Region, Pacific Northwest Water Laboratory, Corvallis, Oregon: 66 pp.

Shmulevich, S. A., Troitskiy, V. S., Zelinskaya, M. R., Markov, M. S. and Sukhanov, A. L., 1971. Dielectric properties of rocks at a frequency of 500 MHz. *Earth Phys.*, 12: 68-

76.

Shmulevich, S. A., 1970. Determination of the dielectric characteristics of rocks in the wave length range of 0.8-60 cm. *Earth Phys.*, 19: 100-103.

Singh, J., and Singh, P. K., 1991. Studies of the dielectric constant of Indian rocks and minerals and some other materials. *PAGEOPH*, 135: 601-610.

Sivertz, G. W. G., 1976. *Geology, Petrology, and Petrogenesis of Opal Cone and the Ring Creek lava flow*, B.Sc. Thesis, University of British Columbia, Vancouver, Canada.

Soeder, D. J., Flint L. E., Flint A. L., 1991. Laboratory analysis of porosity and permeability in unsaturated tuffs at Yucca Mountain, Nevada. Geological Society of America, 1991 annual meeting. *Abstracts with Programs - Geological Society of America*. 23; 6, 186 pp.

Stasiuk, M.V., Russell, J.K., and Hickson, C.J., 1996. Distribution, nature, and origins of the 2400 BP eruption products of Mount Meager, British Columbia: linkages between magma chemistry and eruption behaviour. *Geol. Surv. of Can. Bull.*, 486, 27 pp.

Strangway, D. W., Chapman, W. B., Olhoeft, G. R., and Carnes, J., 1972. Electrical properties of lunar soil dependence on frequency, temperature and moisture. *Earth*

Planet. Sci. Lett., 16: 275-281.

Swanson, D. A., 1973. Pahoehoe Flows from the 1969-1971 Mauna Ulu Eruption, Kilauea Volcano, Hawaii. Geol. Soc. Am. Bull., 84: 615-626.

Troitsky, V. S., and Shmulevich, S. A., 1973. Dependence of dielectric properties of rocks on their volume weight. J. Geophys. Res., 79: 6933-6935.

Tuck, G. J., and Stacey, F. D., 1978. Dielectric anisotropy as a petrofabric indicator. Tectonophys., 50: 1-11.

Ulaby, F. T., Bengal, T. H., Dobson, M. C., East, J. R., Garvin, J. B., and Evans, D. L., 1990. Microwave dielectric properties of dry rocks. IEEE Trans. GeoSc. Remote Sensing, 28(3): 325-336.

Ursin, B., 1983. Review of elastic and electromagnetic wave propagation in horizontally layered media. Geophys., 48: 1063-1081.

Walker G.P.L., 1989. Spongy pahoehoe in Hawaii: a study of vesicle-distribution patterns in basalt and their significance. Bull. Volcanol., 51: 199-209.

Wharton, R. P., Hazen, G. A., Rau, R. N., and Best, D. L., 1980. Electromagnetic propagation logging: advances in electromagnetic propagation logging, Soc.Petr.Eng.,

AIME, Paper 9267

Whitham A.G., and Sparks R.S.J., 1986. Pumice. *Bull. Volcanol.*, 48: 29-223.

Yilmaz, O., 1987. Seismic data processing. *Investigations in geophysics Volume 2*. Soc. Explor. Geophys., Tulsa, OK, United States.

Appendix I

Measurement of density and porosity in volcanic rocks

Several properties unique to volcanic rocks obviate the standard procedures for measuring density and porosity; volcanic rocks tend to have lower permeabilities than sedimentary rocks of the same porosity (Klug and Cashman, 1996), can be less dense than water, can contain anomalously large pores, and can have porosities as high as 98% (Robertson and Peck, 1974). The purpose of this appendix is to describe the problems associated with established techniques and give a rationale for the methods used in the present project. Note that although not repeatedly stated, all papers referenced in this appendix deal with volcanic rocks.

Density

Density is mass per unit volume and an obvious approach to determining bulk density (ρ_T), defined as the density of the whole rock including pores, is to measure mass (actually weight) and volume directly:

$$\rho_T = \frac{wt_{rock}}{V_T} \quad (A1.1)$$

Determination of sample weight (wt_{rock}) is straightforward and uses dry samples. There are three techniques commonly employed to determine bulk volume (V_T):

- i) measure volume of liquid displaced by the sample (Carey and Sigurdsson, 1987; Gardner et al., 1991),
- ii) calculate sample volume from the weight of liquid displaced by the sample (e.g., water or mercury pycnometer) (Manger, 1965; Gardner et al., 1996), and
- iii) calculate volume from dimensions of carefully machined samples (Robertson and Peck, 1974; Witham and Sparks, 1986; Walker, 1989; Gardner et al., 1996).

The first two methods require modification for porous rocks because fluids can enter pores thereby causing low estimates of sample volume. In the past, this problem has been addressed by blocking pores with a thin film of silicon-based aerosol spray (Houghton and Wilson, 1989) or with wax (Carey and Sigurdsson, 1987) or wrapping the sample with a sheet of wax, plastic or latex (Gardner et al., 1991; Sahagian et al., 1989; Houghton and Wilson, 1989). No such modifications are required for the technique of machining samples into regular geometries. Furthermore, samples are not contaminated (e.g., by sealants) and, thus the sample can be used subsequently for other measurements (e.g., porosity and dielectric constant). The apparatus for direct measurement of mass and volume are simple and such techniques are commonly used in studies where the porosity of samples need not be measured directly and highly accurate estimates of density are not required. An example is the calculation of pumice or lithic clast densities for Plinian column height determination (e.g., Carey and Sigurdsson, 1987).

Densities are commonly determined using hydrostatic methods. Samples are dried and weighed in air ($w_{t_{rock\ in\ air}}$) then weighed suspended in water ($w_{t_{rock\ in\ water}}$). Density (ρ) is calculated from:

$$\rho = \frac{\rho_{water} \times w_{t_{rock\ in\ air}}}{w_{t_{rock\ in\ air}} - w_{t_{rock\ in\ water}}} \quad (A1.2)$$

Depending on the porosity and permeability of the sample, equation (A2) will give bulk density (ρ_T), solid density (ρ_S , the density of the solid, void-free portion) or an apparent density in between these two end-values. The standard method to determine the bulk density of porous samples is to saturate the sample with water and quickly weigh it in air after wiping

off excess water from the surface (Robertson and Peck, 1974; Cas and Wright, 1988). In this way, the weight of the water in the pores can be determined and bulk density (ρ_T) calculated using the following formula:

$$\rho_T = \frac{\rho_{\text{water}} \times w_{\text{dry rock in air}}}{w_{\text{dry rock in air}} - w_{\text{saturated rock in water}} + w_{\text{saturated rock in air}}} \quad (\text{A1.3})$$

Volcanic rocks, however commonly have vesicles which are too large for water to be retained when the saturated sample is removed from water (Robertson and Peck, 1974; Witham and Sparks, 1986). In order to measure the bulk density of such rocks by hydrostatic methods, the samples must be rendered impermeable to water. This can be done using some of the techniques listed above in the discussion of direct volume measurements. In the case of wrapping the sample with a sheet of wax, the formula for bulk density is (after Houghton and Wilson, 1989):

$$\rho_T = \frac{\rho_{\text{water}} \times w_{\text{dry rock in air}}}{w_{\text{dry rock in air}} + w_{\text{wax sheet in water}} - w_{\text{wax-coated rock in water}}} \quad (\text{A1.4})$$

An additional problem, unique to volcanic rocks, is that samples which are less dense than water will float giving the false result that the samples have the same bulk density as water. A less dense fluid could be used, but the simplest solution is to ballast the sample with a metal weight and the negative effective weight of the sample in water calculated by subtracting the ballast weight (Houghton and Wilson, 1989).

Porosity

Porosity (Φ) can also be determined by hydrostatic methods. The relevant formula

(after Cas and Wright, 1988) is:

$$\Phi = \frac{W_{\text{saturated rock in air}}^t - W_{\text{dry rock in air}}^t}{W_{\text{saturated rock in air}}^t - W_{\text{saturated rock in water}}^t} \quad (\text{A1.5})$$

However, the porosity given by equation (A1.5) can only be considered a minimum porosity as it does not include unconnected pores. Although the amount of water absorbed by a sample can be maximized by placing the sample in a container, from which air is evacuated and then flooded with de-aerated water which is left under pressure for days (Cas and Wright, 1988; Robertson and Peck, 1974), one cannot be sure that all pores are filled.

Hydrostatic or other methods which involve contact with water may not be feasible for rocks which contain zeolites. Soeder et al. (1991) found that porosity measurements of zeolitic tuffs from Yucca Mountain were as much as 8% higher when water was used rather than other liquids or gas. This is not an insurmountable problem for hydrostatic bulk density measurements where the sample can be coated with wax or some other material which is impermeable to water. However, such coating techniques are not feasible for hydrostatic porosity measurements because the weight of the water in the pores is required to calculate porosity.

Porosity can also be expressed as a function of bulk and solid (void-free) densities (ρ_T and ρ_S respectively):

$$\Phi = \frac{\rho_S - \rho_T}{\rho_S} \quad (\text{A1.6})$$

Techniques to measure ρ_T have already been discussed and the only additional information required is ρ_S . Porosity is sometimes calculated from the relation in equation (A1.6) using chemistry and proportions of glass and minerals to estimate solid density (Sahagian et al.,

1989; Gardner et al., 1991; 1996). Determining the solid density of a porous rock by hydrostatic methods requires completely filling all pores with liquid. Even where possible to do so, it is difficult to ensure complete filling of all pores. In some experiments involving crushed rock it is assumed that the rock from which the powder was made was not porous and the porosity of the crushed rock and air mixture is determined by substituting solid density (in equation A6) with the bulk density of the original rock (eg., Campbell and Ulrichs, 1969).

Klug and Cashman (1996) and Russell and Stasiuk (1997) calculated the solid volume of vesicular samples with a helium pycnometer (or helium porosimeter), a technique based on the ideal gas law. Although rocks should be at least as permeable to helium gas as to water, the question as to whether or not there are unconnected pores which are not filled with gas remains. The apparatus has been extensively used on sedimentary material but sedimentary rocks generally have higher and more regular permeabilities than lavas of the same porosity (Klug and Cashman, 1996).

Another approach to determining solid density (which in turn is used to calculate porosity) is to measure the density of a representative powdered sample. The assumption is that if the sample is crushed fine enough, all pores will be accessible to fluid. A helium pycnometer is an ideal apparatus to measure the volume of the powdered material (K. Cashman, personal communication). In determining the porosity of welded lapilli tuff, Manger (1965) used a water pycnometer and de-aerated the crushed rock by boiling the water-powder mixture in the pycnometer flask for ten minutes. Note that the term pycnometer is used in this appendix both for the helium pycnometer and water pycnometer,

the apparatus and theory behind these two techniques are different. The water (or other liquid) pycnometer is a specially designed flask used to measure the weight of fluid displaced by the sample. The helium (or other gas) pycnometer is based on the ideal gas law $PV=nRT$; n (number of moles of gas), R (gas constant) and T (temperature) are kept constant while the volume of the chamber which contains the sample and helium is changed. Using the difference in pressure for the different chamber volumes, the volume of the sample is calculated.

Direct measurements of porosity are sometimes done visually or by digitally processing images of thin sections (e.g., Dorn, 1995) or hand sample surfaces (Kanamori et al., 1970), assuming that the porosity in three dimensions is the same as in two dimensions. Walker (1989) took this approach one step further and measured porosity in one dimension: he drew lines across sawn surfaces and found the porosity by dividing the length of line crossing vesicles over the total length of the line. No comparison between the results of these quick methods and more sophisticated ones was located for volcanic rocks.

Selection of procedures for present study

The laboratory study (Chapter 2) includes the measurements of bulk density and porosity for cylindrical disks of volcanic rocks. Porosity and density measurement methods were chosen such that: 1) they were applicable to sample set with large range in porosity; 2) they were applicable to samples with individual pores as large as 5 mm in diameter; and 3) they did not contaminate samples thus affecting subsequent capacitance measurements. Due to the high porosity of many samples, determining bulk volumes by fluid displacement is not

feasible because fluids can enter pores thereby causing low estimates of sample volume. Materials such as silicon spray and wax cannot be used to plug pores due to sample contamination. Hydrostatic methods to determine porosity or bulk density are not practical because many samples have vesicles which are too large for the pores to remain saturated when the sample is removed from water.

The methods implemented in this study (Chapter 2) fit the three requirements listed above and do not involve water or sealing vesicles. The procedures entail: 1) weighing samples, 2) measuring disk diameters and heights to calculate bulk volume, and 3) using a He-pycnometer to determine solid volumes of disks and powders from the same hand-samples. Further details on the methodologies are listed in Chapter 2 (pages 15-16).

Appendix II

Scale of heterogeneity of pyroclastic deposits and applicability of gradational porosity profile models

Chapter 3 simulates the interactions between a radar wave and subsurface models of K' , that contain gradations in porosity. A logical question is whether the actual scale of heterogeneity of pyroclastic deposits can be adequately modeled by a gradational subsurface model. Profiles such as those used in this study may be practical for fine-grained, lithic-poor deposits, but in many cases deposits contain variations in physical properties that cannot realistically be modeled as gradational. For example, a deposit may show an overall gradational porosity profile at one scale (e.g., Fig. 3.2a), yet, on a finer scale (e.g., decimeters) the presence of large pumice blocks or lithic clasts could impart sharp (non-gradational) deviations from the background Φ and K' profiles. Such clasts could generate reflections of strong amplitude or act as point diffractors and obscure the general patterns seen in the simulations (e.g., Fig. 3.5).

We illustrate the problem presented by sharp, small-scale discontinuities and a method to overcome it with the GPR survey of a welded pyroclastic flow (Fig. 3.8). As discussed in the main text, the middle and upper portions of the deposit generate abundant reflections and numerous hyperbolic events (concave down). The diffraction hyperbolas are interpreted to originate from relatively large lithic or pumice clasts. In order to apply the results of our model simulations, we must remove the "noise" from erratic clasts to uncover the baseline response caused solely by changes in welding. Diffraction hyperbolas can be collapsed into their point sources by migration (Fig. A2.1a). Migration removes the tails of diffraction hyperbolas but there remain diffraction sources as well as westward dipping reflections of unknown origin (Fig. A2.1a). To eliminate the entire effect of erratic clasts and steeply dipping reflectors, we have averaged groups of 10 adjacent traces of the Figure 8

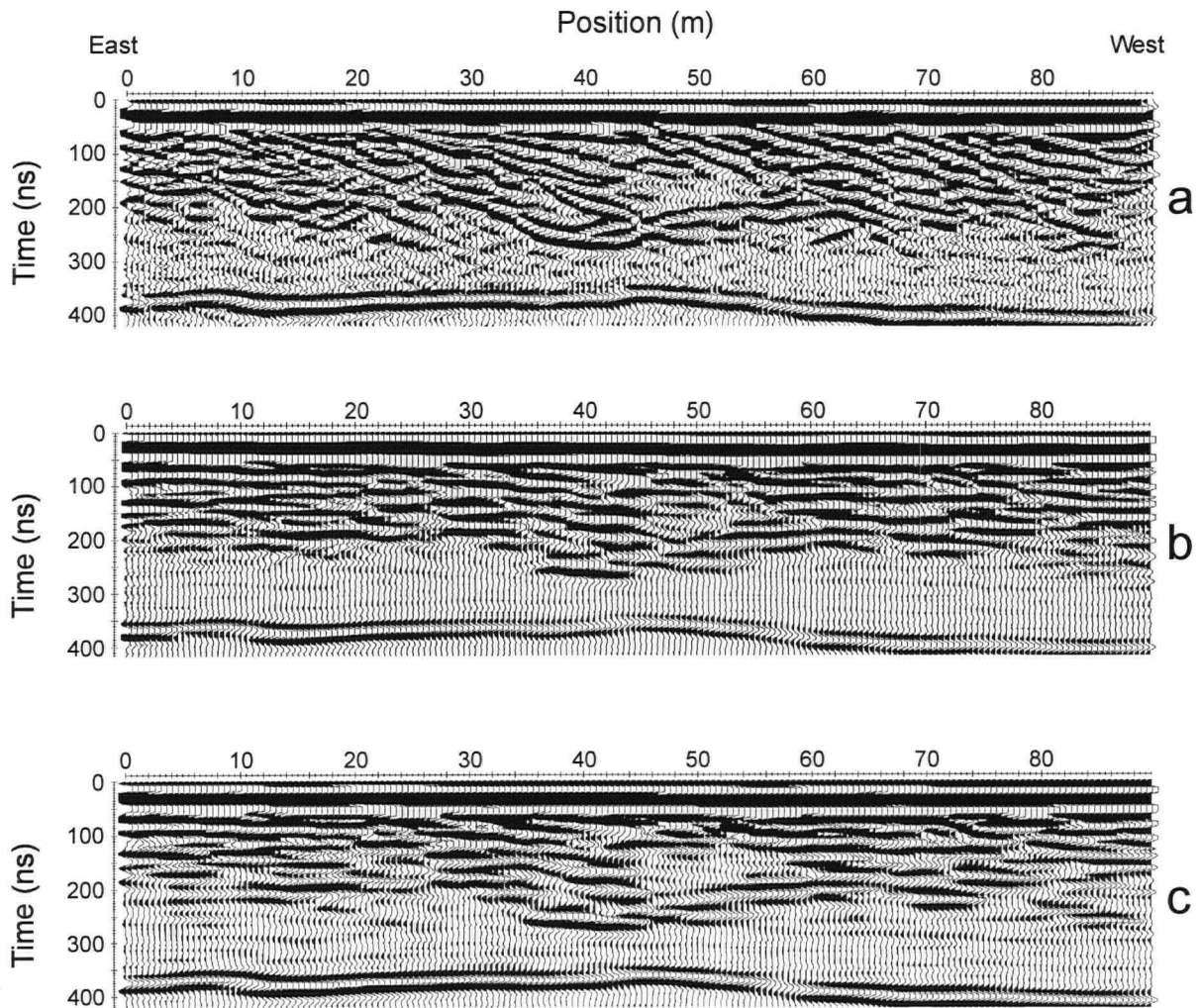


Figure A2.1 Three processed versions of the radargram of Fig. 3.8. All radargrams are gained with an SEC gain with start value of 10, gain max of 120 and attenuation of 3 dB/m. A gain factor of 0.25 was applied to migrated data to compensate for higher amplitudes produced by the migration process. a) Migrated data assuming constant velocity of 0.09 m/ns. Note the removal of hyperbolic events seen in Fig. 3.8. b) Each trace is the mean of 10 adjacent traces in Fig.3.8. c) Each trace is the average of 10 adjacent traces of the migrated radargram (a).

radargram (Fig. A2.1b). Each trace shown in Figure A2.1b is, therefore, the spatial average of traces over a lateral distance of five meters. As long as the clasts are distributed randomly and not concentrated in thin horizons, this process removes the "noise" imparted by clasts as well as steeply dipping reflectors. The resulting radargram (Fig. A2.1b) shows sub-horizontal reflections in the middle and upper portions of the pyroclastic flow with very little response below this until the base of the flow. Migration followed by averaging of groups of 10 adjacent traces (Fig. A2.1c) gives a similar result to simple averaging (A2.1b). Short reflections in Figure A1a such as the six meter-long reflection centered at (40 m, 260 ns) could have formed by smearing of a clast response and, therefore, may not actually represent the desired baseline pattern. However, many of the upper zone reflections are continuous over a distance of more than 10 m and are too long to be the result of smearing individual clast reflections by 5m spatial averaging. Note that this averaging technique will not uncover a baseline pattern as desired in the presence of sub-horizontal bedforms.

Appendix III

Effect of water on radar velocities

The velocity data of Chapter 4 derive from CMP surveys collected in the Bend-Tumalo area, Central Oregon. This region is dry and the water table is about 185 m below surface (Sceva, 1968; Caldwell and Truini, 1997) which is many times the depths imaged by the GPR surveys. Most precipitation occurs in the winter and these surveys were conducted in July and August during the hot, dry, summer season. However, even in August there remains residual moisture in the ground. While the pit walls are dry, material dug out less than a meter into the wall is darker-coloured indicating the presence moisture. There are no visible drops or pockets of water filling spaces suggesting there are thin films of water adsorbed on the surfaces. Because the deposits are highly porous, there is a relatively large surface area to bulk volume ratio and a significant amount of water could be retained by the rocks.

A comparison of calculated interval velocities (Chapter 4) with laboratory measurements on dry volcanic rocks (Chapter 2) indicates that the velocities observed at the Cascade Pumice site are too slow to correspond to completely dry deposits. For a low-loss medium, velocity (V) is related to dielectric constant by:

$$V = \frac{c}{\sqrt{K'}}, \quad c = 3 \times 10^8 \text{ m/s} \quad (\text{A3.1})$$

(e.g., Davis and Annan, 1989). Using Eq. (A3.1), the velocity profiles from surveys CMP1 and CMP3B (Fig.4.8) are converted to a K' profile (Fig. A3.1). From experiments on rocks which were dry except for air-derived moisture (Chapter 2), the K' of intermediate to felsic volcanic rocks is related to porosity by:

$$(K')^{0.96} = \Phi + 6.51(1 - \Phi) \quad (\text{A3.2})$$

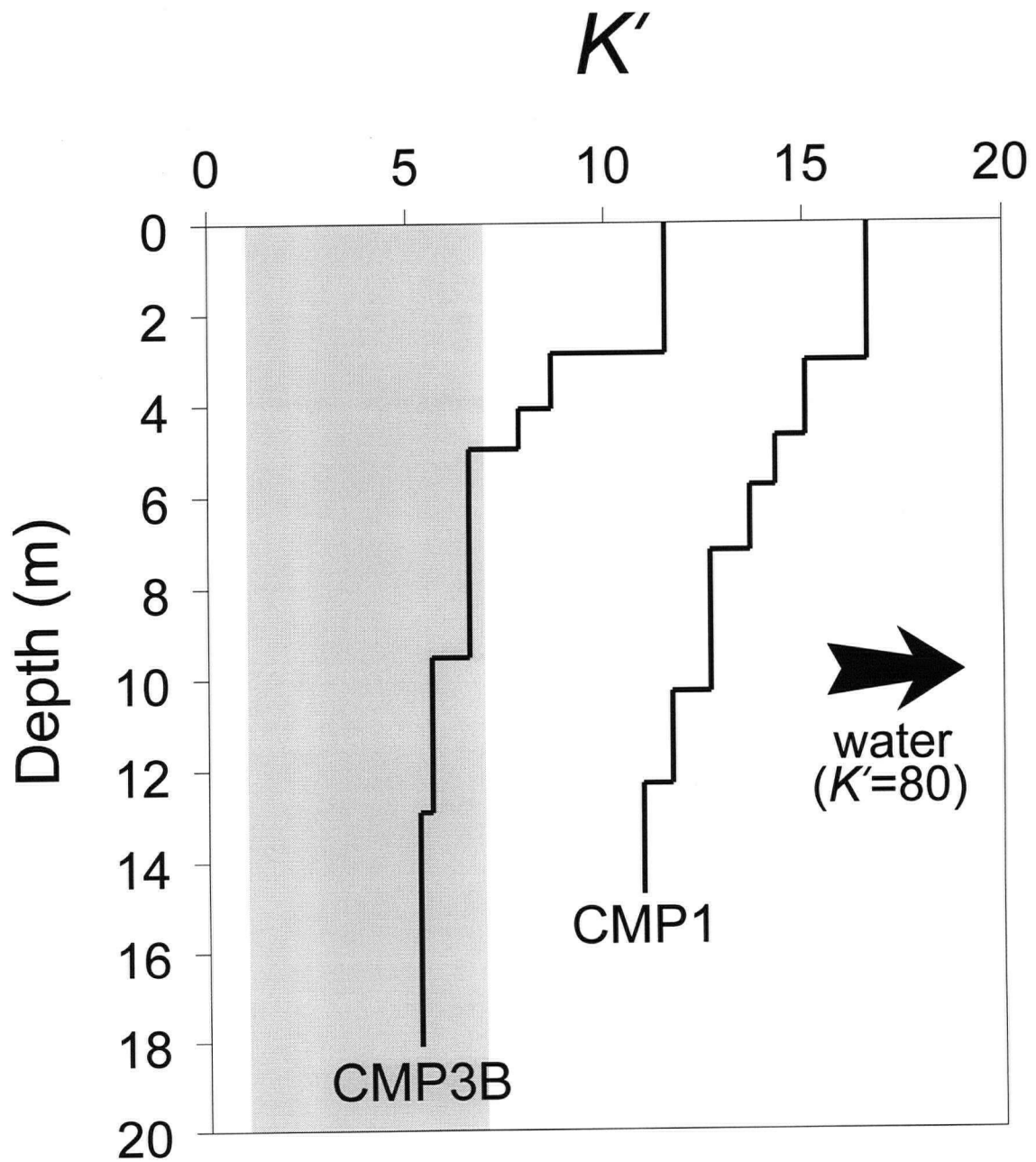


Figure A3.1 Dielectric constant vs. depth data for two CMP surveys at Cascade Pumice Company pits (Chapter 4). The shaded region indicates the range of values predicted for dry, intermediate to felsic volcanic rocks according to laboratory experiments (Eq. 2.13, Chapter 2).

where Φ is the fractional porosity of the rock ($0 \leq \Phi \leq 1$). The maximum dielectric constant possible according to Eq. (A3.2) is 6.97 which corresponds to no pore space ($\Phi=0$). Figure A3.1 shows dielectric constant values substantially exceeding this maximum. This discrepancy is attributed to the presence of water ($K'_{water} = 80$) which has a much higher dielectric constant than air (1) or intermediate volcanic rocks (~ 6.5).

Volcanic deposits are found in all climates from wet tropics, dry deserts to permafrost regions. In interpreting velocity analysis results one must be aware of the potential effect of water on velocity patterns. For example, in Chapter 4, I attributed increases in velocity with depth to increasing porosity (decreasing degree of welding) towards the base of the Tumalo Tuff, a nearly dry, welded pyroclastic flow. This interpreted relative porosity profile is in agreement with outcrop-scale observations. However, if water saturations are very high, then a decrease in degree of welding with depth would be expected to cause a decrease in velocity rather than increase as observed in these data. This is because air in the pores is replaced by water and $V_{water} \ll V_{rock} < V_{air}$ (e.g., $K'_{water} \gg K'_{rock} > K'_{air}$).

Because moisture content tends to increase with depth in the vadose zone, radar CMP results typically show a decrease in velocity with depth (Reynolds, 1997). The fact that I see an increase in velocity within the Tumalo Tuff (Chapter 4) despite the presence of moisture substantiates the notion that porosity increases with depth and that water saturations are not very high at this site. I advocate the use of relative velocity (porosity) rather than absolute velocities in the interpretation of volcanic sections and the identification of deposit type or facies within a deposit. Extra caution is required when interpreting profiles where velocity decreases with depth, as this could simply be a moisture content effect. Even basic

knowledge such as precipitation patterns and approximate water table depths in the area may be sufficient to discriminate between hydrological and volcanological origins of relative velocity profiles.